Pia Hofmann, BSc

Nanostructured Copper-Zinc Alloys as Alternative Anode Materials for Lithium-Ion Batteries

Master Thesis

to achieve the university degree of
Diplom-Ingenieurin
Master programme: Technical Chemistry

submitted to
Graz University of Technology

Supervisors
Univ.-Prof. Dr.rer.nat Martin Wilkening
Dr. Ilie Hanzu
Institute for Chemistry and Technology of Materials

Graz, December 2018

Eidesstattliche Erklärung

Hiermit erkläre ich an Eides statt, dass ich die vorliegende Arbeit selbstständig verfasst, andere als die angegebenen Quellen/Hilfsmittel nicht benutzt und die den benutzten Quellen wörtlich und inhaltlich entnommenen Stellen als solche kenntlich gemacht habe. Das in TUGRAZonline hochgeladene Textdokument ist mit der vorliegenden Diplomarbeit identisch.

Affidavit

I declare that I have authored this thesis independently, that I have not used other than the declared sources/ resources, and that I have explicitly indicated all material which has been quoted either literally or by content from the sources used. The text document uploaded to TUGRAZonline is identical to the present master thesis.

Datum / Date	Unterschrift / Signature

Acknowledgment

First, I would like to thank Univ.-Prof. Dr. rer. nat. habil. Martin Wilkening for giving me the opportunity to do my master thesis at the Institute for Chemistry and Technology of Materials and my supervisor Dr. Ilie Hanzu for his support during the practical work as well as during the writing of the master thesis.

In addition, I want to thank Dipl.-Ing. Sarah Lunghammer who always helped me during the NMR measurements with her experience, advice and assistance. Furthermore, I would like to thank Dr. Denise Prutsch for preparing everything for my start and the passing on of her know-how, which made my entry into the world of lithium ion batteries much easier.

I also want to thank Dr. Brigitte Bitschnau and Univ.-Prof. Dr. techn. Franz-Andreas Mautner for doing the XRD measurements, Ao.Univ.-Prof. Dr.techn. Robert Saf and Dr. Ilie Hanzu for doing the SEM measurements and Dr. Raffaele Ricco for the BET-measurement. Furthermore, I would like to acknowledge the Christian-Doppler Laboratory for Lithium-Ion Batteries for the financial support.

Of course, I would also like to thank the whole working group of Prof. Wilkening for the support from all sides at any time when help was needed, which cannot be taken for granted.

My family also deserves a big thank you for having made it possible for me to study at Graz University of Technology and for supporting me financially and emotionally in both good times and bad.

A big thank you must also go to Jasmin Handl, the best fellow student, roommate and friend, as well as to Sarah Schneider and Nadja Grißmann, who offered me asylum during the last months and of course to all my friends for providing unforgettable moments in Graz.

THANK YOU

Abstract

Rechargeable lithium ion batteries are an important energy storage technology with a wide variety of applications. Graphite is probably the most frequently used anode material. Unfortunately, the practical specific capacity of the graphite-based battery electrodes has already reached its theoretical limit of 372 mAh g^{-1}. With no further room for improvement, research tends towards the investigation of alternative anode materials.

Porous, nanostructured Cu-Zn alloys used as alternative anode material have shown excellent low temperature behaviour as well as high rate capability when tested in lithium half-cells. Varzi et al. [1] have already done some research on the electrochemical properties of the lithium alloy electrode at variable temperatures, but to our knowledge no investigations on the lithium ion dynamics is reported up to now.

This master thesis is intended to provide an easier access to this topic and attempts to clarify questions like: "Where does the superior low temperature behaviour of the Cu-Zn alloy come from?" or "How can further capacity improvement be achieved?"

Solid-State NMR spin-lattice relaxation (SLR) measurements are a useful tool for the investigation on lithium hopping processes including jump rates and activation energies. With the $T_{1\rho}$ experiment, a method sensitive to longer range ion transport, jump rate maxima in the order of 10^5 Hz were obtained at a temperature of 70 °C for an electrode lithiated to an extent of 66% (of the total Li storage capacity) and at 90 °C for a fully lithiated sample. The recorded jump rates are in the order of the well-studied material $Li_4Ti_5O_{12}$ (LTO). Based on the shape of the $T_{1\rho}$ Arrhenius plot, diffusion is tentatively expected to proceed in confined dimensions rather than three-dimensional. In addition, low activation energies were obtained at the low temperature flank of the T_1 Arrhenius plot which might be the reason for the excellent performances at low temperature although the mobility of the ion is limited by the thermal energy.

Trying to improve the capacity of the electrode by the combination with amorphous as well as crystalline titania nanotubes has shown that slight improvement could be reached regarding the use of crystalline titania nanotubes. It was also shown that a certain roughness of the substrate is necessary to prevent the Cu-Zn alloy from crumbling off the current collector which leads to capacity fading.

As a second part, the influence of the annealing step on the titania nanotubes was investigated and current-voltage(IV)-curves were recorded for a crystalline nanotube sample within a potential range of -4 V to +4 V. Non-linear IV-characteristics as expected for semiconductors are visible and lead to resistivities ranging between 10^3 to 10^4 Ω cm.

Kurzfassung

Wiederaufladbare Lithium-Ionen-Batterien sind ein wichtiges Energiespeichermedium und finden Anwendung in vielen Bereichen. Graphit ist dabei das wohl am häufigsten verwendete Anodenmaterial, aber die praktische, spezifische Kapazität des Elektrodenmaterials stößt bereits and die theoretische Grenze von 372 mAh g^{-1}. Daher tendiert die Forschung zur Untersuchung alternativer Anodenmaterialien.

Eine Alternative zu Graphit sind poröse, nanostrukturierte Cu-Zn-Legierungen, welche sich durch ihr ausgezeichnetes Verhalten bei tiefen Temperaturen sowie durch eine hohe „rate capability“ auszeichnen. Varzi et al.[1] haben bereits Untersuchungen zu den elektrochemischen Eigenschaften der Li-Legierungselektrode bei unterschiedlichen Temperaturen durchgeführt. Eine Untersuchung der Lithiummobilität wurde aber laut unserer Kenntnis noch nicht publiziert.

Diese Masterarbeit soll einen Zugang zu diesem Thema schaffen und Fragen klären wie: ”Woher kommt das herausragende Tieftemperaturverhalten der Cu-Zn Legierung?” oder ”Wie kann eine weitere Verbesserung der Kapazität erreicht werden?”

Festkörper-NMR Spin-Gitter-Relaxationsmessungen (SLR) sind dabei ein nützliches Werkzeug zur Untersuchung von Lithium-Sprungprozessen einschließlich Sprungraten und Aktivierungsenergien. Mit einem $T_{1\rho}$ Experiment, einem Verfahren, das empfindlich auf Sprungfrequenzen im kHz-Bereich reagiert, wurden maximale Sprungfrequenzen in der Höhe von 10^5 Hz für Temperaturen zwischen 70 und 90 °C erhalten, was ungefähr der Sprungrate von $Li_4Ti_5O_{12}$ (LTO) entspricht. Basierend auf der Form des $T_{1\rho}$ Arrhenius-Plots wird erwartet, dass die Lithium Ionen nicht in drei Dimensionen diffundieren, sondern die Diffusion auf eine oder zwei Dimensionen begrenzt ist. Darüber hinaus wurden niedrige Aktivierungsenergien aus der Niedertemperaturflanke des T_1-Arrhenius-Diagramms erhalten, was der Grund für die hervorragenden Leistungen bei niedrigen Temperaturen sein könnte, obwohl die Mobilität des Ions durch die geringe thermische Energie limitiert ist.

Der Versuch, die Kapazität der Cu-Zn Elektrode durch die Kombination mit amorphen oder kristallinen Titandioxid-Nanoröhrchen zu verbessern, hat gezeigt, dass hinsichtlich der Verwendung von kristallinen Titandioxid-Nanoröhrchen geringe Verbesserungen erzielt werden können. Des Weiteren war sichtbar, dass eine gewisse Rauheit des Substrats notwendig ist, um ein Abbröckeln der Legierung zu verhindern, was zu einem kontinuierlichen Kapazitätsverlust führen würde.

Im zweiten Teil wurde der Einfluss des Temperns auf die amorphen Titandioxid-Nanoröhrchen untersucht und Strom-Spannungs-Kurven der kristallinen Nanoröhrchen wurden im Bereich von -4 V bis +4 V aufgezeichnet. Alle IV-Kennlinien zeigen ein nicht-lineares Verhalten, typisch für Halbleiter, woraus sich Widerstände im Bereich von 10^3 bis 10^4 Ω cm ergeben.

Table of Content

List of Abbreviations

SLR	spin-lattice relaxation
SSR	spin-spin relaxation
LTO	$Li_4Ti_5O_{12}$
LIB	lithium ion batteries
PC	propylene carbonate
EC	ethylene carbonate
DEC	diethyl carbonate
DMC	dimethyl carbonate
LCO	$LiCoO_2$
LMO	$LiMn_2O_4$
NMO	$LiNi_{0.5}Mn_{0.5}O_2$
NMC	$LiNi_xMn_yCo_zO_2$
LFP	$LiFePO_4$
D_{Li+}	lithium ion diffusion coefficient
NMR	nuclear magnetic resonance
SEI	solid electrolyte interface
SEM	scanning electron microscopy
SE	secondary electrons
BSE	back scattered electrons
EDX	energy dispersive x-ray analysis
CV	cyclic voltammetry
GCPL	galvanostatic cycling with potential limitation
PEIS	potentio electrochemical impedance spectroscopy
DSC	differential scanning calorimetry
rf-pulse	radio frequency pulse
FID	free induction decay
MAS	magic angle spinning
XRD	X-ray diffraction
BET	Brunauer Emmett Teller
PP	polypropylene
TNT	titania nanotube(s)
ICSD	Inorganic Crystal Structure Database
LT	low temperature
HT	high temperature
RT	room temperature
IV	current-voltage
1,2,3D	one-, two- or three-dimensional

1. Introduction

1.1. Lithium Ion Batteries – General Aspects

In times of increasing costs of raw materials and people becoming more and more conscious of important environmental issues, the usage of alternative energy sources is gaining significantly in relevance. Since natural energy sources like wind, water, sun or geothermal heat do not deliver constant amounts of energy, the fluctuations must always be compensated in order to stabilize the electric power grid – storing energy is highly important. Lithium ion batteries can be a possible solution to store energy at peak periods over a short (seconds to minutes) or a long time and deliver it to the grid when needed. However, so far, costs of such LIB based storage systems are quite high [2] and capacities too low [3] leading to a yet insufficient performance/price ratio. Additional concerns are raised by the possible future scarcity of lithium and some transition metals like cobalt as well as the political situation and the working conditions in the mining areas [4]. Nevertheless, the number of publications on this topic increases and an annual cost decline of 30% on the cell level is noticeable [3].

Nevertheless, the long-term energy storage capability, rechargeability paired with the combination of sufficiently high power and the highest energy density, are the reason why lithium ion batteries are chosen as energy source for portable electronic devices [5]. From mobile phones and notebooks up to electric toothbrushes or remote-controlled cars, batteries are indispensable in today's society. It is also worth mentioning the automotive industry sector, where we see an increased interest and continuous development of electric cars, year after year.

In Li-ion batteries lithium ions are the mobile ionic species. Lithium possesses one of the smallest ionic radii of any single charged ion and is the third lightest element in the periodic table. Due to these facts the lithium ion can diffuse fast through the liquid and the solid state enabling high power densities and high specific and volumetric capacities [4] of Li-ion batteries.

1.1.1. Fundamentals

Broadly speaking, a LIB consists out of a positive electrode, a negative electrode, the electrolyte and a separator. The working principle is the reversible intercalation of lithium which is presented in Figure 1. During battery charging, the lithium ion moves from the positive to the negative electrode; this motion is driven by the current applied. The discharging is the opposite process, it occurs spontaneously and leads to

the movement of electrons from anode to cathode through the external circuit (the load). Please note that the electrons are transported through the outer circuit from the positive to the negative electrode (in charge) or vice versa (in discharge). Concomitantly, the ions are forced to use the inner ionic pathway through the electrolyte and the separator, moving from one electrode to the other.

The lithium ion intercalation/ insertion process includes the following processes:

- Migration or diffusion of the solvated lithium ion through the electrolyte to the electrode surface
- Desolvation and subsequent transfer of the ions to free lattice sites near the surface region of the host
- Solid-state diffusion inside the host material.

The separator usually is a microporous membrane which enables lithium ions to pass through when being soaked with a liquid electrolyte and should prevent the electrodes from touching each other. This sounds easy but in practice much more components are needed to prepare a well-operating LIB such as current collectors, packaging materials and safety devices. In addition, several technologies for LIB assembly are possible. At laboratory scale mainly Swagelok cells, coin cells or simple pouch cells are used. Also, choosing the right materials for the individual components requires the careful consideration of many parameters that will be briefly discussed in the next chapters. In accordance to the topic of the master thesis I will go more deeply into anode materials.

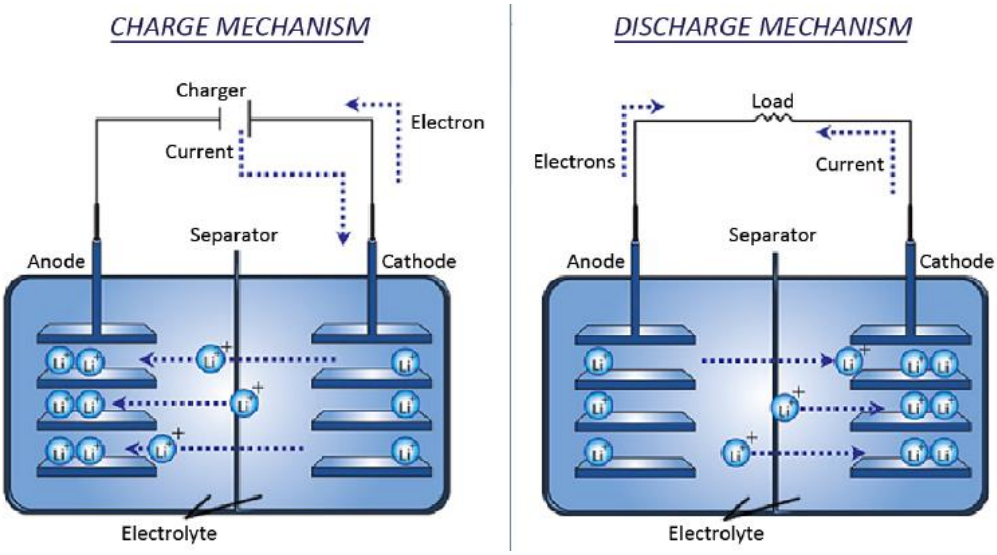

Figure 1. Simplified representation of a lithium ion battery during charging and discharging (Source: Omar et al.[6])

1.2. Electrolyte

The most important properties of an electrolyte for LIB are the high lithium ion conductivity and the low electronic conductivity. Commercial electrolytes for LIB usually consist out of carbonate-based aprotic solvents including a conducting salt like $LiPF_6$ and several additives. Usually a mixture of cyclic carbonate esters like propylene carbonate (PC) or ethylene carbonate (EC) and linear carbonate esters, such as diethyl carbonate (DEC) or dimethyl carbonate (DMC) are used [7]. The goal is to obtain the fastest possible Li-ion diffusion. Therefore, low viscosity and high ionic conductivity of the electrolyte are crucial. Cyclic carbonate esters in most cases have a high dielectric constant but a high viscosity. In contrast, linear carbonate esters have lower dielectric constants but also lower viscosities. That is why blending both delivers the best results [7].

Although there is a trend towards solid electrolytes, except for low-power devices and small batteries, up to now liquid electrolytes are still dominating the market [8]. This is because the conductivities of the organic electrolytes are exceeding most of the solid electrolytes. Also, larger lithium ion transfer resistances at the electrode-solid electrolyte interface prevent the solid state battery from reaching a sufficiently high power density [9]. Nevertheless, advantages like improved packaging efficiency, improved safety, high thermal stability or long cycle life are potentially game-changing features and research is still going on [9].

1.3. Cathode Materials

Cathode materials in lithium ion batteries usually consist out of a metal oxide host network that is able to store lithium reversibly and acts as the positive electrode. In some cases, also polyanionic compounds or chalcogenides are used as cathode materials. Inside the material lithium ion diffusion can occur in a one-, two-, or three-dimensional way. Table 1 shows the typical crystal structures of cathode materials, their dimensionality and associated examples.

Table 1. Typical metal oxide cathode materials classified by their crystal structure [4]

layered (2D)	spinel (3D)	olivine (1D)	tavorite (1D)
LCO ($LiCoO_2$)	LMO ($LiMn_2O_4$)	LFP ($LiFePO_4$)	$LiFeSO_4F$
$LiNiO_2$, $LiMnO_2$	$LiCo_2O_4$	$LiMnPO_4$	$LiVPO_4F$
$LiNi_{0.8}Co_{0.2}O_2$		$LiCoPO_4$	
NMO ($LiNi_{0.5}Mn_{0.5}O_2$)			
NMC			

Lithium cobalt oxide (LCO, $LiCoO_2$) was the first successful cathode material in commercial LIB. Although the market share has declined, in 2010 still 40% [7] of all batteries contained LCO electrodes and it's still used in many commercial LIB. LCO has a relatively high theoretical specific capacity of 274 mAh g^{-1} and a high theoretical volumetric capacity of 1363 mAh cm^{-3} [4] when all the lithium is cycled. However, in practice only 0.5 Li can be reversibly cycled per mol of LCO – this leads to practical capacities that are close to 140 mAh g^{-1}. Further disadvantages are related to the high cost of cobalt and its toxicity. Additionally, LCO is the metal oxide cathode with a relatively low thermal stability. Therefore, other materials have to be taken into consideration. NMO ($LiNi_{0.5}Mn_{0.5}O_2$) would evade the cobalt problem while keeping the energy density at a similar level [4]. Adding cobalt to the structure leads to NMC which possesses a higher structural stability [10]. Hence, NMC is widely used in commercial batteries. The spinel-type structured LMO is also used commercially due to economic and ecological reasons [11] although theoretical specific capacities (148 mAh g^{-1}) and theoretical volumetric capacities (596 mAh cm^{-3}) are lower than for the layered structures [4,7].

When it comes to the replacement of sealed lead acid batteries, lithium iron phosphates (LFP) are the material of choice. LFP batteries have slightly higher theoretical capacities than LCO (170 mAh g^{-1} and 589 mAh cm^{-3}) while having a lower but quite constant discharge voltage of 3.2 V (4 · 3.2 V placed in series – nominal voltage of 12.8 V). They are the safest form of all commercial cathode materials due to their thermal and chemical stability [12], they are cheaper than LCO, almost non-toxic and complete delithiation is possible.

1.4. Anode Materials

Since anode materials are the fundamental topic of this master thesis I will go into more detail on them now. Anode materials are the negative electrode in lithium ion batteries and take up the lithium ions during charge mode. It is important for the material to have a sufficient high specific capacity as well as a high volumetric capacity. Furthermore, the discharge profile should be flat so that the discharge capacity is almost independent of the cut-off voltage [13].

$$Energy\,[Wh] = Capacity\,[Ah] \cdot Voltage\,[V] \tag{1}$$

The material should also enable fast lithium ion diffusion to make it possible to charge/ discharge at higher rates. The diffusivity is often expressed in terms of the Li-ion diffusion coefficient (D_{Li+}) that can be used to determine how far a lithium ion

can diffuse, on average, in a given time. Slower diffusion can be compensated by the use of nanostructured materials which reduce the charge carrier transport lengths.

For electrodes in general it is also important to be a good electron conductor. They should be thermally and chemically stable and the expansion during lithiation should be minimized to avoid cracking and crumbling. Last but not least, the materials should be available and economically viable.

The major advantages of lithium itself as anode material are the high specific capacity of 3860 mAh/g [14] and the low reduction potential, allowing to reach high cell voltages. Nevertheless, pure lithium metal is not used as anode material in practise because it tends to form lithium dendrites during cycling. This can cause local short circuits and a subsequent thermal run-away which is undesirable in any application.

However, the commercial breakthrough of rechargeable lithium ion batteries occurred with the use of anode materials without any metallic lithium. Instead of the metal, graphite or other carbon-based materials as well as transition metal oxides or intermetallic compounds have been used [4].

1.4.1. Graphite

Graphite consists out of a stack of several graphene planes and enables the lithium ions to intercalate between those planes. Fully lithiated graphite has the two-dimensional structure LiC_6. Therefore, volume changes (~10%) are kept to a minimum [4] and the material possesses a high cycle life. The material is an electron conductor due to the presence of delocalised electrons and the conductivity increases even more by taking up electrons during the intercalation of positive charge carriers. Graphite has the advantages of being abundant, available and cheap. It has a low delithiation potential vs. lithium and power and energy density are sufficiently high as well. Although the volumetric capacity is relatively low with 330-430 mAh cm^{-3} the specific capacity of graphite is higher than in most cathode materials [4]. Many variations of graphite exist in order to increase the capacity [7]. The most economic one is natural graphite which is also the most used anode material on the LIB market in a modified way (see Figure 2). The modification is necessary to prevent the electrode from reacting with the electrolyte. Additionally lithium plating is an issue with regard to the carbon based anode materials [15].

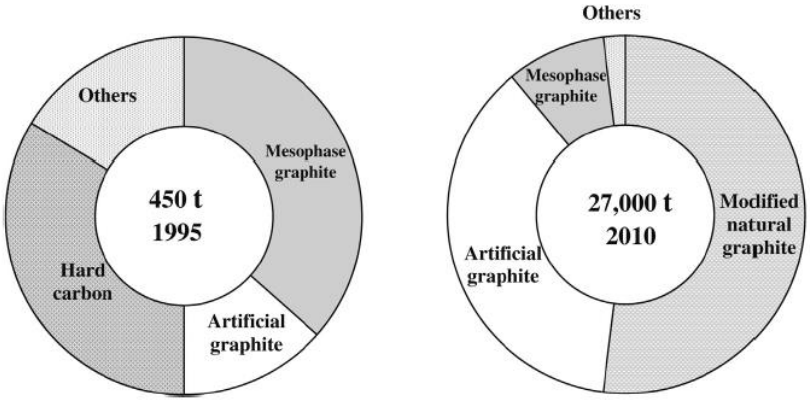

Figure 2. Distribution of the most common anode materials on the lithium ion battery market [7]

1.4.2. Metals and Intermetallic Compounds

Although graphite has the lowest potential vs. Li/Li^+ (see Figure 3) which is crucial for a high cell voltage and thus also for high energy density, research tends towards the investigation on other materials to be used as negative electrode because the capacity of graphite has already reached practically its theoretical limit [16] of 372 mAh g^{-1}.

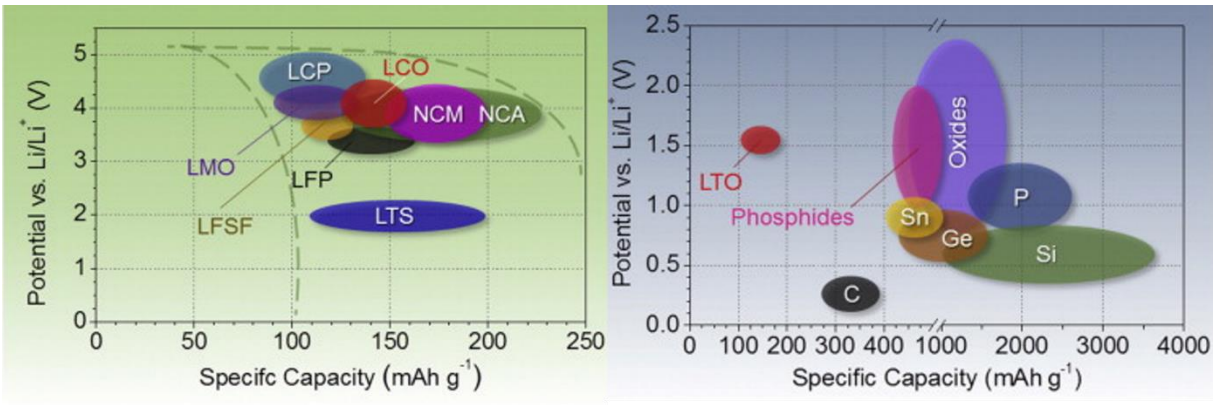

Figure 3. Approximate range of some experimental, specific capacities and average discharge potentials of common cathode materials (left, in green) and anode materials (right, in blue) (Source: Nitta et al. [4])

1.4.2.1. Lithium Alloy Anodes [4]

Metals like Sn, Sb, Si, Zn, Cd, Ge and others have the ability to form alloys with lithium at sufficient low potentials (usually <1 V vs. Li/Li^+).

$$Li_xM \underset{charge}{\overset{discharge}{\rightleftarrows}} xLi^+ + xe^- + M \tag{2}$$

Depending on the stoichiometry large specific and volumetric capacities can be reached, higher than those of graphite, but the materials are also known for their extreme volume changes which can be several times the original volume. The volume changes are given in Table 2 for a selection of materials. This volume expansion is accompanied by cracking and crumbling of the material. Particles are detaching from the current collector and loose contact. New surface is formed by the fractured particles leading to further SEI formation accompanied by the decomposition of the electrolyte. Consequently, the volume expansion is not only a matter of space limitation in the cell but also the reason for capacity fading during cycling until the electrode breaks down.

Silicon is the most studied element of the alloying materials due to its relatively low delithiation potential (see Figure 3) and the extremely high volumetric and specific capacity [4]. Due to the different stoichiometries appearing during alloy formation there is no distinct potential at which alloying takes place. The multialloying mechanism is noticeable as broad peak or several peaks overlapping in the cyclic voltammogram.

Tin has also received some attention due to its similar properties to silicon and the increased electrical conductivity. However, tin tends to suffer from easy fracturing. Germanium is way too expensive for commercial usage. Zinc is cost effective and its natural abundance is quite high, but fracturing is an issue as well and the specific capacity is significantly lower than for the other alloying metals. Antimony and lead can be excluded due to the toxicity of the elements. Table 2 and Figure 4 give a rough overview of the different alloy electrodes and their properties and allows comparison with other negative electrodes such as metallic lithium, graphite or LTO.

Table 2. Comparison between different Li-alloying materials as well as graphite and LTO with regard to their theoretical specific capacity, theoretical volumetric capacity, volume expansion after lithium alloy formation and onset potential [13, 15,17,18]

Material		**Sn**	**Si**	**Sb**	**Zn**	**Mg**
Phase		$Li_{4.4}Sn$	$Li_{4.4}Si$	Li_3Sb	LiZn	Li_3Mg
Theor. specific capacity	mAh g^{-1}	993	4200	660	410	3350
Theor. volum. capacity	mAh cm^{-3}	7246	9786	4422	2923	4355
Volume expansion	%	260	300	200	n.g.	100
Onset potential	V vs. Li/Li^+	0.6	0..4	0.9	0.1	0.1

Material		**Al**	**Li**	**Graphite**	**LTO**
Phase		LiAl	Li	LiC_6	$Li_7Ti_5O_{12}$
Theor. specific capacity	mAh g^{-1}	993	3862	372	175
Theor. volum. capacity	mAh cm^{-3}	2681	2047	837	613
Volume expansion	%	96	100	12	1
Onset potential	V vs. Li/Li^+	0.3	0	0.05	1.60

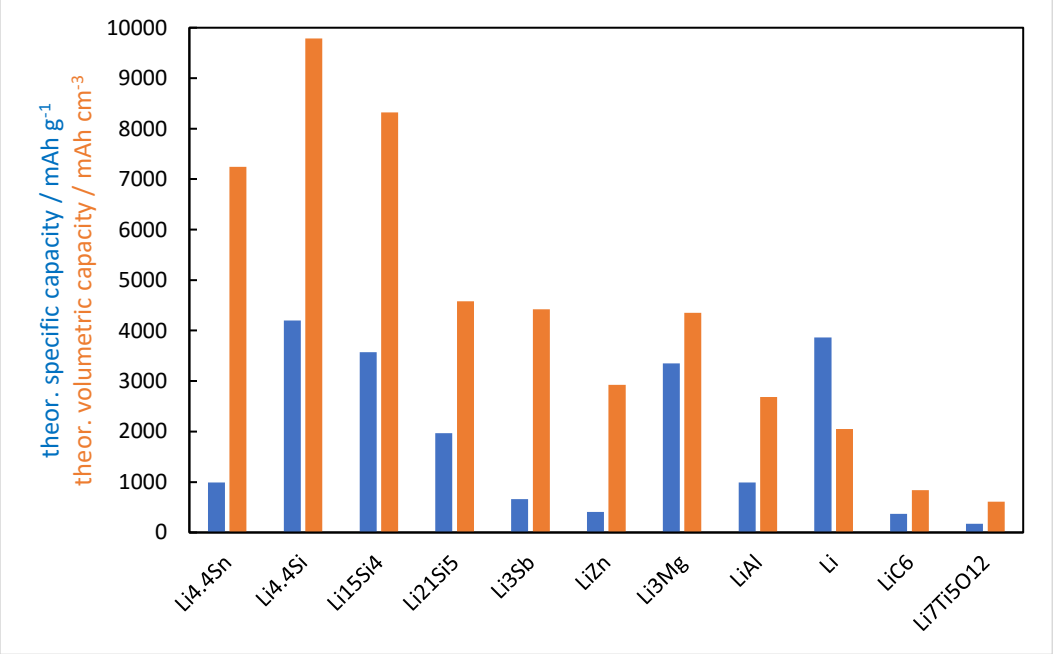

Figure 4. Block diagram comparing the capacities of several anode materials for lithium ion batteries, all capacities are the theoretical ones and may differ from practice, the phases given represent the theoretical composition after complete lithiation [4,13,15,17,18]

1.4.2.2. Intermetallic Alloy Electrodes of the type M_xM_y

One possibility to overcome the problems arising from the volume changes during cycling is the use of intermetallic compounds [1] or composite host materials of the type M_xM_y, where M_x is active regarding the alloy reaction with lithium and can be one of the metals described in the previous chapter. M_y is inactive or less active and should perform as a buffer to compensate the expansion and contraction of the reactant.

One extensively studied intermetallic alloy is the system Sn_xCu_y which has provided a much longer cycle life in comparison to pure Sn electrodes and capacities of approximately 300 mAh g^{-1} with high coulombic efficiencies when tested in lithium half cells [19]. Amorphous Sn-Co nanoparticles with the addition of carbon are even commercialized by SONY as negative active material in the Nexelion™ LIB and have the advantage of higher volumetric capacities than conventional LIB [20].

1.4.2.3. Cu-Zn Alloys

Due to a possible future shortage of Sn and the related cost issues, Sn should be replaced by metals with a higher natural abundance when it comes to the usage in commercially produced LIB. Studies by Varzi et al. [1] have shown that Zn could be a promising alternative. In theory specific capacities of about 410 mAh g^{-1} can be estimated. Again, the pure metal itself suffers from cracking and crumbling. The cycling stability would be insufficient. The addition of Cu improves the stability and would lead to an increase in electric conductivity which is favourable for the use as electrode.

When it comes to electrochemical behaviour, $Cu_{18}Zn_{82}$ has shown the best performance [1]. The Zn-rich alloy can sustain current densities of about 10 A g^{-1} without significant damage while graphite already fails at 5 A g^{-1}. Furthermore, the material shows a promising capacity retention over 500 cycles and has an excellent low temperature behaviour. The latter aspect is visible during galvanostatic cycling with a constant current rate of 0.1 A g^{-1} which shows rather constant capacities of roughly 200 mAh g^{-1} at -20 °C and still 137 mAh g^{-1} at -30 °C, where commercial graphite already fails [1] as shown in Figure 5.

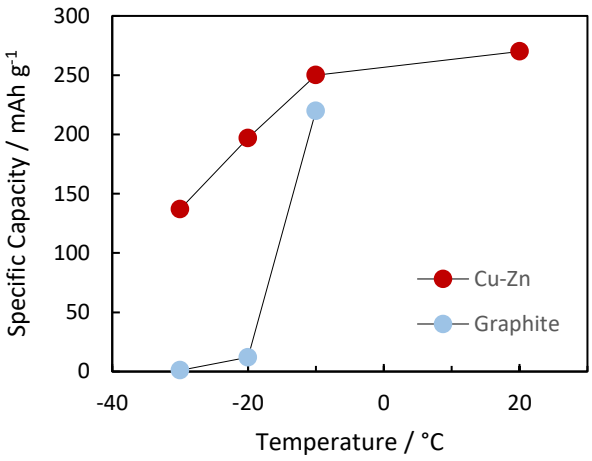

Figure 5. Low temperature behaviour of the electrodeposited Cu-Zn alloy in comparison to commercial graphite when tested in lithium half cells (Source: Varzi et al. [1])

1.4.3. Nanostructured Electrode Materials [20]

In specific cases it is possible to improve the properties of the active material using nanostructuration. The smaller structures automatically lead to a larger surface area to volume ratio and thus also to shorter diffusion pathways for lithium ions inside the electrode material, which in turn may result in an enhanced rate capability. In addition, nanoscale structured materials are often better in the compensation of volume changes triggered by the insertion or removal of lithium which in turn increases the electrode's lifetime and cycle stability.

One disadvantage of the high surface of the structures is the increased tendency towards irreversible surface reactions leading to the consumption of lithium and electrolyte. Furthermore, the low density in comparison to a bulk material leads to lower volumetric capacities.

In summary, the cycle stability can be increased although one has to cope with the higher volume electrodes to obtain the same capacity and the preparation of nanomaterials that is usually difficult and more expensive than for the bulk type. Nevertheless, nanostructuring of active material is sometimes a crucial point. In LTO, for instance, nanoparticles lead to an enhancement of Li-ion diffusion and nanostructured silicon or nanocomposites containing silicon show better cycling stability in comparison to bulk silicon. Nanoscale thick silicon films can retain capacity after hundreds of cycles. Other lithium alloy electrodes have been less studied. In general, nearly all metals show some improvement in their nanostructured form except aluminium which shows poorer performance when scaled down to the nanosized particles due to the formation of an oxide layer on the surface.

1.4.4. Titania

LTO and various forms of TiO_2 can also be used as negative electrodes. Lithium insertion and removal occurs between 1.5 and 2.0 V vs. Li/Li^+ which is quite high when compared to other anode material [20]. The high lithiation potential results in a lower cell voltage but has the advantage that there is no problem with exceeding the stability window of typical electrolytes and the danger of lithium plating can be excluded. Also, the extent of passivation layer (SEI) formation is expected to be very low. Hence, there are less penalties induced by thick SEI layers resulting in improved kinetic properties [21].

The spinel-type compound $Li_4Ti_5O_{12}$ (LTO) is lithiated at a potential of 1.55 V vs. Li/Li^+ to the rock salt type $Li_7Ti_5O_{12}$ (see eqn. 4) The high operating potential ensures safe operation conditions. However, lithium transport inside the material is relatively slow and therefore nanostructuring the material is inevitable to obtain high rate cycling performance as expected from LTO material. This material has low theoretical capacity [20] of 175 mAh g^{-1} and the low electronic conductivity [22] of 10^{-13} S cm^{-1} which affect performance at high rates.

Also, lots of polymorphs of titanium dioxide are able to insert lithium at certain potentials (potential ranges) whereby theoretical capacities are exceeding those of LTO (336 mAh g^{-1} for $LiTiO_2$ vs. 175 mAh g^{-1} for LTO). Nevertheless, exploitation of the whole capacity is very challenging [22] and therefore the overall performance is insufficient in many cases.

$$in\ theory: TiO_2 + Li^+ + e^- \rightleftharpoons LiTiO_2 \qquad (3)$$
$$in\ practice: TiO_2 + x\ Li^+ + x\ e^- \rightleftharpoons Li_xTiO_2$$
$$x < 1$$
$$x \approx 0.5 \text{ for anatase[24,25] or rutile[26,27]}$$
$$x \approx 1 \text{ for } TiO_2\text{(B) [27,28]}$$

$$Li_4Ti_5O_{12} + 3\ Li^+ + 3\ e^- \rightleftharpoons Li_7Ti_5O_{12} \qquad (4)$$

Titania possesses several advantages such as high abundance, high chemical stability and structural diversity. The lithium insertion process in titania usually depends on its particle size, structure and crystallinity [22]. Once again, downscaling leads to increased capacity and rate capability.

In amorphous titania, lithium insertion takes place over a large potential range whereas there are distinct lithiation potentials, resulting in potential plateaus, in the case of LTO or anatase TiO_2 [23]. Anatase is considered to be the most (electronic) conductive and electroactive phase of TiO_2 in the voltage range of 1-3 V [26]. During lithium ion insertion (see eqn. 3) anatase undergoes a phase transformation from the tetragonal anatase phase to the lithium rich orthorhombic phase. The good ionic conductivity of the material is caused by free octahedral and tetrahedral sites inside the tetragonal structure of crystalline anatase [21]. Concerning anatase, lithium insertion is only possible to an extent of 0.5 Li per TiO_2 molecule (see eqn. 3) leading to a theoretical capacity [24] of 168 mAh g^{-1} which is similar to the theoretical capacity of LTO.

Nanowires [29] and nanotubes [28] made out of TiO_2-B have shown slightly higher capacities, but it is uncertain whether the material can compete with LTO with regard to the long-term cycling stability. Further development in terms of power density and cycling life is achieved by the combination of titania nanostructures with carbon nanotubes or graphene to increase the conductivity of the material [30,31]. TiO_2 nanotubes built on a graphene layer [32], for instance, show constant capacity values of 300 mAh g^{-1} over thousands of cycles when cycled with current loads of 10 mA g^{-1} up to 8 A g^{-1}.

1.4.5. TiO_2 Nanotubes

As already mentioned in the previous chapter the properties of titania can be drastically improved by downscaling the material and increasing the specific surface area [23]. That is why nanostructured titania and self-organized titania nanotubes in particular attracted lots of interest in the past. When nanostructured, the material shows different electronic properties (e.g. from quantum confinement effects, surface curvature etc.) than in the bulk form. These effects also change the interaction of the titania with the surrounding, leading to different kinetics. Since the band gap is different for surfaces (or grain boundaries) than for the bulk, also the electric conductivity varies with the size of the grains [33]. An increased number of crystallographic defects in the former areas causes this variation.

Although, titania spherical nanoparticles itself would already lead to an increased surface area and the associated new properties, other nanosized geometries like nanorods or nanotubes are preferred due to a better control of the chemical and physical behaviour [34,35]. Titania nanotubes are non-toxic and environmentally friendly, available, resistant to most chemicals, mechanically stable and the electrochemical preparation of the highly ordered nanotubular structure is rather inexpensive and fairly simple [21,36].

Depending on the crystalline modification (anatase, rutile, brookite, TiO_2-B), titania is a wide-gap semiconductor with a band gap between 3.0 and 3.2 eV and suitable band-edge positions for the use in photocatalytic reactions or in solar cells [34]. The one dimensional (1D) TiO_2 nanotubes are already used to design dye-sensitized solar cells [37]. The band gap can be tuned by doping with nitrogen, carbon, Sn [38] or other elements. Doping of TiO_2 with V and Cr was reported to be effective in activating a response to visible light [39].

1.4.5.1. Preparation Methods

Nanotubular titania is a promising candidate for the use as a non-harmful anode material in lithium ion batteries [40]. The synthesis of one-dimensional titania nanostructures can be achieved with several methods including sol-gel methods, hydrothermal approaches, template-assisted methods or electrochemically via anodization in non-aqueous electrolytes [34].

Apart from anodization, all of these techniques lead to single tubes with variable tube length or agglomerates of tubes which are dispersed in a solution. For the use in electronic devices the tubes have to be connected to a conducting surface. This connection is mainly done by compacting the tubes in layers on the respective surface leading to a random orientation of the single tubes [34] as shown in Figure 6. The one-dimensionality is no longer given.

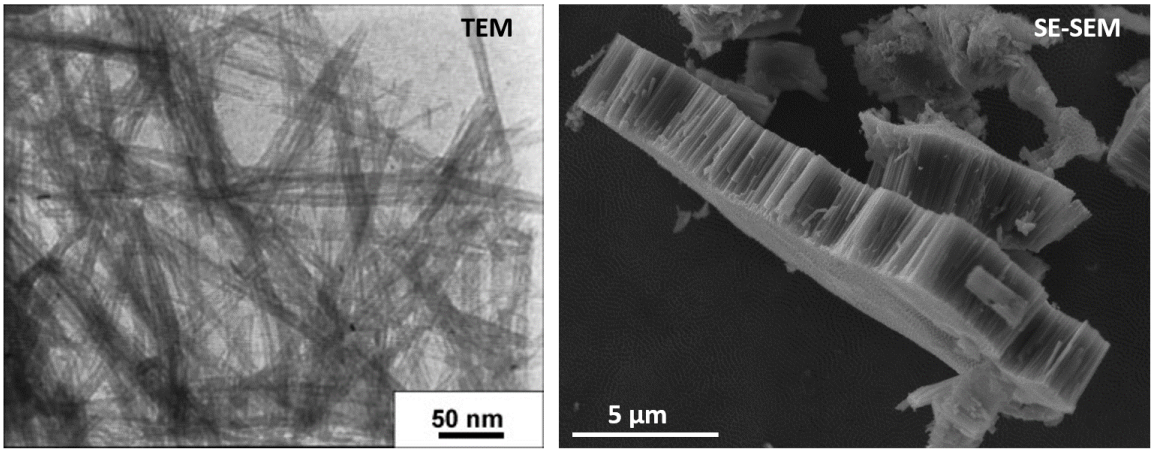

Figure 6. TEM image of randomly oriented titania nanotubes synthesized by Xu et al. using a hydrothermal process [40] (left) and secondary electron SEM image of self-assembled TNT prepared via anodization on a titanium substrate as part of this thesis (right)

By electrochemical oxidation (anodization), nanotubes perpendicular to the substrate can be produced. This self-assembly method allows the dimensions of the nanotubes to be controlled by adjusting the synthesis conditions. The dimensions may vary between 30 and 200 nm with regard to the diameter and for the lengths between

200 nm and 1000 µm when anodized in fluoride containing, non-aqueous environment [41,42] (e.g. ethylene glycol). The first experiments for the preparation of titania nanotubes via anodization were carried out in fluoride containing, acidic, aqueous solutions by Zwilling et al. [43,44]. The attempt was successful although the as-prepared material showed side wall inhomogeneities [45] and no highly organized structure could be achieved. Later it was shown that highly parallel self-organized structures containing almost ideal hexagonally arranged tubes [46] could be prepared in organic electrolytes, like ethylene glycol.

In non-aqueous solvents the anodization is carried out at a constant voltage between 5-150 V. As a substrate, pure titanium foil or titanium covered surfaces can be used. The concentration of fluoride ions is important to achieve the desired result and should be between 0.1 and 1 wt%. If the fluoride content is lower than 0.05 wt% a compact oxide layer without the existence of any pores or tubes is formed according to equations 5a-6 [34]. First, the titanium is oxidized to Ti^{4+} and reacts with O^{2-} created by field-aided deprotonation of water.

$$M \longrightarrow M^{z+} + z\, e^- \tag{5a}$$

$$M^{z+} + z\ H_2O \longrightarrow M(OH)_z + z\, H^+ \tag{5b}$$

$$M(OH)_z \longrightarrow MO_{z/2} + \frac{z}{2}\ H_2O \tag{5c}$$

$$M + \frac{z}{2}\ H_2O \longrightarrow MO_{z/2} + z\, H^+ + z\, e^- \tag{5}$$

Depending on the migration rate of Ti^{4+} and O^{2-} the growth of new TiO_2 either occurs at the interface between oxide and electrolyte or between the oxide and the titanium substrate. The latter is the predominant process in most experiments. With increasing oxide layer thickness, the current decreases exponentially with the time due to the higher resistances. The maximum possible film thickness is dependent on the anodization voltage.

The counter reaction of the oxide layer formation is the reductive hydrogen formation at the cathode.

$$z\ H_2O + z\, e^- \longrightarrow \frac{z}{2} H_2 \uparrow\ + z\, OH^- \tag{6}$$

The addition of more fluoride to the electrolyte would lead to self-assembled nanotube formation according to equations 7 and 8. The fluoride forms complexes with the Ti^{4+} that is migrated through the oxide layer to the oxide electrolyte interface after oxidation and in addition chemically attacks the as-formed TiO_2 layer.

$$Ti^{4+} + 6\,F^- \longrightarrow [TiF_6]^{2-} \tag{7}$$

$$TiO_2 + 6\,F^- \xrightarrow{H^+} [TiF_6]^{2-} + 2\,H_2O \tag{8}$$

For concentrations between 0.1 and 1 wt% F^- there is a competition between oxide formation and complexation leading to the desired structures. Figure 7 shows a rough schematic of the formation of bulk in contrast to nanotubular titania. A more detailed description of the mechanisms occurring during anodization of titanium is given by Roy et al. [34]

In contrast, concentrations higher than 1 wt% would lead to a so called electropolishing of the sample and no oxide is formed at all since all of the free Ti^{4+} forms complexes with the fluoride and no Ti^{4+} is available for titanium oxide formation anymore [45].

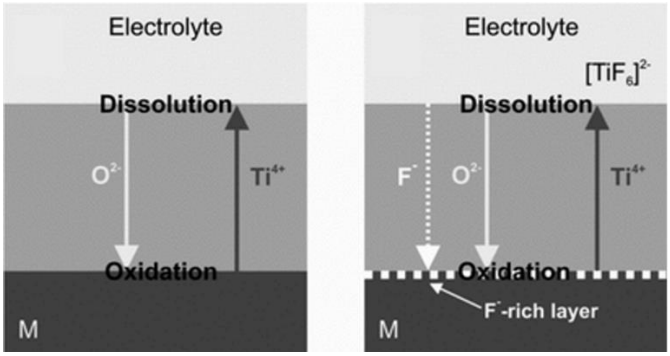

Figure 7. Schematic drawing showing the titanium substrate (M), the oxide layer at the interface and the electrolyte as well as the field-aided transport of the mobile ions through the oxide layer during the formation of a compact oxide layer in fluoride-free electrolytes (left) and during porous/tubular oxide formation in the presence of fluoride (right) (Source: Roy et al. [34])

As already mentioned, the geometry of the tubes can be influenced by the synthesis conditions. While the tube length depends on the etching rate and anodization time, the tube diameter can be adjusted by changing the applied voltage. The diameter increases linearly with the voltage whereby the rate of growth depends on the electrolyte, being smaller for the less-conductive organic electrolytes due to higher IR-drops [34].

1.4.5.2. Usage of Pulsed Current Electrodeposition to Deposit Various Metals into the Inner Volume of Titania Nanotubes

The properties of the as-prepared titania nanotubes can be modified by further tuning through the introduction of other elements (doping) or by annealing in order to convert the amorphous structures to their crystalline counterpart rutile or anatase. Another possibility would be to use the TNT structure as a substrate for further loading with another electroactive material such as semiconductors (e.g. CdS [47], Cu_2O [48], $ZnFe_2O_4$ [49]) or metals (e.g. Cu [50], Ni [51], Sn [36], Ag [52], Pt [53]…). Filling the tubes with Fe_3O_4 for instance can introduce magnetic properties [54]. Such magnetic tubes can be applied in guiding and release systems.

Although, so far, numerous approaches for the deposition of various materials in the inner volume of TiO_2 nanotubes have been reported, the most economically viable method to fill the nanotubes is probably electrodeposition. For the n-type semiconductor [34] titania it is not possible to use the traditional approach used for insulators where the deposition starts at the conductive bottom and the tube is then filled up from this point. Electrodeposition of compounds inside titania nanotubes was achieved using the so called pulsed current approach [36].

After anodization, the nanotubes were further subjected to an anodic treatment (solution of ethylene glycol and H_3PO_4) to seal defects. Defects or cracks at the bottom can be related to the F^-- rich layer which is situated at the bottom of the titania nanotubes and weaken the chemical and mechanical stability of the structure [34,55]. The sealing step is followed by a first current pulse which should lead to a homogeneous distribution of nuclei all over the tube walls. The nuclei grow further with an increasing number of pulses until the whole volume is filled [55]. However, to our knowledge, the mechanism is not completely clear up to now.

When filled with an element that is active towards lithium insertion as for instance Sn or Sb, the nanotubes can also be used as anode material in lithium ion batteries. The encapsulation of the nanosized metal particles is expected to prevent the coalescence to larger species and thus increases the cycle life and capacity retention of the electrode [36].

1.5. Methods and Techniques

1.5.1. Scanning Electron Microscopy (SEM) [56,57]

Optical microscopy is limited by the wavelength of optical light. When particles smaller than 400-700 nm should be observed, electron microscopy is the technique of choice. Depending on the setup, structures in the size of a few Ångstrom can be imaged and morphological as well as compositional information can be obtained. The setup of an electron microscope is rather similar to an optical microscope with the exception that the source are electrons and the optical lenses are replaced by electromagnetic lenses which focus the electrons by either a magnetic or an electrostatic field.

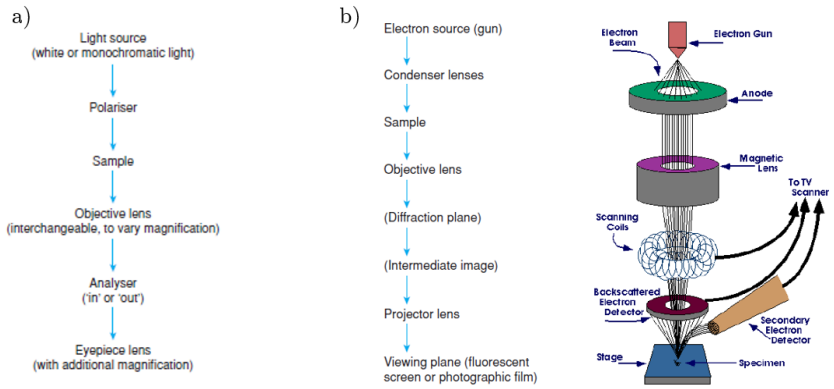

Figure 8. Basic components of an optical polarising microscope (a) and an electron microscope (b) (Source: Anthony et.al [56] and Purdue University [90])

The electrons are either thermionically emitted by a tungsten filament or a lanthanum hexaboride cathode and are accelerated towards the anode. Field emission is also a possible technique (although more expensive) for the generation of electrons and leads to an improved signal-to-noise ratio and higher spatial resolution when compared to thermionic devices.

In scanning electron microscopy (SEM) the beam which has an initial energy from a few hundred eV up to 100 keV and which is focused to a very small focal spot in the size of 0.4 nm − 5 nm, scans along the surface in a raster-like manner. The resolution limit corresponding to the wavelength of the electrons can be calculated from the acceleration voltage V as follows:

$$\lambda = \frac{h}{\sqrt{2\,m\,e\,V}} = \frac{12.3}{\sqrt{V}}\ [\text{Å}] \tag{9}$$

When the electron penetrates into the material it undergoes several elastic and inelastic collisions within a drop-shaped interaction volume of the size of 100 nm-5 µm depending on the energy of the electron and the material (see Figure 9). Non-conducting samples have to be covered with a thin layer of metal to avoid local charging effects of the sample.

There are several signals possible to be measured with SEM. Detecting the electrons which escape from the material after several elastic collisions is referred to as backscattered electron SEM. The BSE have energies higher than 50 eV which is about 80% of their original energy and are coming from the first 300 nm of the sample, depending on the acceleration voltage and the specimen (see Figure 9). The higher the atomic number of the element the more electrons are scattered back, which in turn leads to a stronger signal and thus to bright spots in the resulting image. Consequently, BSE SEM can give you information about the elemental composition if the difference in atomic number is high enough. The detector, visible in Figure 8b, is located straight above the specimen and collects the electrons which are scattered back in the given direction.

Secondary electrons (SE) are generated when the incoming electron transmits a part of its energy to a specimen's electron during an inelastic collision. The atom is then in an excited state and an electron, the secondary electron, possessing an energy of less than 50 eV is emitted. Due to the lower energy, the penetration depth of SE is lower than for instance for the more energetic BSE, leading to a smaller interaction volume and a better resolution. SE as well as BSE are then drawn in by the use of a positively charged anode or Faraday cup towards the scintillator and contribute to the signal. The SE detector is located perpendicularly to the incident beam and is shown as brownish tube in Figure 8b. Thus, a surface tilted towards the detector emits more SE that can be captured by the detector than a surface normal to the incident beam resulting in an image representing the morphology of the specimen.

By the collision of an electron with other atoms, X-rays or Auger electrons can be generated. Via an energy dispersive X-ray analyser (EDX), information upon the atomic composition of the sample can be obtained. The X-rays are generated when an electron from an outer, higher energy shell "drops down" to fill a vacancy in an energetic lower shell which was previously produced by the release of a secondary electron. The difference in energy is then released in form of X-rays and is characteristic of the emitting element. EDX is useful to get an impression of the elements present in the sample although an exact determination is not possible and variations in the order of 10% (detection limit of 1000-3000 ppm) have to be taken into account. It is also important to know that there is a drastic loss in sensitivity for light elements.

If the excess energy is transmitted to a third electron from an outer shell which is subsequent ejected, the released electron is called Auger electron. The energy of the Auger electron is again characteristic for the respective element. The interaction volumes from which the different signals are emitted are shown in Figure 9. Further effects related to the incoming electron beam may be heating by the excitation of lattice vibrations or structural changes known as radiation damage [56].

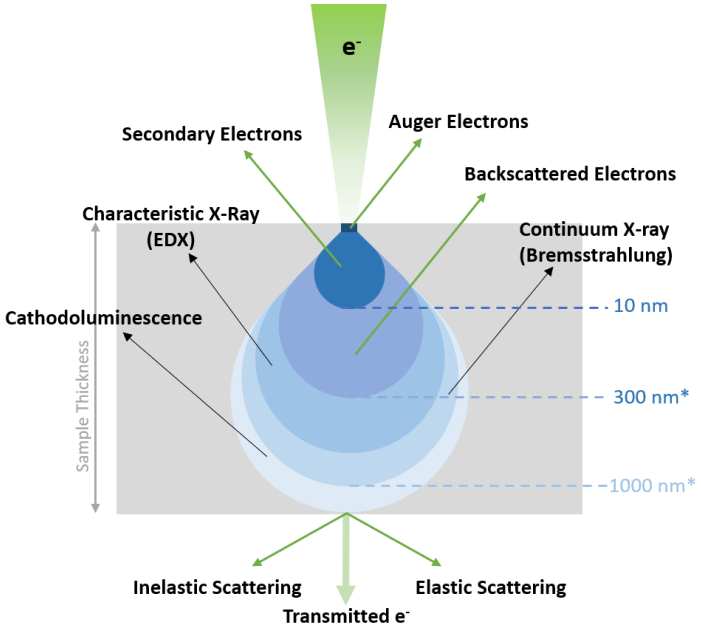

Figure 9. Specimen interaction volume and corresponding signals emitted from specific regions of the interaction volume. *depth depends on accelerating voltage of the incoming electrons and density of the specimen

1.5.2. Cyclic Voltammetry (CV) [58–60]

Cyclic voltammetry is a promising tool for the acquisition of information about electrochemical reactions. The technique provides information about simple as well as more complicated redox systems including kinetic parameters. In terms of LIB one gets information about the processes occurring during lithium insertion and deinsertion, about the reversibility and stability, about SEI formation or possible side reactions inside the cell and much more.

The setup comprises three electrodes. In the case of the lithium half-cells dealt with in this thesis, the counter and reference electrode consist out of lithium metal whereby the working electrode is the electrode material of interest. Basically, in cyclic voltammetry a voltage is applied to the system and the potential of the working electrode is varied linearly with the time within two fixed values while the current response is measured [59]. The fixed rate at which the voltage is changed, is called sweep rate or scan rate and has to be adapted to the experiment. Figure 10 shows the exemplary course of current and potential during a CV experiment. While the

course of potential is controlled by the set-up, the corresponding current provides information about the reactions occurring in/ at the working electrode.

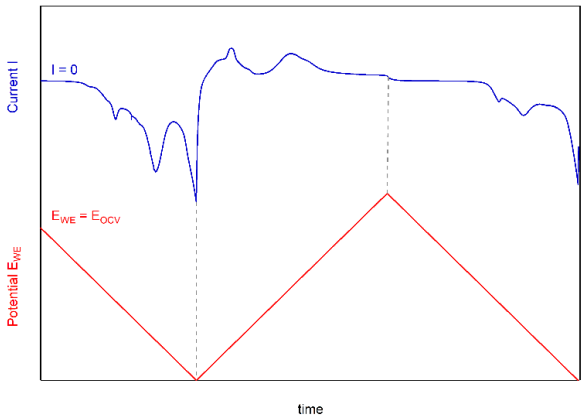

Figure 10. Time dependent voltage curve (red) and current curve (blue) showing 1.5 cycles scanned with a constant potential scan rate. The data is taken out of a CV measurement of a lithium half-cell from this thesis. The first scan shows irreversible current responses due to SEI formation

If a charge transfer process takes place at a certain potential this charge flow is expressed as a current signal in the CV. Processes that are limited by diffusion, such as the lithium insertion in the solid anode material, proceed very slow. Therefore, studying these processes requires very low scan rates, typically smaller than 1 mV s^{-1}. If the scan rates are too fast, the processes might occur outside the time scale and are not visible anymore.

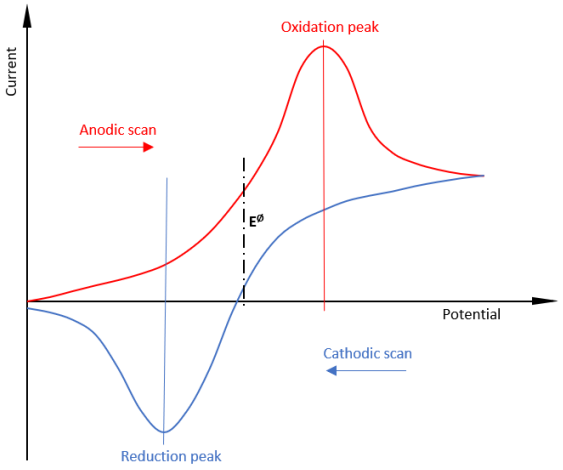

Figure 11. Current-potential curve from a cyclic voltammetry experiment with one anodic and one cathodic scan of a highly reversible redox-couple

Figure 11 shows a typical CV of a reversible redox reaction. As a starting point you can choose the open circuit voltage or a defined value. In this case the lower vertex potential is chosen as a start where only the reduced species is present.

When scanning in anodic direction the current slightly increases. This may be originated from non-Faradaic currents which are basically independent from any electrochemical reaction and can be caused by migration, reorientation of solvent dipoles or charging of the electric double layer at the electrode. This current usually appears during the whole measurement and is therefore referred to as background current. In addition, a Faradaic current begins to flow around the equilibrium potential of the oxidation reaction. A peak current can be recorded followed by a current decay afterwards due to a lack of available reactant. After the second vertex potential the scanning direction is reversed, the oxidation reaction slows down until the reduction of the oxidized species takes place.

For a reversible, single electron transfer reaction, like it should be for lithium, the CV shows certain characteristics [58,60].

- The current peaks are separated by ~59 mV for a single electron process – when electron transfer is too slow and Nernst equation is not applicable anymore ΔV is higher
- The formal potential $E^{\emptyset}$ is located in the middle of the oxidation peak potential and the reduction peak potential (see Figure 11) – identification of the electroactive redox couple possible

$$E_{an.peak} - E_{cat.peak} = \frac{59\,mV}{n}\ at\ T = 25°C \quad n \ldots . number\ of\ electrons \qquad (10)$$

- The ratio of the peak currents (referred to a correctly chosen baseline) is 1
- The peak currents are proportional to the square root of the scan rate (Randles-Sevcik)

According to Randles and Sevcik the Faradaic current increases linearly with the square root of the sweep rate:

$$i_{peak,faradaic} = 0.4958\,n\,F\,A\,c\,\sqrt{\frac{\alpha\,n\,F\,D\,v}{R\,T}} = const.\ \cdot\sqrt{v} \qquad (11a)$$

Plotting the peak current, where the diffusional current is the highest, against $\sqrt{v}$ should lead to a linear function. If all other parameters of equation 11a are known the chemical macroscopic diffusion coefficient D can be estimated from the slope.

Since there is always a non-Faradaic current (see eqn. 11b) contributing to the whole current response, a correction is necessary. In comparison to Faradaic current the non-Faradaic current is directly proportional to the sweep rate and increases therefore faster with increasing scan rate leading to a higher share of non-Faradaic current at fast scan rates [58].

$$|i_{cap}| = A\, C_d\, \nu \tag{11b}$$

$$\frac{|i_{cap}|}{i_{faradaic}} = \frac{C_d \sqrt{\nu}\, 10^{-5}}{2.7\, n \sqrt{n\, D}\, c} \tag{11}$$

From eqn. 11 you can see that for high scan rates or low concentrations of electroactive redox centres the contribution of capacitive current increases drastically. Using the Trasatti method [61] one has the possibility to differentiate between the capacitive current and the Faradaic current resulting from the redox reactions.

$$I(V) = k_1 \nu + k_2 \sqrt{\nu} \tag{12a}$$

$$\frac{I(V)}{\sqrt{\nu}} = k_1 \sqrt{\nu} + k_2 \tag{12}$$

Here, $k_1 \nu$ represents the Faradaic current due to surface capacitive effects and $k_2 \sqrt{\nu}$ the Faradaic current coming from redox reactions.

1.5.3. Galvanostatic Cycling with Potential Limitation (GCPL) [59,62]

GCPL is a constant current method widely used for the examination of battery characteristics. It measures the voltage over the time while keeping the current constant. Charge and discharge processes (negative or positive currents) are alternating when a certain pre-set lower or upper potential limit is reached. Information about the capacity retention, rate capability, long-term stability or reversibility of a charge-discharge process is acquired.

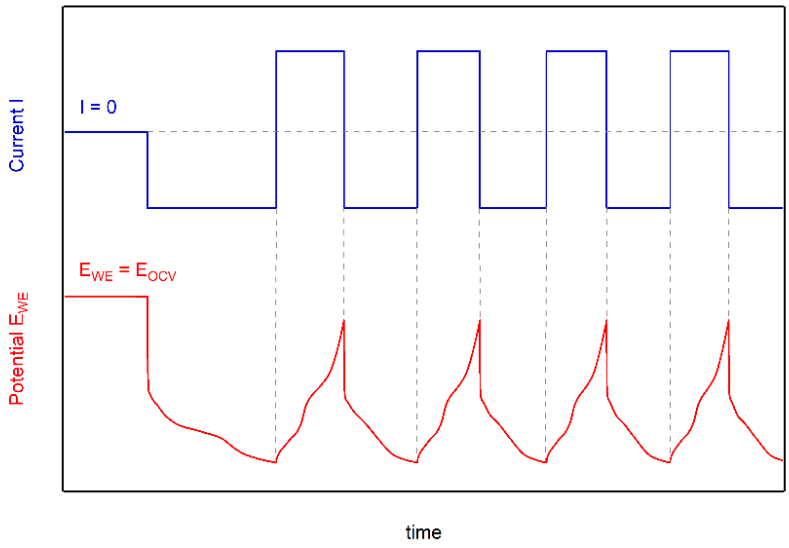

Figure 12. Potential (red) and current (blue) response of a cyclic chronopotentiometry with constant charge/ discharge rates

Figure 12 shows some cycling data of a lithium half-cell. The measurement is started at the open circuit voltage of the cell, followed by discharging (lithium insertion) with a constant rate. Potential limits are set in order to avoid side reactions such as oxidative decomposition of the electrolyte as well as lithium plating. Of course, the potentials limits have to match the electroactive potential range of the material. Here, it was cycled between 0.005 V and 2.5 V. If any electroactive compound is present, an electrochemical reaction will take place which is usually visible as plateau or flattening of the E_{WE}t-curve at the respective potential. When there are no more electroactive species to react, the potential further decreases to a potential where the next oxidation occurs and so on, until the lower limit is reached. Afterwards charging starts, again with a constant current rate, but this time a positive current is applied. Lithium is deinserted and diffuses back towards the metallic lithium anode. Again, a concentration gradient is formed and as soon as all of the reactant is consumed the potential increases until the upper potential limit is reached. Then the process is repeated.

$$Q(t) = \int I(t)\, dt \tag{13}$$

According to equation 13 the discharge and charge capacity of the regarding electrode can be calculated from the passed current and time.

Knowing the capacities, the coulombic efficiency can be determined as follows:

$$\frac{Q_{Li\_out}}{Q_{Li\_in}} \cdot 100 = Coulombic\ efficiency\ (\%) \tag{14}$$

Values around 100% indicate a high reversibility of the charge-discharge process.

1.5.4. Nuclear Magnetic Resonance (NMR) Spectroscopy [63,64]

^{7}Li nuclear magnetic resonance spectroscopy is a versatile tool for the investigation on Li-ion dynamics. Since these processes are an important key for the understanding of the underlying processes inside the electrode during charging and discharging, the next few pages will give you a brief overview about the basic principles of this method. Basically, all nuclei possess a certain nuclear spin quantum number I which is a multiple of 1/2. All spin quantum numbers $I \neq 0$ have a nuclear spin which means that they are NMR active and possess a magnetic moment $\vec{\mu}$ which is given in equation 15.

$$\vec{\mu} = \gamma \sqrt{I\,(I+1)}\,\hbar \tag{15}$$

$$\vec{P} = \sqrt{I\,(I+1)}\,\hbar \tag{16}$$

$\vec{P}$ corresponds to the angular momentum of the nucleus. The nucleus-dependent constant γ is called the gyromagnetic (magnetogyric) ratio which describes the ratio between the magnetic (dipole) moment and the angular momentum of a nucleus.

Table 3 shows the gyromagnetic ratios of different nuclei in comparison to their sensitivity relative to ^{1}H. The relative sensitivity of a nucleus which is calculated based on the intrinsic sensitivity and the natural abundance is an estimation of its measurability. An improvement can be achieved by artificially increasing the percentage of the isotope inside the sample if the natural occurrence is too low.

Table 3. Spin quantum number, relative abundance, gyromagnetic ratio, quadrupole moment [64] (b=10^{-28} m^2 mb=milli b) and relative sensitivity of common nuclei. The calculation of the relative sensitivity is based on the intrinsic sensitivity and the natural abundance of the respective nucleus.

nucleus	I	abundance (%)	$\gamma_n/2\pi$ (MHz T^{-1})	Q (mb)	rel. sensitivity (%)
^{1}H	1/2	99.9885	42.578	-	100
^{2}H	1	0.015	6.536	+2.8	0.0631
^{12}C	0	98.93	-	-	not active
^{13}C	1/2	1.07	10.708	-	0.0176
^{14}N	1	99.636	3.077	+16	0.101
^{15}N	1/2	0.364	-4.316	-	$3.85*10^{-4}$
^{19}F	1/2	100	40.052	-	83.0
^{23}Na	3/2	100	11.262	+100	9.27
^{7}Li	3/2	92.41	16.5468	-40.1	27.0
^{6}Li	1	7.59	6.2662	-0.808	0.0631
^{8}Li [65]	2	0	6.3015	+31.1	-

When the nucleus is placed in an external magnetic field $\overrightarrow{B_0}$, the randomly oriented microscopic magnetic moments $\vec{\mu}$ start to align themselves in the static, external field, whereby $2I+1$ orientations are possible. Hence, for the most usual ^{1}H nucleus with $I = 1/2$ there are two possible spin states (+1/2; -1/2) which correspond to the representation of two spins, one parallel (α) the other antiparallel (β) to $\overrightarrow{B_0}$.

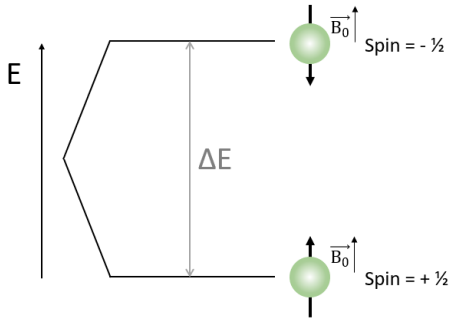

Figure 13. Image shows the representation of a spin-½ nucleus with two possible spin states ($2I+1$). $I = -1/2$ is the less occupied state β and antiparallel to the static magnetic field B_0 and $I = +1/2$ is the energetically favoured spin orientation α and parallel to B_0.

At equilibrium there is an excess of nuclei in the α state according to Boltzmann.

$$\frac{N_\alpha}{N_\beta} = \exp\left(\frac{\Delta E}{k_B T}\right) \tag{17}$$

$$\Delta E = h\upsilon = h\,\frac{\gamma \vec{B}_0}{2\pi} \tag{18}$$

The difference between the spin energy levels is very small which in turn leads to rather small population differences. Since the energy difference is direct proportional to the static magnetic field $\overrightarrow{B_0}$, the excess of nuclei with one specific orientation can be increased by increasing the field strength. However, assuming to have 1 million ^{1}H nuclei in an 18.8 T magnetic field only leads to an excess population of 64 nuclei in the preferred orientation corresponding to a population ratio of 0.999872. Although in reality there are much more nuclei present in a NMR sample, the population difference is still low leading to sensitivity problems. An improvement can be achieved by either increasing the field strength of $\overrightarrow{B_0}$ (depends on available NMR device) or by increasing the sample volume and therefore the absolute population difference.

The static magnetic field $\overrightarrow{B_0}$ imposes a torque on the magnetic moment $\vec{\mu}$ which starts to precess around the z-axis. The direction of precession is determined by the sign of γ.

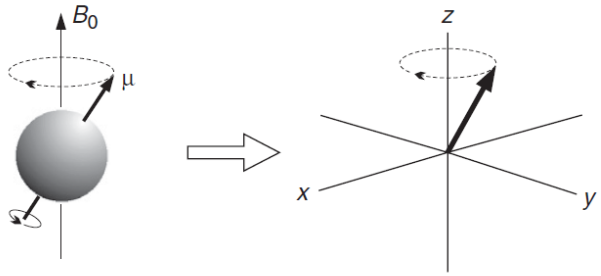

Figure 14. The magnetic moment $\vec{\mu}$ starts to precess around the z-axis if a static magnetic field $\overrightarrow{B_0}$ is applied in this direction. The rate of precession is called Larmor frequency and depends on the field strength and on the gyromagnetic ratio of the spin. (Source: Clardige [64])

The motion is referred to as Larmor precession. The rate of the precession is the Larmor frequency ν and is defined as follows:

$$\nu = \frac{-\gamma \vec{B}_0}{2\pi}\ [Hz] \qquad \omega = \upsilon * 2\pi\ [\frac{rad}{s}] \tag{19}$$

Nuclear magnetic relaxation takes place when the spin state of a nucleus changes due to the absorption of discrete energy amounts supplied to the system via a radio frequency pulse. The energy corresponds to the energy difference of the spin states described in equation 18 and thus also to the Larmor frequency ν.

Assuming a cartesian coordinate system with the static magnetic field $\overrightarrow{B_0}$ on the z-axis, one can say that during equilibrium there is a net magnetisation of the nuclei in z-direction $\overrightarrow{M_{eq}}$ arising from the population excess of the parallel α state. Applying a radio frequency pulse switches the net magnetisation into either the x-y plane (90° pulse) or in direction of the -z-axis (180° pulse). Regarding the ^{1}H nucleus, the 90° pulse equalises the population of the α and β states and no net z-magnetisation is measurable. During the 180° pulse the population of the spin states is inverted leading to more spins in the β orientation.

The magnetic component of the rf-pulse provides a time dependent magnetic field $\overrightarrow{B_1}$ which oscillates at the Larmor frequency ν as well and is perpendicular to the static field $\overrightarrow{B_0}$. Basically, one can say that it consists out of two counter-rotating magnetic vectors with the frequencies $+\nu_0$ and $-\nu_0$ which are shown in Figure 15. Viewing the processes occurring during and after the application of a rf-pulse from a stationary point of view (co-ordinate system is static) is called the laboratory frame of reference. For the sake of simplicity, the rotating frame of reference with the coordinates x′, y′, z′ is introduced. It includes the rotation of the co-ordinate system with a rate equal to the applied radio frequency ν. In this representation, the motion of the component rotating in the same direction as the co-ordinate system is frozen whereas the other one rotating in the opposite direction doesn't meet the resonance condition and can be ignored.

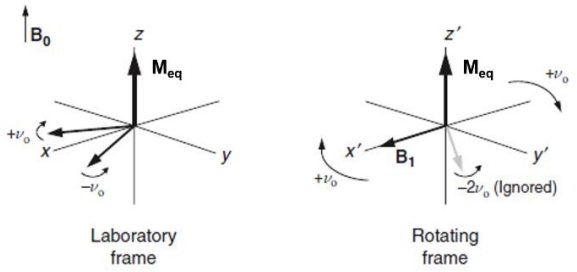

Figure 15. In the laboratory frame, B_1 precesses around the z-axis with the rotation speed ν_0 (Larmor frequency). It can be split into two counter-rotating vectors precessing with $-\nu_0$ and $+\nu_0$. The rotating frame of reference is a simplification of this representation where the co-ordinate system rotates with the Larmor frequency as well leading to a situation where the $+\nu_0$ vector can be regarded as static whereas the $-\nu_0$ vector is far from the resonance conditions and can be ignored. (Source: Claridge [64])

Applying a rf-pulse along the x-axis imposes a torque on $\overrightarrow{M_{eq}}$ and flips it from z-direction towards the y-axis where the signal is measured. This means that at equilibrium the magnetisation should be 0 whereas you should measure the highest signal after applying a 90° pulse which decreases afterwards with the time. This process is called relaxation and the RF signal one measures is called FID (Free Induction Decay).

Figure 16. Example of a Free Induction Decay (FID). After the application of a rf-pulse the FID shows the highest amplitude and fades until the system is completely relaxed towards thermal equilibrium (Source: Clardige [64])

1.5.4.1. Solid State NMR ^{7}Li NMR

Solid-state NMR spectroscopy is a powerful tool to investigate the dynamics and local structures of materials. Microscopic as well as macroscopic diffusion mechanisms can be observed. In comparison to liquid-state NMR, where Brownian motion leads to an averaging of orientation dependent (anisotropic) interactions and thus to narrow NMR lines, in solid-state NMR there is very little mobility and the anisotropic interactions cause substantial line broadening. Depending upon the extent of those anisotropic interactions, line widths up to 10^9 Hz can be reached whereas liquid-state NMR shows lines in the order of a few Hz [91].The orientation dependent interactions may come from external factors like Zeeman or radiofrequency terms, which are interactions with $\overrightarrow{B_0}$ and $\overrightarrow{B_1}$ or from internal factors such as internuclear dipolar or quadrupolar coupling, anisotropic J-coupling or chemical shift anisotropy which is described in equation 20.

$$H_{NMR} = H_{external} + H_{internal} = (H_Z + H_{RF}) + H_{CSA} + H_{DC} + H_{QC} + H_J \quad (20)$$

In liquids all these internal terms are reduced to their isotropic averages whereas they have a considerable impact on the line shape in solid-state NMR [92].

$$H_{CSA} \Rightarrow \sigma_{iso} \qquad H_{DC} \Rightarrow 0 \qquad H_{QC} \Rightarrow 0 \qquad H_J \Rightarrow J_{iso} \tag{21}$$

Dipolar coupling is an interaction between two magnetic dipoles which can provide structural information. For nuclei with a spin quantum number I > 1/2, quadrupolar interactions are observed triggered by a non-spherical charge-distribution in the nucleus [65]. The coupling of the quadrupole moment is with the electric field gradient is called quadrupole coupling [91]. J-coupling, an indirect dipole-dipole interaction mediated through chemical bonds, only leads to line widths in the order of a few hundred Hz and is thus comparatively small whereas it is important for liquid state NMR. The influences coming from chemical shift anisotropy as well as dipolar interactions are averaged to the corresponding isotropic value using Magic Angle Spinning which leads to smaller line widths. Here, the sample is fixed in a 54.7° angle in relation to the external magnetic field and rotates in the kHz range. An isotropic signal is reached if the rotation speed is higher than the line width would be without MAS [63].

Since all lithium isotopes have a spin quantum number larger than 1/2 [65], quadrupolar interactions with non-vanishing electric field gradients have to be taken into account. ^{7}Li has the largest quadrupole moment Q (see Table 3) of all lithium isotopes which broadens the ^{7}Li resonances by the quadrupolar interactions. The way the quadrupole influences the spectrum, may give information on the local structure around a nucleus. Due to the spin quantum number I = 3/2 ^{7}Li possesses four magnetic energy levels which lead to the formation of a central line ($+1/2 \leftrightarrow -1/2$) and two satellite lines ($\pm 3/2 \leftrightarrow \pm 1/2$) [66]. Hence, for structural investigations where a high resolution is of great importance the ^{6}Li nucleus is preferred due to its 50 times smaller quadrupole moment Q [67]. Nevertheless, most of the lithium NMR experiments are conducted with ^{7}Li although the second abundant stable isotope ^{6}Li would lead to much narrower NMR line shapes because the former is a more sensitive nucleus with a higher abundance and therefore no further enrichment is necessary, and the amount of sample required to get a sufficient signal is comparatively low [66]. In addition, ^{7}Li has shorter relaxation times which is also advantageous in a number of cases.

1.5.4.2. Lithium Ion Dynamics with NMR

Solid-state NMR is able to provide information about diffusion processes over a large dynamic range (sub Hz to MHz). Diffusion parameters like activation energies or jump rates can be determined unless no significant temperature dependent structural changes occur during the measurement [68].

I will focus more on the spin-lattice relaxation experiments since those are applied in this thesis. Spin-lattice relaxation rates (R_1) (which is the inverse of the spin-lattice relaxation time = T_1) are measured in the laboratory frame of reference and are therefore sensitive to jump rates in the MHz range whereas slower jumping processes in the kHz range can be detected with the so-called $R_{1\rho}$ experiment conducted in the rotating frame of reference. Even slower jumping processes in the order of 10^4 Hz can be probed by the use of R_2 (spin-spin relaxation) experiments.

R_1 experiments [68]

^{7}Li spin-lattice relaxation times T_1 are measured using the saturation recovery pulse sequence shown in Figure 17. As already described in the introduction, in equilibrium there is a net magnetization in z-direction in the presence of a static magnetic field.

$$\overrightarrow{M_z} = \overrightarrow{M_{eq}} \tag{22}$$

Several closely spaced 90° rf-pulses are then sent to destroy this initial longitudinal magnetization in order to get a z-magnetization $\overrightarrow{M_z} = 0$. The magnetization curves shown in Figure 17 are obtained by a series of measurements of the transients $\overrightarrow{M_z}(t_{var})$ in dependence on a variable relaxation time until equilibrium is reached. The recovery process can be described by a stretched exponential function given in equation 23 [69].

$$M_z(t_d) \propto 1 - \exp(-(t_{var}\, R_1)^{\gamma}) \tag{23}$$

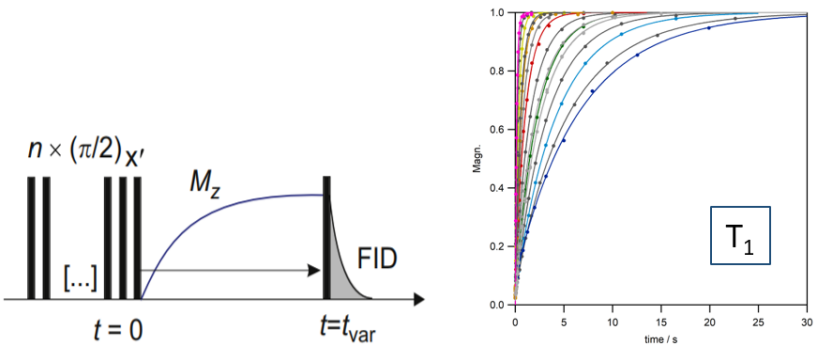

Figure 17. Saturation Recovery Pulse sequence (left) for the conduction of a spin-lattice relaxation experiment. The initial magnetization M_z is destroyed, a detection pulse is applied after a variable delay time t_{var}. The stretched exponential behaviour of the M_z magnetization in dependence on the delay t_{var} during relaxation is shown on the right for different temperatures. (Source: Kuhn et al. [68])

The relaxation rate R_1 is the reciprocal of the spin lattice relaxation time T_1 and is an indicator for the probability of the spin to switch between the distinct Zeeman levels. Only induced transitions between the Zeeman levels are able to cause a spin lattice relaxation. In order to get information on activation energies and jump rates the relaxation rate is measured at different temperatures over a large range. The curve reaches its maximum at the temperature where the correlation rate of the motional process equals the Larmor frequency.

$$\nu = \tau_c^{-1}\,[Hz] \tag{24}$$

Consequently, R_1 experiments can describe very fast motional processes or with regard to lithium diffusion in solid state, very fast jump rates, in the order of approximately 10^9 Hz. Sometimes it is not possible to detect a maximum because it is beyond the temperature limitations of the device or outside the thermal stability window of the sample. It is possible to shift the maximum to lower temperatures by decreasing the static magnetic field $\overrightarrow{B_0}$ and thus also the Larmor frequency. However, it is not feasible to change the frequencies in a large range. Performing NMR experiments at $\overrightarrow{B_0} < 1$ T would lead to very low signal-to-noise ratios. Therefore, other methods have to be used for the investigation of diffusion behaviours in different time scales.

$R_{1\rho}$ measurements [68]

Slower jumping processes in the order of 10^5 Hz can be detected at lower temperatures by the measurement of $T_{1\rho}$ relaxation times using the spin-locking technique conducted in the rotating frame of reference. First of all, a 90° rf-pulse flips the magnetization to the -y' axis which is kept there by a following "locking pulse" leading to a static magnetic field B_1 along the -y axis. After a certain time t_{lock} the locking pulse is switched off and the decay of $M_{-y'}$ is recorded as a function of t_{lock} [69] which can be seen in Figure 18. The shape of the magnetization curve results from equation 25.

$$M_{-y'}(t_{lock}) \propto \exp(-(t_{lock}\,R_{1\rho})^{\gamma_\rho}) \tag{25}$$

The much smaller B_1 field (mT) leads to smaller Zeeman splitting than during R_1 measurement in the laboratory frame and the measurement is therefore more sensitive to motional processes in the kHz range.

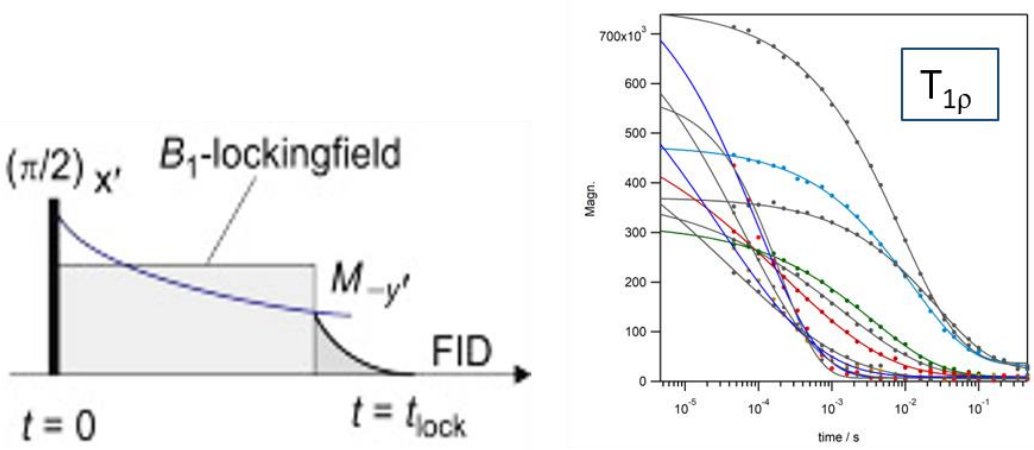

Figure 18. Pulse sequence of a $R_{1\rho}$ /$T_{1\rho}$ measurement: the magnetization is flipped to the -y' axis and locked there by a B_1-lockingfield. The decay of $M_{-y'}$ is recorded as a function of the locking pulse time t_{lock}, shown in the plot on the right side (for different temperatures) (Source: Kuhn et al. [68])

In most cases, plotting the spin-lattice relaxation rate $\log_{10}(R_{1\rho})$ as a function of the inverse temperature leads to a diffusion induced rate peak whereas in other cases only one flank of the peak is visible depending on the applied temperature range. The jump rates τ_c mostly follow Arrhenius behaviour (see eqn. 26) and therefore, the activation energies E_A of the hopping processes can be determined from the slopes of the high and the low temperature flank.

$$\tau^{-1} = \tau_0^{-1} \exp(\frac{-E_A}{k_B T}) \tag{26}$$

The preexponential factor τ_0^{-1} is in the order of phonon frequencies. From the maximum, if there is one, the frequency dependent jump rate regarding long range diffusion can be determined. Here the following condition is met, whereby the factor 0.5 is only an estimation.

$$\upsilon * \tau_c = 0.5 \tag{27}$$

The shape of the peak can further give information on the dimensionality of the diffusion processes occurring in the material. Usually a highly symmetric peak indicates uncorrelated jumping processes leading to isotropic random motion. This behaviour is mostly the case for 3D diffusion whereby an asymmetric peak may indicate 2D or 1D diffusion.

Uncorrelated 3D motion is described with the diffusion model of Bloembergen, Purcell and Pound (BPP) based on a single exponential correlation function:

$$g(t) = \exp(-\frac{|t|}{\tau_c}) \tag{28}$$

Deviations from this behaviour reflect correlated motion caused by vacancy diffusion mechanisms, coulombic interactions of the spins or structural disorder and are better described by the stretched exponential function:

$$g(t) = \exp(-(\frac{|t|}{\tau_c})^{\alpha}) \quad 0 < \alpha \leq 1 \tag{29}$$

However, equation 29 is applicable to nuclei with $I = 1/2$. In the presence of quadrupolar interactions the correlation function can deviate from eqn. 29.

Effects which are coming from correlation effects like coulombic interactions and/ or structural disorder are only visible on the low temperature flank, yielding to an activation energy reduced by the correction factor α. In contrast, motion originating from diffusion in confined dimensions (1D, 2D) decreases the slope of the high temperature flank. In addition, there might be a characteristic frequency dependence of the flank which only shows up for 1D or 2D diffusion [70].

Line shape measurements [70,71]

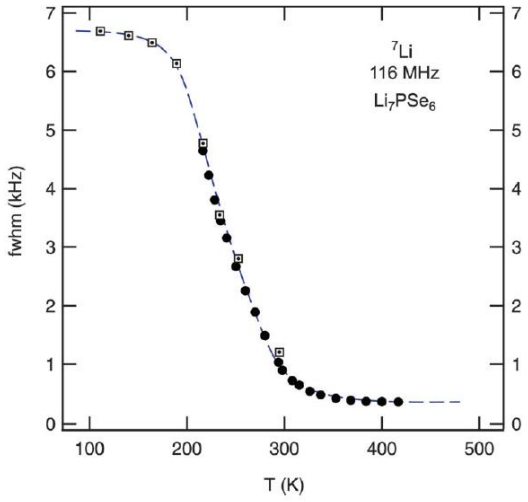

Figure 19. Temperature-dependent ^{7}Li NMR line width (full width at half maximum fwhm) of polycrystalline Li_7PSe_6. Figure shows the typical course of a motional narrowing curve indicating the rigid lattice at low temperatures. The dashed line is drawn to guide the eye. (Source: Dissertation Viktor Epp [70])

Also, NMR line shape measurements are able to give insights into the lithium dynamics in solids. In order to get the information, ^{7}Li line shapes (of central transition $+1/2 \leftrightarrow -1/2$) are measured with a single pulse procedure at different temperatures and the full width at half maximum of a line (fwhm) is plotted against the temperature. A typical plot is shown in Figure 19. The NMR line width is dependent on the spin-spin relaxation rate R_2. Due to the single pulse sequence, quadrupole intensities are mostly suppressed. The measurement has to be carried out over a large temperature range to see the whole dynamic range of the material starting from the rigid lattice, where no motion induced line narrowing is observable, up to completed motional narrowing at high temperatures.

In the so-called rigid lattice regime at low temperatures (~below 130 K in Figure 19), measured under non-rotating conditions, the correlation rate τ_c^{-1} is much smaller than the dipolar broadened line width which is constant in this temperature range. At a certain temperature the jump rates resemble the rigid lattice linewidth. Motion gets faster, and the dipolar interactions are averaged resulting in smaller line widths. In this motional narrowing regime, the correlation rate τ_c^{-1} is proportional to R_2. Jump rates can be estimated and range from 10^3-10^5 Hz. However, these values are only an estimation and of limited use. The line shape measurement is more interesting to get an idea of the dynamic range of the hopping processes inside a material. At very high temperatures (above 350 K in Figure 19) the line width is again temperature independent due to inhomogeneities of the static magnetic field $\overrightarrow{B_0}$.

1.6. Solid-State Diffusion

Diffusion in solids ($<10^{-7}$ cm^2 s^{-1}) is some orders of magnitude smaller than liquid state diffusion (10^{-4} cm^2 s^{-1}) [71]. The atoms and ions are less mobile than in solution and diffusion is only possible in presence of crystallographic defects which can be point defects (vacancies, interstitials), line defects (dislocations) or planar defects (grain boundaries, stacking faults). The number of defects is dependent on the temperature. There are three major possibilities for an atom/ion to move within a defective crystal lattice which are illustrated in Figure 20: Interstitial mechanism, Interstitialcy mechanism or vacancy mechanism [63].

- Interstitial mechanism: It is predominant for atoms smaller than those of the host lattice which are located at interstitial sites forming a solid solution with the host. No vacancies are needed for the atoms to move and therefore high diffusion coefficients can be detected in comparison to the other two mechanisms.

- Vacancy mechanism: It is the most important mechanism regarding metals and alloys. Guest and host atoms move to vacant sites. Thus, this mechanism is dependent on the number and mobility of vacancies. Furthermore, with regard to substitutional solutes repulsive and attractive interactions with the vacancy may be the reason for correlations [70].

- Interstitialcy mechanism: It is considered for interstitial atoms with a similar size as the host atoms for which direct interstitial diffusion would be unfavourable.

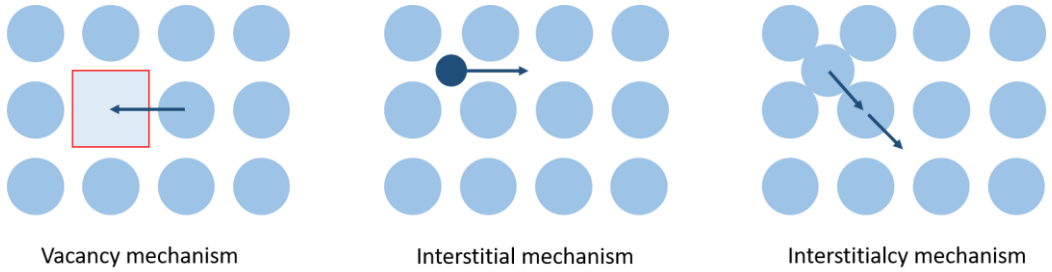

Figure 20. Three possibilities of microscopic diffusion in a defective crystal system

The crystal lattice can be regarded as potential landscape with different minima representing preferred locations (interstitial sites, vacancies…) for the diffusing species to stay. Considering a situation where the probability of a particle to jump is identical for each direction, the jump process is defined as uncorrelated and the landscape can be simplified as follows:

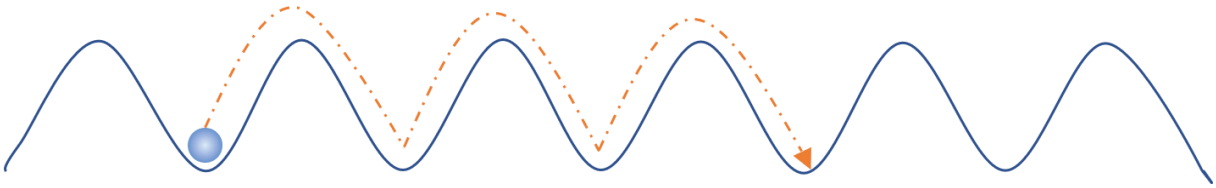

Figure 21. One-dimensional potential landscape of a crystalline solid where all possible locations for a diffusing species to stay (vacancies, interstitials…) are energetically identical. The motion is referred to as uncorrelated.

This model is termed "random walk". Here, the mean displacement of the particle after n jumps corresponds to the sum of all individual jumps [63] (see Figure 22).

$$\vec{R}_n = \sum_{1}^{n} \vec{r}_i \tag{30}$$

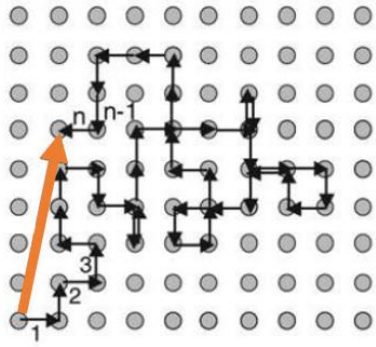

Figure 22. Representation of a "random walk". The mean displacement R_n is drawn with the orange arrow. (Source: Diffusion in Solids, H. Mehrer [72])

For an ideal random walker, the potential landscape is independent on the time meaning that also the diffusivity is independent on the regarding time frame. Thus, the diffusion coefficient can be calculated regarding one individual jump using the Einstein-Smoluchowski equation [71].

$$D^{uc} = \frac{a^2}{2d\tau} \tag{31}$$

Here a corresponds to the jump length, d is the dimensionality (1D, 2D or 3D) of the process and τ is defined as the residence time of the respective species. In the case of uncorrelated jumps where the mean jump time is short in comparison to the mean residence time the tracer diffusion coefficient D^T can be determined as follows [71].

$$D^T = \lim_{t \to 0} \frac{\langle \vec{R}^2(t) \rangle}{2dt} \tag{32}$$

D^T is calculated from the mean square displacement after a given time t and should equal D^{uc} for uncorrelated motion.

The jump may also be referred to as correlated. In this case the potential landscape is time dependent and D^{uc} differs from D^T by the correlation factor f. As you can see in Figure 23, the various lattice sites are energetically different.

$$D^T = f \cdot D^{uc} \qquad 0 < f \leq 1 \qquad \text{f = 1 for uncorrelated jumps} \tag{33}$$

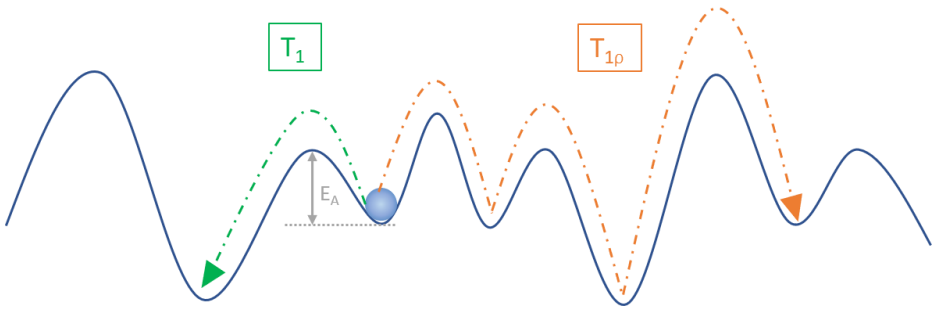

Figure 23. Representation of a one-dimensional potential landscape with energetically different minima. The figure shows short range diffusion (green) which can be detected using spin-lattice relaxation (T_1) experiments in the laboratory frame of reference and longer range diffusion (orange) which is measurable with spin-lattice relaxation ($T_{1\rho}$) experiments conducted in the rotating frame of reference.

With increasing temperature, the particles get faster and thus also have more energy to overcome the energy barriers leading to an increased number of successful jumps. The temperature dependence of the diffusivity is described empirically by an Arrhenius relation with E_A corresponding to the activation energy of the mass transport.

$$D^T = D_0^T \, exp(-\frac{E_A}{k_B T}) \tag{34}$$

The well-known Fick's law describes the diffusion in a continuous medium under a chemical potential gradient and is therefore not applicable for the examples mentioned above.

$$J_{x,y,z} = -\mathrm{D}\nabla\mathrm{c} \tag{35}$$

From a microscopic point of view there is no gradient responsible for the motion of the particles. The diffusion is rather random and triggered by the mentioned crystallographic defects and the thermal energy of the particles and is therefore known as self-diffusion [70]. This behaviour was shown by Albert Einstein and Marian von Smoluchowski (see eqn. 31).

There are several techniques to study diffusion processes occurring in solid state but not all results are comparable. The determined diffusion coefficients may differ in several orders of magnitude although the regarded material remains unchanged and the data is acquired correctly. The results strongly depend on the conditions of determination.

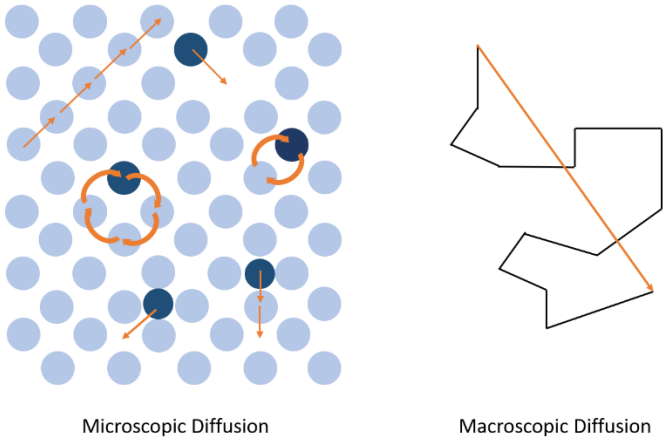

Figure 24. Solid state diffusion: Microscopic diffusion on the atomic level and macroscopic diffusion as a result of lots of microscopic steps

First of all, one has to decide whether one wants to look at diffusion from a microscopic or a macroscopic point of view (see Figure 24). Examples for macroscopic methods are field gradient NMR [72] or the tracer method [70,72,73]. The techniques are related to Fick's law of diffusion and referred to as direct methods because the diffusion coefficient can be directly determined.

Microscopic methods are mostly indirect. The diffusion coefficient is derived via microscopic models from parameters that are influenced by diffusional processes [70] like the residence time τ. As seen in section 1.5.4.2. the residence time τ of a species at a certain position and thus also the jump rate τ^{-1} is able to be determined via SLR NMR. The values can then be further used for a calculation of the microscopic self-diffusion coefficient via the Einstein-Smoluchowski equation (eqn. 31).

The microscopic diffusion coefficient can be determined using[71]:

- NMR spin-lattice relaxation: R_1, $R_{1\rho}$
- Line shape measurements/ spin-spin relaxation: R_2
- Spin alignment echo (SAE) [74]
- β-radiation detected NMR [68,71]
- Quasielastic neutron scattering [73]
- Impedance spectroscopy [70]

In order to get a detailed impression about the diffusion mechanisms inside a material a comparison of microscopic as well as macroscopic diffusion parameters is necessary.

2. Experimental

Chemicals

Ammonium sulfate p.a., MERCK 1.01217.1000

Sodium citrate dehydrated p.a., MERCK 1.06448.1000

Copper(II) sulfate pentahydrate ReagentPlus™, ~99%, SIGMA

Zinc sulfate heptahydrate p.a., MERCK Art.8883

Millipore

Nitric acid 69.0-70.0%, J.T. Baker

Ethylene glycol ≥99.7%, AnalaR NORMAPUR®, VWR Chemicals

Ammonium fluoride ≥98.0% AnalaR NORMAPUR®, VWR Chemicals

Ortho-phosphoric acid ≥85.0% p.a., FLUKA

Selectilyte LP 30, BASF

Materials

Ti-foil, 0.25 mm thick, 99.7% trace metals basis, Aldrich

Cu-foil, 25 µm thick, PI-KEM LTD

Cu-foil, 20 µm thick, Schlenk

Whatman™ GF/B

Freudenbergflies FS2190

Pouch foil

Part I

2.1. Synthesis of Porous Cu-Zn Alloys

First of all, the copper substrates were prepared. Four different samples, a rough Cu foil, a shiny Cu foil, an etched Cu foil and a titanium foil acted as substrate for the porous alloys. Table 4 is a list of the materials used as substrate.

Table 4. List of materials used as substrate for the electrodeposited, porous Cu-Zn layers

rough	Cu-foil, 20 µm thick, Schlenk	-
shiny	Cu-foil, 25 µm thick, PI-KEM LTD	-
etched	Cu-foil, 25 µm thick, PI-KEM LTD	120 s in 20 wt% HNO_3
Ti	Ti-foil, 250 µm thick, 99.7% pure	

All substrates are cleaned with distilled water and acetone to remove residual contaminations before being mounted in the electrodeposition cell. The electrodeposition bath reported by Varzi et al. [1] for porous Cu-Zn layers with the composition $Cu_{18}Zn_{82}$ was prepared. The aqueous solution consisted of 1 M $(NH_4)_2SO_4$, 0.3 M Na citrate, 0.028 M $CuSO_4$ and 0.222 M $ZnSO_4$ (first dissolution of the ammonium sulfate and the sodium citrate in de-ionized water followed by a dissolution of the Cu- and Zn-salt in the as-prepared solution). The solution was always prepared freshly before the deposition experiment.

The electrodeposition was performed in a transparent, plastic, electrochemical cell with a three-electrode assembly using the copper substrate as working electrode, a saturated calomel electrode as reference and a Pt mesh as counter electrode. To provide sufficient electrical contact, the sample was fixed in the cell by pressing it against a brass ring. An area of 1.65 cm^2 ($\varnothing = 1.45$ cm) of the titanium substrate was exposed to the electrolyte. The deposition was carried out at room temperature using the Metrohm Autolab Galvanostat/Potentiostat, the Autolab 10 A current booster BSTR16A and the Nova 1.11 software. After the deposition, the samples were rinsed with de-ionized water and carefully dried with compressed air. For the deposition of the Cu-Zn alloy a current density of -3 A cm^{-2} was applied for 27 s (80 C cm^{-2}). After Cu-Zn deposition the samples were washed with deionized water (Millipore) and pre-dried with compressed air. After most of the residual water was removed from the porous structure by drying the samples at 60 °C, the mass of the electrodeposited layer was determined. The active material loading was between 5.5 and 8 mg cm^{-2}.

2.2. Morphological and Structural Characterization

In order to obtain some information on the morphology of the Cu-Zn alloy, Scanning Electron Microscopy (Vega Tescan with tungsten heated filament) was employed. Secondary electron images as well as Backscattered electron images were taken. However, the difference in atomic number is too low with regard to Ti, Cu and Zn to see a significant variation in contrast in BS mode. The attempt to take cross-section images via scratching the sample before placing it into the vacuum chamber was unsuccessful.

Energy dispersive X-ray analysis was made to get a rough impression of the elemental composition of the samples.

2.3. Structural Characterization with XRD

Prior to the measurement the Cu-Zn alloy was scraped off the substrate using a spatula. The powder was then characterized by XRD to minimize the signal coming from the Cu-substrate. XRD patterns were recorded on a Bruker D8 Advance diffractometer with Bragg Brentano geometry to get some information on the average composition of the Cu-Zn alloy as well as to receive information on the crystal structure including cell constants. All diffractograms were collected at room temperature and under atmospheric pressure. Rietveld refinement was done with the X'Pert HighScore Plus software.

2.4. Electrochemical Characterization

For the electrochemical characterization of the Cu-Zn alloys Swagelok-type lithium half cells were built. Therefore, a circle with a diameter of 10 mm was punched out of the dried, deposited Cu-Zn alloy, to act as working electrode (positive electrode) in the cell. Afterwards, the electrode was dried overnight in the Büchi at 60 °C under vacuum to get rid of residual water and air. The assembly of the cell was done under inert gas (argon) conditions in the glove box. The counter electrode (negative electrode) as well as the reference electrode consisted out of lithium. Two disks of the Whatman™ GF/B microfibre filters in the size of the electrode acted as separator and approximately 800 µL of LP 30 (1 M $LiPF_6$ in EC:DMC 1:1 w/w) were used as electrolyte.

Cyclic voltammetry and galvanostatic cycling experiments were carried out using the MPG-2 multi-channel potentiostat/galvanostat from Bio-logic. The CV was recorded in a potential range between 0.005 V vs. Li/Li^+ and 2.5 V vs. Li/Li^+ starting at the OCV of the respective cell. Slow potential scan rates of 0.05, 0.1, 0.2, 0.5 and

1.0 mV s^{-1} were chosen whereby two scans were recorded for each scan rate. The galvanostatic charge/discharge cycling was carried out in accordance to the rate capability test of Varzi et al. [1] with the exception that 10 cycles were recorded for each current load instead of 5. Constant current loads of 0.1, 0.5, 1, 2, 5 and 10 A g^{-1} were applied to the cell for 10 cycles each. Finally, the current load was decreased back to the initial value to see if the initial capacity is retained.

In general, after preparation all cells were left in rest state for at least 12 hours before starting each electrochemical measurement to enable the system to equilibrate. All measurements were carried out at room temperature.

2.5. Investigation on Li^+ Dynamics Using NMR Spectroscopy

Sample preparation:

In order to lithiate the Cu-Zn electrodes (prepared as in section 2.1) the samples were cycled three times with a current load of ±30 mA g^{-1}. Afterwards an additional discharging step with -30 mA g^{-1} was applied. For the fully lithiated sample the discharging was stopped at the lower potential limit 0.005 V vs. Li/Li^+. For the achievement of certain lithiation degrees, here 2/3 and 1/3 of the initial capacity, the discharging was stopped as soon as 66.6% or 33.3% of the capacity (based on the discharge capacity of cycle 2) were reached.

Afterwards the cells were transferred to the glove box (argon) and rested for at least 24 h before opening. The Cu-Zn working electrodes were cleaned by rinsing them with DMC and subsequent soaking in water for appr. 15 minutes to get rid of the $LiPF_6$ conducting salt. The cleaning procedure was repeated once. The washed electrodes rested in the glovebox (MBraun MB150B-G) until the whole solvent was evaporated. Then the lithiated Cu-Zn alloy was scraped off the Cu-foil using a spatula. The powder was placed in a 5 mm (= outer diameter, inner diameter 3.5 mm) NMR tube which was fire-sealed to keep the sample away from moisture and air.

Measurement conditions

All ^7Li NMR data were acquired on the Bruker Avance III (300 MHz) spectrometer connected to a shimmed cryomagnet with a nominal magnetic field of 7.04 T (resonance frequency of 116 MHz) with the Ceramics 500WB H7039 probe head and a type E thermocouple. The measurements were carried out in a temperature range from -60 °C to 200 °C. For temperatures higher than 80 °C the type T thermocouple was used for temperature regulation.

For the motional narrowing curve, the line width was determined from ^{7}Li NMR spectra obtained after a Fourier transformation of the FID (free induction decay) which was recorded by a single pulse experiment. A delay of at least $5 \cdot T_1$ was used between each scan to enable the spin to fully relax. With the exception of the lower temperatures, where the shim coil could not resist the cold for the duration of the measurement, 128 scans were made to obtain a sufficient signal.

The spin-lattice relaxation rates R_1 in the laboratory frame of reference were determined with a saturation recovery pulse sequence [75] (see section 1.5.4.2). For the detection of slower diffusion processes the spin-lattice relaxation rate in the rotating frame of reference $R_{1\rho}$ was recorded with the spin-locking technique using a locking frequency of 28 kHz. Both, $R_{1\rho}$ and R_1, were determined from the magnetization curve, which is the time dependent representation of the magnetization $M_z(t_d)$ and $M_\rho(t_{lock})$ [69]. The stretched exponential magnetization curve is expressed as [69]:

$$M_z(t_d) \propto 1 - \exp(-(t_d\, R_1)^{\gamma}) \;\&$$

$$M_\rho(t_{lock}) \propto \exp(-\left(t_{lock}\, R_{1\rho}\right)^{\gamma_\rho})$$

The logarithm of the obtained relaxation rates was then plotted against the inverse temperature.

2.6. Differential Scanning Calorimetry

To see whether any phase transformations or other reversible or irreversible processes take place in the Cu-Zn alloy caused by the temperature changes during the NMR measurements, a Differential Scanning Calorimetry (DSC) measurement was conducted ranging from 30.0 °C to 400.0 °C with a heating and cooling rate of 20.0 °C/min. The sample was heated up to 400.0 °C, then cooled to 30.0 °C and heated again. The data was acquired on the DSC 8500 of Perkin Elmer. The amount of sample was 7.526 mg.

2.7. BET- Surface Analysis

BET surface area and pore size were determined by measuring nitrogen adsorption isotherms at 77 K in a N_2-bath and calculated using Micromeritics software (3flex version 4.02).

Part II

2.8. Preparation of TiO_2 Nanotubes

Titanium foils were cut into squares having a side length of approximately 12.5 mm. To get rid of impurities, the pieces were then ultrasonically cleaned in three steps starting with acetone and proceeding with isopropanol and methanol. Each step was carried out for 15 minutes in the ultrasonic bath (Branson 1510), followed by rinsing with Millipore and subsequent drying on PP wipers.

The anodization was performed in a transparent plastic cell with a two-electrode assembly using the cleaned titanium substrate as working electrode and a stainless-steel electrode as counter electrode. To provide sufficient electrical contact, the sample was fixed in the cell by pressing it against a brass ring. An area of 0.708 cm^2 of the titanium substrate was exposed to the anodization bath. The electrolyte consisted of 97.6 wt% ethylene glycol, 2 wt% distilled water (Millipore) and 0.4 wt% NH_4F and was prepared in amounts of 200 g. For the anodization, the two electrodes were connected to a precision DC power supply (Agilent E3612A). A constant voltage of 60 V was applied (the real voltage varied from sample to sample between 59.9 V and 60.1 V) for 1 h. The next step was to rinse the as-anodized samples with deionized water and to dry them with compressed air. In order to achieve a highly regular tube-morphology a second anodization step was applied. Therefore, the first tube layer was removed with an adhesive scotch tape and on the same substrate TiO_2 nanotubes were grown under the same conditions for 5 minutes.

In the next step, after rinsing the samples with deionized water and subsequent drying with compressed air, an oxide sealing layer was formed underneath the nanotubes. Therefore, the samples were again anodized in a solution of 0.2 M H_3PO_4 in ethylene glycol for 10 minutes at 20 V. After this last anodization step the samples were rinsed again with deionized water and dried with compressed air.

2.9. Conductivity Measurement

Crystalline titania nanotubes are known to have a better conductivity than the amorphous (pristine) ones that one gets from anodization. Therefore, the TNT samples were annealed in an oven (Schröder Industrieofen with Logotherm® Program Controller S19) at 400 °C for 20h. The oven was heated with a rate of 5 °C/minute. The increased temperature should lead to a phase transformation to crystalline anatase. To examine the crystal structure, XRD measurements were performed using the Bruker D8 Advance diffractometer (see part 2.3)

For the measurement of the conductivity and thus also the resistance, gold and aluminium contacts were evaporated on top of the pristine as well as on the crystalline titania nanotubes using an aluminium mask with contact diameters of 0.8 mm. E-beam evaporation was carried out under vacuum ($p = 1 \cdot 10^{5}$ mbar) using the Inficon SQM 160 system (in N_2 filled glovebox). In addition, nickel contacts were sputtered on a pristine and an annealed sample using the same mask as for evaporation with the LEICA EM SCD050 sputtering device in combination with the LEICA EM QSG100.

Table 5. Layer thicknesses of gold, aluminium (e-beam evaporated) and nickel (sputtered) contacts. The aluminium and nickel layers were applied in a two-stage process (see values in brackets).

	Au	Al	Ni
TNT pristine	100 nm	245 nm (117+128)	300 nm (183+117)
TNT annealed	100 nm	245 nm (117+128)	300 nm (183+117)

Potentio Electrochemical Impedance Measurement (PEIS) as well as Staircase PEIS were used to measure the impedance of the annealed and the pristine sample using the VMP3 multi-channel potentiostat. Contacting was done with the help of a microscope as shown in Figure 25 using two 1 µm tungsten tips (T20-10-B Everbeing Int'l Corp.) which were connected to the impedance analyser.

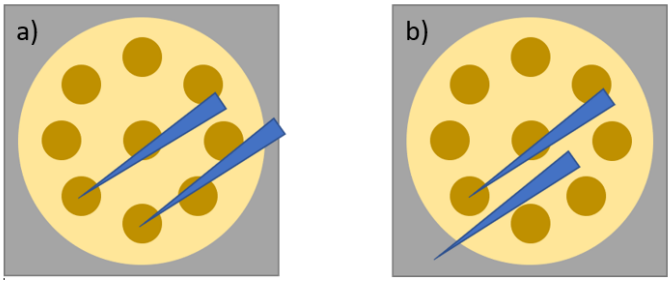

Figure 25. Simplified representation of two possibilities for contacting the tungsten tips with the titania nanotube sample. a) two gold, nickel or aluminium contacts are used b) one electrode is connected to a gold, nickel or aluminium contact and the other electrode to the titanium substrate

Only the Al-contacts on the annealed sample have shown some signals while for the Au- and Ni- contacts only noise was measurable. Therefore, the contacts were examined under the SEM to see if the contacts themselves were the problem for the bad signal. For the next attempt, the titanium substrates were polished prior to the anodization according to Table 6 to minimize the number of surfacial defects.

Table 6. Grinding and polishing steps for titanium

	pad	abrasive	time	rpm
Plane Grinding	SiC #320	SiC #320	until flat	300 rpm
Fine Grinding	MD-Largo	diamond, 9 µm	20-40 min. (until most scratches are gone)	150 rpm
Polishing step 1	MD-Mol	diamond, 3 µm	15-30 min. (to remove smaller scratches)	150 rpm
Polishing step 2	MD-Chem	SiO_2, 0.04 µm	until glass-smooth and reflecting	150 rpm

To further decrease the size of the contacts on the sample, Au-contacts were sputtered on top of the nanotubes (prepared after polishing step) with a thickness of 100 nm and 400 nm. This time a nickel mask which is able to provide contacts with diameters of 15, 30, 50, 100, 200 and 400 µm was used. After sputtering the contacts, one of the samples with 100 nm thick contacts was annealed in the oven at 400 °C for 20h. The microcontact set-up shown in Figure 25b was used for the DC-approach. The samples were contacted in the glove box (argon) and a variable potential was applied (CV) with the Keithley 2450 Source Meter® while the current response was measured. We were only able to receive useful values for the annealed sample.

As already mentioned in chapter 1.4.5 TNT are also active in terms of lithium insertion and extraction. Therefore, CV and GCPL experiments were made to see whether a possible difference in electrochemical performance between the pristine and the annealed sample is visible. The TNT samples were characterized in three-electrode, pouch-type cells with lithium as counter and reference electrode. Two layers of the Freudenbergflies FS2190 were used as a separator and LP 30 (1 M $LiPF_6$ in EC:DMC v/v 1:1) was used as electrolyte. A sketch of the exact assembly of such a pouch-cell is shown in Figure 26. All pouch-cells were assembled in the glove box (MBraun MB150B-G, filled with argon). The Cyclic voltammograms were recorded with a similar setting as shown in chapter 2.4. With regard to the GCPL measurement the samples were cycled with an approximate C-rate of C/1.5 for more than 30 cycles. The potential range was again 0.005 V – 2.5 V. All experiments were performed at room temperature.

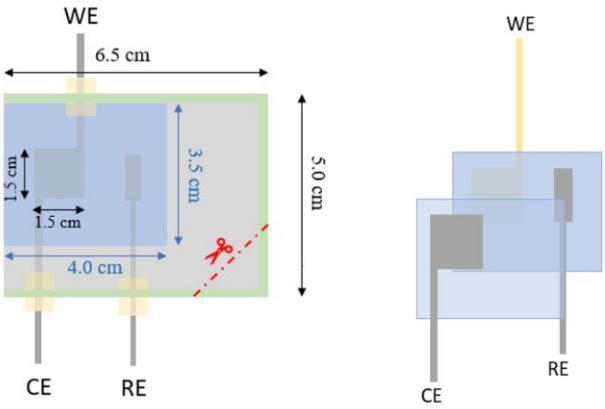

Figure 26. Assembly sketch of a pouch-cell used for titania nanotube working electrodes with lithium as counter- and reference electrode. Compartments: electrodes with Cu-current collector (dark grey), sealing tape (yellow), separator (blue), pouch foil (light grey) and weld-seam (green)

2.10. Effect of TNT as Substrate for Cu-Zn alloys in Li-ion Batteries

In order to examine the extent to which the use of TNT influences the electrochemical properties of the CuZn alloy several CV and GCPL experiments were made. For the deposition of the Cu-Zn alloy on the TNT, the pulsed current approach as described in chapter 1.4.5.2 was used. The electrodeposition bath was prepared as in chapter 2.1. and the annealed or pristine TNT sample was mounted in the respective transparent cell were an area of 0.708 cm^2 was exposed to the electrolyte. All other cell components remained unchanged in comparison to chapter 2.1. The pulsed current approach consisted out of 40 pulses whereby one pulse of -3 A cm^{-2} (corresponding to -2.124 A) was applied for 0.5 s followed by a delay time of 10 s. The real current was deviating from the pre-set -2.124 A due to a voltage overload during the measurement.

Cyclic Voltammograms were recorded with a similar setting as used in chapter 2.4. and Galvanostatic Cycling (GCPL) was carried out within a potential range comprised between 0.005 V and 2.5 V vs. Li/Li^+ and with C-rates between C/1 – C/2.3. The following electrode compositions were used as positive electrode in pouch-type, lithium half-cells (assembly described in more detail in the previous chapter):

- Cu-Zn alloy on Ti-substrate
- TNT on Ti-substrate
- Cu-Zn alloy on TNT on Ti-substrate

The experiments were carried out with annealed as well as with pristine nanotubes. All experiments were performed at room temperature.

3. Results & Discussion

Part I – Lithium Ion Mobility in Cu-Zn Alloys

3.1. Morphology and Composition

Cu-Zn alloys were electrodeposited onto different substrates in aqueous environment by applying high cathodic current densities which are exceeding the diffusion-limited current values by far. Although a constant current of -3 A cm^{-2} could not be delivered due to problems with voltage overload, the electrodeposition of the porous Cu-Zn alloys according to Varzi [1] et al. was successful. Independent on the substrate (Ti, rough, etched or shiny Cu-foil), all samples have shown the expected porous structure. When taking a closer look at Figure 27, it is clear that the material is microporous as well as nanostructured. The denser structure that surrounds the pores is composed of a fine dendritic network leading to a further increase in effective surface area.

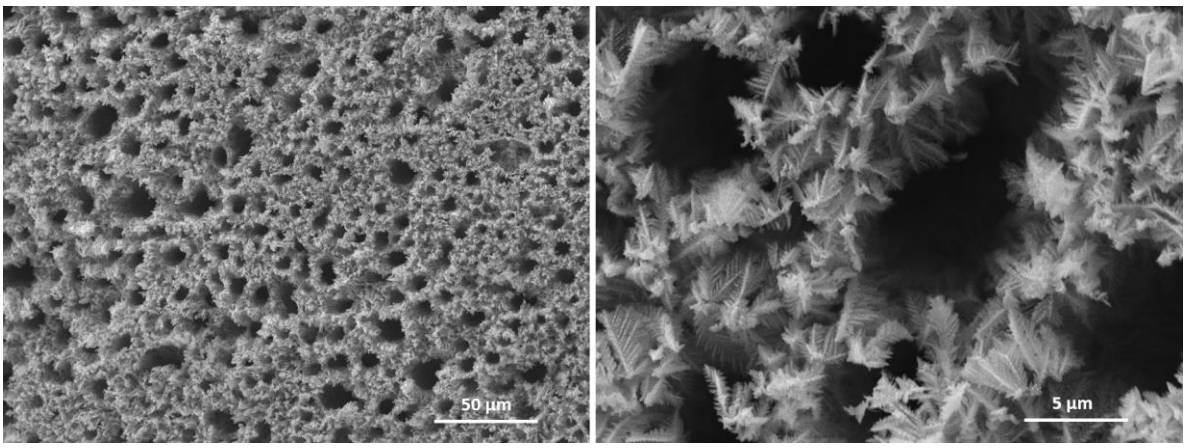

Figure 27. Secondary electron SEM images in different magnifications of porous Cu_2Zn_8 alloys prepared by electrodeposition on a Cu-foil in aqueous environment. The pores and dendrites are visible.

In order to get an impression of the size of the surface area, a Brunauer-Emmett-Teller (BET) specific surface measurement was performed. The method is based on the physical adsorption of gas molecules, here N_2, on a solid surface. The measured amount of adsorbed or released gas is proportional to the surface. Here, a specific surface area of 240 m^2/g was determined.

Figure 28 shows a difference in the structure with increasing distance from the substrate. The Cu-Zn alloy that was deposited at first directly on the substrate shows dendrites which are more defined and look much more fragile. The overall structure consists of lots of small macroscopic pores with a size of 5-10 µm. With increasing distance from the substrate, the macro pores are getting less numerous, but larger with a size of up to tens of micrometres on the top and the dendrites get coarser and less defined. This shows that the dendritic growth might be a function of the deposition time and is therefore more distinct in the first nanometres. Another possibility would be surface reactions like oxidation or corrosion changing the morphology of the dendrites on the top.

The dependence of the pore size on the distance from the substrate originates from a coalescence of the hydrogen bubbles evolving at the electrode-alloy interface which is described in more detail by Plowman et al. [76]. The hydrogen evolution is favoured by the high cathodic overpotential and the bubbles are disrupting the alloy growth mechanism leading to the porous structure.

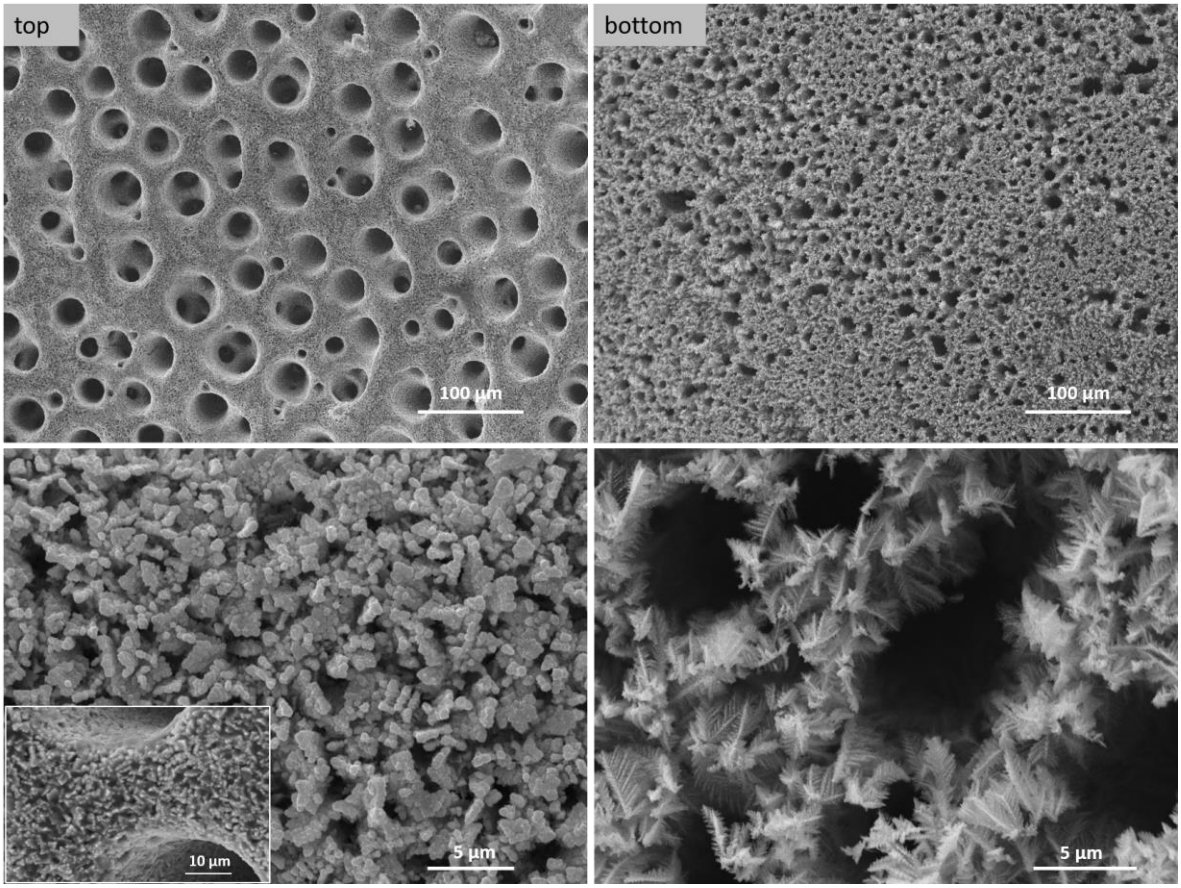

Figure 28. SEM images of Cu_2Zn_8 prepared by electrodeposition on Cu-foil. The part of the sample that was attached to the Cu-foil (first grown alloy) is shown on the right side whereas the upper surface is shown on the left. The pores are increasing from the bottom to the top.

Previous experiments have shown that a composition of approximately 20% Cu and 80% Zn reveals the best performances concerning the use as alternative anode material in LIB [1]. Therefore, the composition of the Cu-Zn alloy was determined with EDX and XRD. EDX analysis has given an average composition of 75% Zn and 25% Cu including a statistical error of ±10%.

The lattice constants and the structure type were determined with XRD analysis. The Cu-Zn alloy has a hexagonal closed packed structure similar to that of pure zinc with the lattice parameters $a = 2.7432$ Å and $c = 4.2956$ Å. When comparing the lattice parameters from our sample with lattice parameters from other Cu-Zn phases with hexagonal structure, listed in the Inorganic Crystal Structure Database (ICSD), it was visible that a and c were very similar to the Cu_2Zn_8 phase (Coll. Code 103157) with $a = 2.7418$ Å and $c = 4.293$ Å. Therefore we assumed a composition of 20% Cu and 80% Zn.

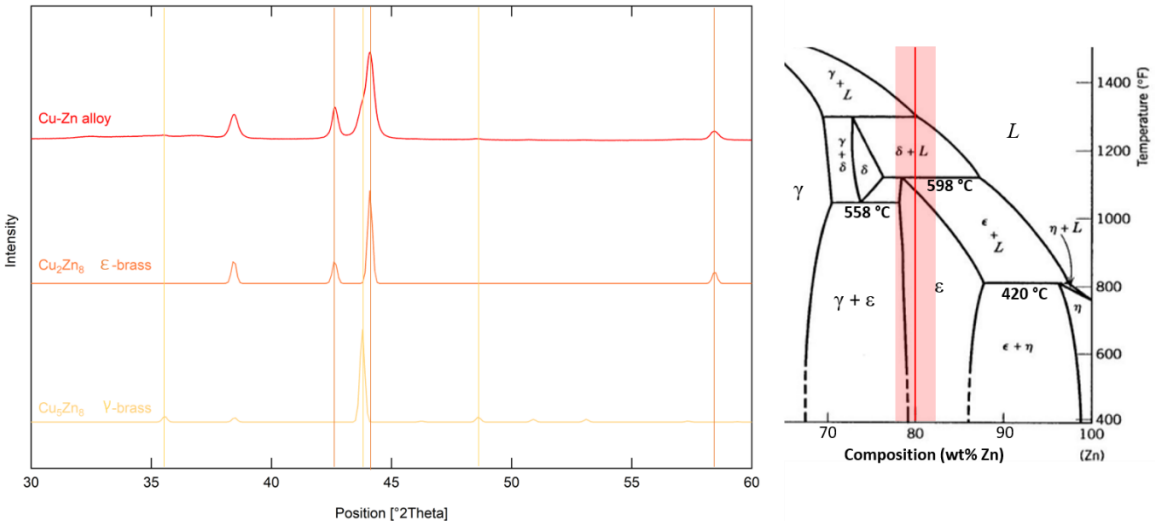

Figure 29. XRD pattern of the electrodeposited Cu-Zn alloy with an approximate composition of 20% Cu and 80% Zn. XRD data for comparison is taken out of the Inorganic Crystal Structure Database (Coll. Code 103157 & 2092). The area marked in red in the Cu-Zn phase diagram represents possible compositions of the alloy.

According to literature [77], the Cu_2Zn_8 phase should equal the Hume-Rothery ε-phase occurring for valence electron concentrations of ~1.8. The refined XRD pattern shows the existence of the hcp ε-phase to a major part but also the presence of small domains containing the cubic γ-phase [78]. Having a look at the phase diagram in Figure 29, would thus lead to the assumption that the overall Zn content is below 80 wt%. In this area between approximately 67 wt% and 78 wt% a heterogeneous mixture of the two adjacent phases is present.

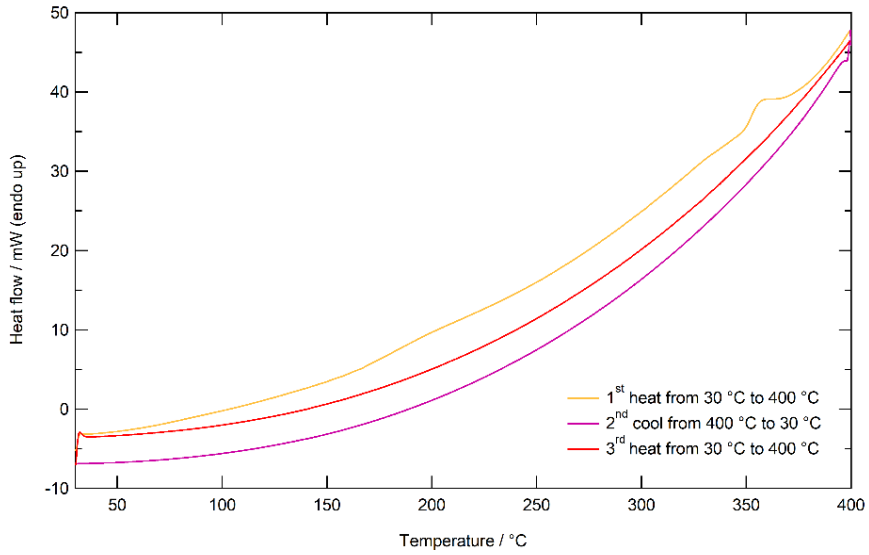

Figure 30. Differential Scanning Calorimetry (DSC) of electrodeposited Cu_2Zn_8 scraped off the Cu-substrate. 1.5 cycles between 30 °C and 400 °C were recorded (heating, cooling, heating)

A Differential Scanning Calorimetry (DSC) measurement was made to see if any phase transformations occur during heating up to 400 °C whereby a crystallization would be visible as exothermic peak. The corresponding diagram is shown in Figure 30. In accordance with the phase diagram shown in Figure 29, where a change in phase commences at the earliest at 558 °C (depending on the exact composition) no significant signals are visible in the DSC plot between 30 °C and 400 °C. Only a small endothermic peak with $\Delta H = 9.48$ J/g is visible at an onset temperature of 349.9 °C. The signal of unknown origin is related to an irreversible reaction because no exothermic counter-reaction takes place during cooling and also during the second heating the peak does not appear anymore.

3.2. Influence of the Substrate on the Cycling Behaviour

Lithium half-cells with a positive electrode consisting out of the Cu-Zn alloy deposited on different substrates (Ti-foil, rough Cu-foil, shiny Cu-foil and a Cu-foil roughened by etching with nitric acid) were electrochemically characterized, to see which substrate works best. The electrodeposition was successful for all half-cells independent on the substrate, although small particles are crumbling off. Figure 31 shows the cyclic voltammograms (CV) of the as-described Cu-Zn alloy recorded with a scan rate of 0.05 mV s^{-1} in the potential range of 0.005 to 2.5 V vs. Li/Li^+. The CV shows responses owing to the electrochemical activity of the alloy which will be discussed later and which is similar to the cyclic voltammetry response reported by Varzi et al. [1].

The different CVs given in Figure 31 show a very similar behaviour which leads to the assumption that the same electrochemical processes occur during the application of a cyclic potential sweep. The shiny Cu-foil as well as the Ti-substrate have shown some noise, demonstrated in Figure 31, which may be originated from contact losses caused by the smooth surface. The rough Cu-foil was demonstrated the best because no noise was noticeable, and no further treatment of the foil is necessary which maintains the reproducibility.

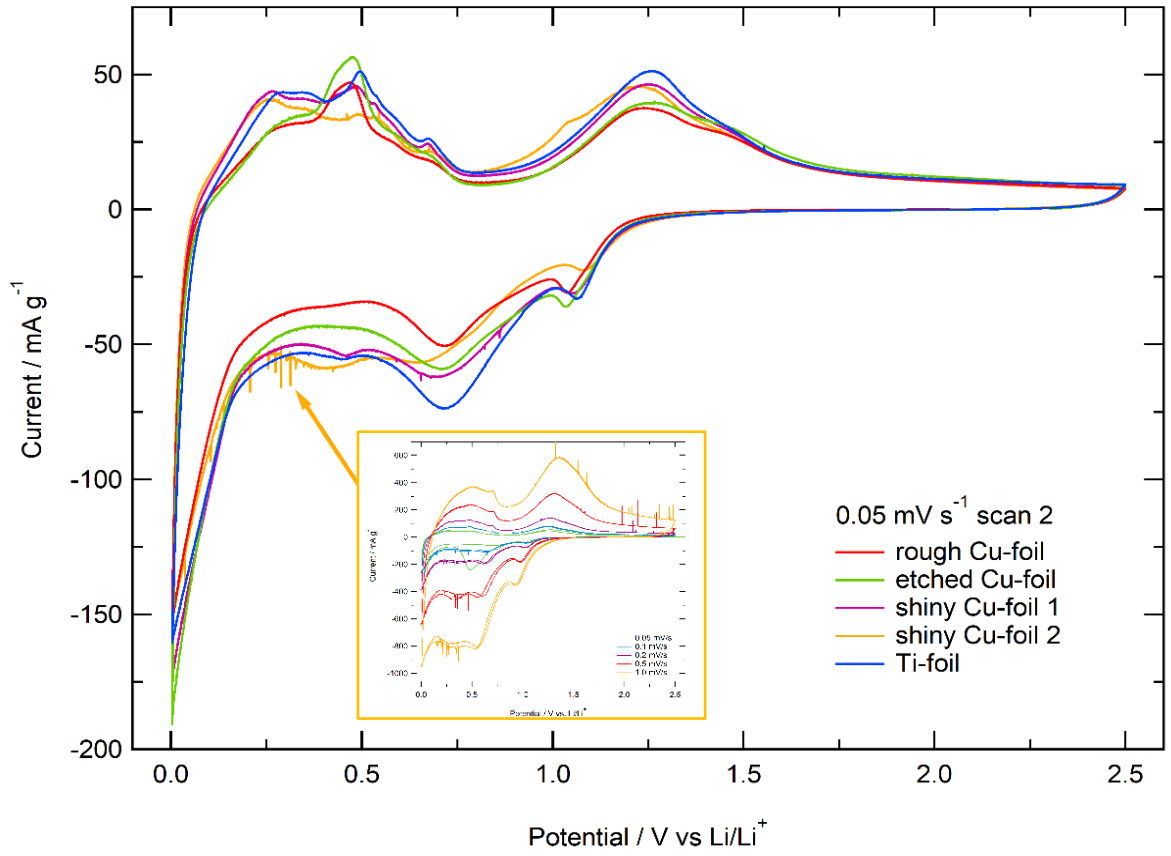

Figure 31. Cyclic voltammograms of Cu_2Zn_8 in 3-electrode lithium half-cell using 1 M $LiPF_6$ in EC:DMC (1:1) as electrolyte recorded at room temperature with a scan rate of 0.05 mV s^{-1}. The second scan was used to exclude most signals coming from SEI formation. The different colours represent different substrates for Cu-Zn alloy deposition. The smaller figure is a set of CVs recorded at different scan rates of Cu_2Zn_8 deposited on a shiny Cu-foil representing the noise.

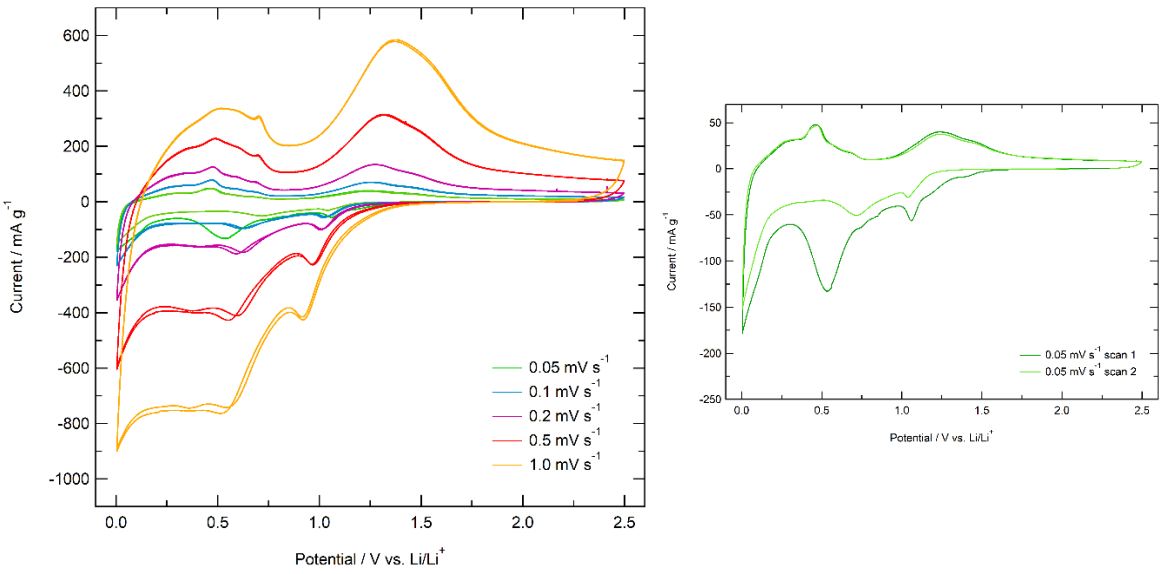

Figure 32. Cyclic voltammograms of Cu_2Zn_8 deposited on a rough Cu-foil as substrate in a 3-electrode lithium half-cell using 1 M $LiPF_6$ in EC:DMC (1:1) as electrolyte recorded at room temperature with varying scan rates from 0.05 – 1 mV s^{-1}.

Cyclic voltammetry experiments carried out at different scan rates lead to an increase of the current response with increasing scan rate. This behaviour can be clearly seen in Figure 32. Two cycles were recorded for each scan rate. The overlapping of the two cycles proves the good reversibility of the lithium insertion/extraction and other related reactions. Only the cathodic scans show a slight shift. The first scan in cathodic direction, drawn in green, indicates a large irreversible peak at approximately 0.5 V which might come from the formation of the solid electrolyte interface, a passivation layer consisting of decomposition products of the electrolyte in presence of lithium. Mueller et al. [79] assigned the origin of the irreversible peak back to the reduction of ZnO to form metallic Zn and Li_2O.

The formation of the lithium alloy proceeds below 0.2 V vs. Li/Li^+. The corresponding delithiation process can be seen in the anodic scan within a potential range from 0.2 – 0.7 V vs. Li/Li^+ which is in accordance with the expectation for lithium alloy anodes (potentials <1 V vs. Li/Li^+). The de-alloying peak is rather broad and consists out of several overlapping peaks which can be explained by a multistep de-alloying mechanism of Li_xZn to Zn.

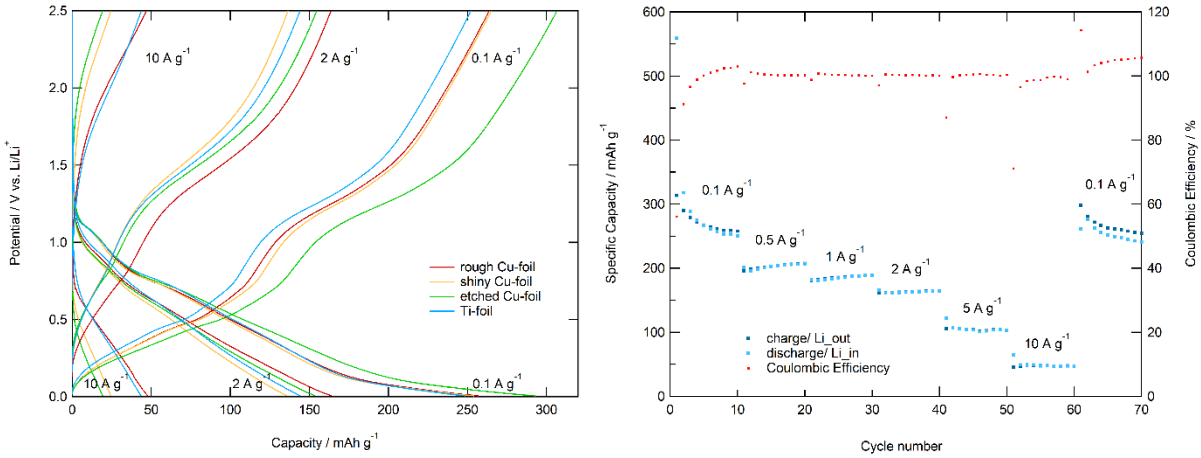

Figure 33. a) Charge/discharge profiles of Cu_2Zn_8 on four different substrates versus lithium at 0.1 A g^{-1}, 2 A g^{-1} and 10 A g^{-1}. b) Representative rate capability test (from 0.1 – 10 A g^{-1}) of Cu_2Zn_8 on rough Cu-foil. The charge and discharge capacity as well as the coulombic efficiency of each cycle is indicated as dot. (GCPL according to Varzi et al. [1])

Also, the cycling performance of all samples was quite similar. Figure 33a shows a part of the charge/ discharge profiles owing to the rate capability test which was performed for all samples in a similar manner to the one of the rough Cu-foil sample shown in Figure 33b. The different cells delivered comparable results and no superiority of one sample compared to the others could be established. The half-cells were cycled with current loads between 0.1 A g^{-1} and 10 A g^{-1} whereby 10 cycles were recorded for each value. All samples could sustain the high current loads although a loss in capacity is noticeable. For instance at 1 A g^{-1}, the alloy still delivers capacities in the order of 180 mAh g^{-1} where commercial graphite [1] only reaches around 15 mAh g^{-1}. After cycling with 10 A g^{-1} the cycling current was decreased again to the value from beginning and the full initial capacity was recovered for each case indicating that the alloy has suffered no severe damage. In the present case, a current rate of 10 A g^{-1} corresponds to charging and discharging within 17 seconds. The reason for the promising rate capability of the sample is probably the porosity and the nanoscale structure of the Cu_2Zn_8 alloy. On account of the increased surface to volume ratio lithium diffusion pathways inside the solid are much shorter because the free lattice sites are closer to the electrode-electrolyte interface.

Another aspect that should not be underestimated is the coulombic efficiency which is, with the expected exception of the first cycle of each current value, around 100%, meaning that the lithium alloy formation is quite reversible. As much lithium is taken out of the alloy during charging as it is inserted during discharging.

3.3. Determination of the Chemical Diffusion Coefficient using Cyclic Voltammetry Method

As visible in Figure 32 there is a dependence of the current response to the scan rate. According to Randles and Sevcik (eqn. 11a) there should be a linear dependence of the peak current to the square root of the scan rate. The corresponding data was plotted for the four major peaks appearing in the CV of the Cu-Zn alloy, but no linear behaviour could be seen with an exception of the data for the delithiation peak at ~0.48 V. Here, in most cases plotting has led to a perfect line with a coefficient of determination R^2 better than 0.999.

Current due to surface capacitive effects should rather be direct proportional to the scan rate. This behaviour was shown for most of the other peaks when plotted but this time directly against the scan rate. These observations led to the assumption that the non-Faradaic current usually coming from a surface pseudo-capacitance and a double-layer capacitance is predominant [61] in the system.

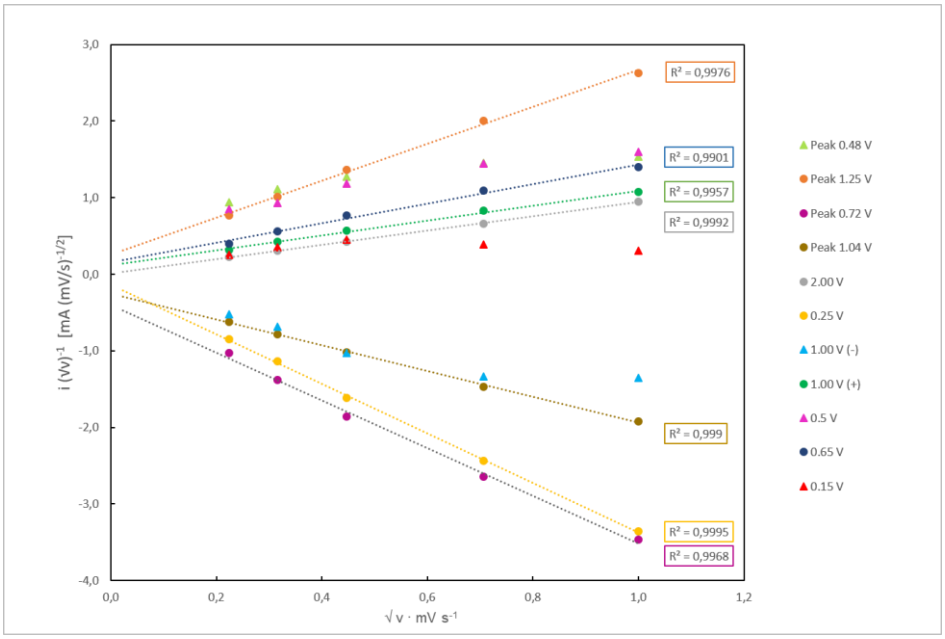

Figure 34. Plots of $i/\sqrt{v}$ vs. $\sqrt{v}$ for certain potentials used for the determination of k_1 and k_2 via eqn.12. A trend line (dotted line) was drawn through the data points for each potential. k_1 and k_2 were further used to determine the contribution of the capacitive current.

We were interested in the amount of capacitive current contributing to the system. The Trasatti-analysis is a useful tool to distinguish between current coming from a diffusion-controlled Li^+ insertion process and the contribution from capacitive effects.

$$\frac{I(V)}{\sqrt{v}} = k_1\sqrt{v} + k_2 \qquad (12)$$

By plotting i/√v vs. √v at different potentials, it is possible to determine the constants k_1 and k_2 from the slope and the y-axis intercept according to equation 12. The corresponding diagram is shown in Figure 34. The straight-line equations were determined from the trend lines (dotted lines in diagram). The linear dependence was observable at most of the potentials and the associated lines show coefficients of determination between 0.990 and 0.100. From the products $k_1 \nu$ and $k_2 \sqrt{\nu}$ the absolute current due to surface capacitive effects and the current triggered by diffusion induced processes at a given potential can be calculated. The relative amount of the capacitive current is given in Table 7 for several potentials.

Table 7. Contribution of surface capacitive effects to the overall current response recorded at different potentials and with varying potential scan rates. The star* indicates that the absolute current values are taken from the maximum of the peaks ignoring a shift in potential. The proportion of capacitive currents increases with increasing scan rate.

Potential	0.05 mV s^{-1}	0.1 mV s^{-1}	0.2 mV s^{-1}	0.5 mV s^{-1}	1.0 mV s^{-1}
1.04 V* (-)	59%	67%	74%	82%	87%
0.72 V* (-)	64%	71%	78%	85%	89%
0.25 V (-)	84%	88%	91%	94%	96%
0.65 V (+)	65%	73%	79%	86%	89%
1.00 V (+)	65%	72%	79%	85%	89%
1.25 V* (+)	68%	75%	81%	87%	90%
2.00 V (+)	96%	97%	98%	99%	99%

Table 7 clearly shows that the proportion of non-Faradaic current is significantly higher than 50% in all cases. Especially at 2.00 V the diffusion-induced current goes down close to zero. This corresponds to the appearance of Figure 32, where no diffusion-induced peak is visible close to 2.00 V. Additionally the charge and discharge curves in Figure 33a show a sloping behaviour between 1.5 and 2.5 V where the reciprocal of the slope should correspond to the capacitance [80]. Also, at 0.25 V the capacitive contribution is relatively high whereas it is lower for the current peaks indicated with a star in Table 7 as well as at 0.65 V and 1.00 V.

One reason for the high contribution of non-Faradaic current might be the high surface area which increases the amount of charge that is able to be stored in the electric double layer. Charge storage kinetics are much faster in electric double layer capacitance electrodes than in purely Faradaic ones [81]. Fast energy uptake and delivery should be possible. Hence, maybe the high contribution of capacitive current is a supplemental factor to the shorter lithium diffusion pathways for the high rate capability of the material.

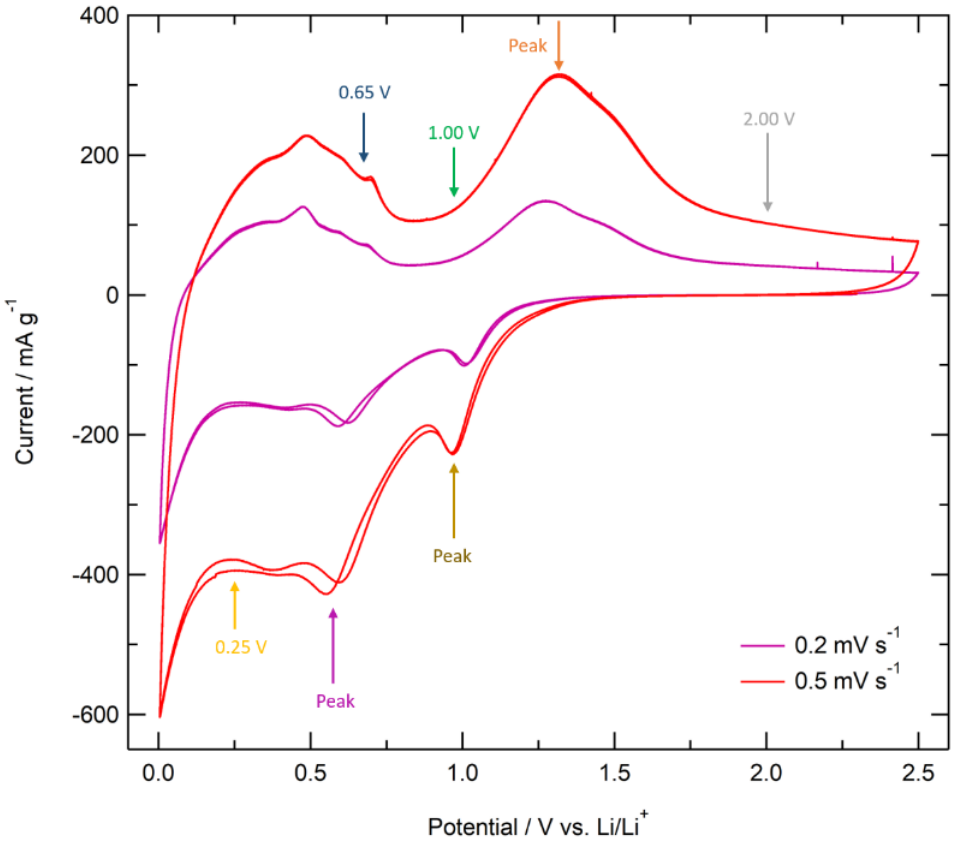

Figure 35. Cyclic voltammograms recorded with scan rates of 0.2 mV s^{-1} (magenta) and 0.5 mV s^{-1} (red) showing two cycles each. The coloured arrows indicate the potentials at which the Trasatti-method was applied. The colours correspond to those of the associated trendlines and data points in Figure 34.

From the diffusion-induced contribution to the current the macroscopic chemical diffusion coefficient was calculated with the Randles-Sevcik equation 11a at the peak potentials indicated in Figure 35 as well as for 0.65 V because no diffusion-induced current could be determined with this method for the de-alloying peak at approx. 0.48 V. The results are shown in Table 8.

Table 8. Macroscopic, chemical diffusion coefficient calculated based on the Randles-Sevcik equation using the peak current /current at 0.65 V after subtracting the capacitive current contribution

Potential	Diffusion coefficient D [$cm^2\ s^{-1}$]
0.65 V	$5.41\ 10^{-19}$
Peak 1.25 V (+)	$1.55\ 10^{-18}$
Peak 0.72 V (-)	$3.64\ 10^{-18}$
Peak 1.04 V (-)	$1.55\ 10^{-18}$

3.4. Investigation on the Ionic Transport Properties and Lithium Self-Diffusion in Lithiated Cu-Zn Alloys

3.4.1. Motional Narrowing Curve/ Line Shape Measurement

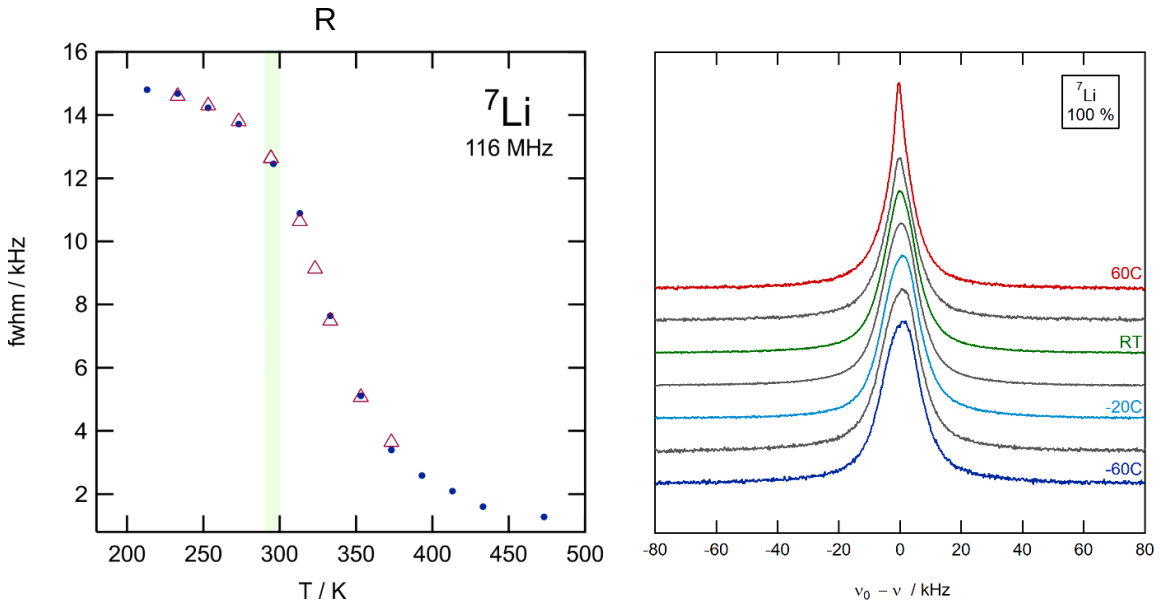

Figure 36. Motional narrowing of the ^{7}Li NMR linewidth of fully lithiated Cu_2Zn_8 (right) and the line width in dependence on the temperature for fully lithiated (Δ) and 66% (•) lithiated Cu_2Zn_8 (left)

^{7}Li NMR spectra were recorded by a single pulse experiment at $\omega_0/2\pi = 116$ MHz over a temperature range from -60 °C (213 K) to 200 °C (473 K) for the fully lithiated sample and between -40 °C (233 K) and 100 °C (373 K) for the sample lithiated to an extend of 66%. The 33% lithiated sample was not investigated further due to a lack of time which will be discussed later. The full width at half maximum of the central transition ($+1/2 \leftrightarrow -1/2$) line of ^{7}Li was determined and plotted against the respective temperature. Figure 36 shows the narrowing of the NMR line induced by

an averaging of the dipole interactions. Due to the single pulse experiment, quadrupole intensities are mostly suppressed and therefore not visible in the spectral lines shown in Figure 36. With the help of echo techniques these effects are expected to show up in the NMR spectra. At low temperatures a flattening of the line width curve is noticeable until a plateau is indicated at 213 K. Here, in the rigid-lattice regime, the lithium diffuses slow and factors like dipolar and quadrupolar interactions or chemical shift anisotropy lead to a broad spectral line which should be more or less constant in this regime. Narrowing of the line sets in at approximately 230 K when the thermally activated motion of the lithium ions leads to an averaging of the internuclear dipole interactions. The rate of line narrowing is the highest at the inflection point of the curve at ~320 K. Here, the lithium jump rate should be roughly in the order of the line width in the rigid lattice regime [74], which is approximately 15 kHz in the present case.

$$\tau_{MN}^{-1} \approx \Delta\omega_{r.l.} \tag{36}$$

The estimated jump rate τ_{MN}^{-1} of lithium in the Cu-Zn alloy would be around $15\ \text{kHz} \cdot 2\pi \approx 10^5\ \text{Hz}$ (at ~320 K). At very high temperatures when the jump rate exceeds the Larmor frequency a plateau is indicated again. Starting at 470 K the spectral line width is again temperature independent and no further increase in lithium ion mobility is detectable. The residual line width is originated from inhomogeneities of the external static magnetic field.

Basically, the motional narrowing curve shows that a diffusion induced relaxation is present in the sample and that the lithium mobility increases significantly between 250 and 400 K meaning that the diffusivity is not at its maximum at room temperature.

3.4.2. Spin-Lattice Relaxation Experiments

Lithium jump rates can be determined more precisely by the analysis of diffusion induced spin-lattice relaxation rates. The Arrhenius plot shown in Figure 37 represents the dependency of the SLR rates measured in the laboratory as well as in the rotating frame of reference on the temperature. The T_1 and $T_{1\rho}$ SLR times were measured at RT for all three samples with varying lithium content. As it can be seen in Figure 37 the sample with the lowest amount of lithium (33%) has by far the longest relaxation time with 3.9 s (T_1) and 0.006 s ($T_{1\rho}$), therefore we focused more on the other two samples due to a lack of time.

The $R_{1\rho}$ measurements were performed at a locking frequency of 25 kHz. The measurement is thus sensitive to lithium jump rates τ^{-1} of the order of 10^5 Hz. For both samples the $R_{1\rho}$ values pass through a maximum appearing at 70 °C for the 66% sample and at 90 °C for the fully lithiated sample. Hence, the partially lithiated sample reaches its maximum mobility already at lower temperatures and might therefore be the "faster sample". Also, the SLR is faster with regard to the partially lithiated sample as it can be seen in Table 9. The lower lithium content in the 66% sample might lead to more unoccupied lattice sites and is probably the reason for the better lithium diffusivity when compared to the fully lithiated sample.

Table 9. Comparison of spin lattice relaxation times in the laboratory frame of reference (T_1) and in the rotating frame of reference ($T_{1\rho}$) for the fully and the partially lithiated Cu_2Zn_8 sample in a temperature range interesting for LIB

Temp. [°C]	T_1 (100%) [s]	T_1 (66%) [s]	$T_{1\rho}$ (100%) [s]	$T_{1\rho}$ (66%) [s]
-40	5.338	4.002	0.0264	not measured
-20	4.166	3.236	0.0122	0.0128
0	3.251	2.524	0.0089	0.0068
RT	2.215	1.836	0.0036	0.0028
40	1.560	1.329	0.0013	0.0005

Knowing the locking frequency, one can calculate the maximum possible lithium jump rate with regard to long-range ion transport.

$$\omega_1 * \tau = 0.5$$

$$\frac{\omega_1}{2\pi} = 25\ kHz$$

Based on the calculation above, a jump rate τ^{-1} of $3.14 \cdot 10^5$ Hz was determined. $\tau^{-1}(T_{1\rho})$ is mostly independent on specific relaxation models and is thus the same for both samples, only the temperature at which this microscopic jump-rate is reached varies.

Comparing the value with literature [82], shows that it is similar to the jump rate of LTO ($1.7 \cdot 10^5$ Hz), a well-studied anode material for LIB. The layer-structured, polycrystalline $Li_{0.7}TiS_2$ [83] is in the order of 10^6 Hz and the microscopic lithium jump rate of one of the fastest known lithium ion conductor so far, Li_3N, is in the range of 10^7 Hz.

The microscopic jump rate can in principle be used to calculate the lithium self-diffusion coefficient D^{uc} using the Einstein-Smoluchowski equation (equ 31). Due to the fact that the lithium jump length as well as the dimensionality are unknown, the calculation is not possible yet. Further investigation on the crystal structure of $Li_xCu_2Zn_8$ is necessary to get an idea whether the lithium occupies interstitial sites, substitutes the host atoms or whether the system undergoes a phase transformation during alloying/de-alloying.

Further analysis of the $R_{1\rho}$ diagram shows that the shape of the peak is rather asymmetrical with a high temperature flank that has approximately half of the slope of the low temperature flank. This leads to the assumption, that lithium diffusion in confined dimensions (1D, 2D) is occurring in the material instead of 3D diffusion which is expected to show rather symmetric peak characteristics, or a flatter low temperature flank caused by correlations. A more precise analysis of the dimensionality is possible with the use of frequency-dependent, temperature-variable NMR [70]. A logarithmic frequency dependence on the high temperature flank points to a 2D diffusion process as it occurs in graphite. In the case of 1D diffusion the $R_{1/1\rho}$ values of the high temperature flank should be proportional to $\sqrt{\frac{A}{\omega_{0/1}}}$ according to Sholl [74,84].

As one can see from eqn. 26, the correlation time can be described by Arrhenius. Therefore, the slope of the flank gives direct access to the activation energies E_A of the jumping processes which are indicated in Figure 37. The activation energies are calculated over the respective area indicated with a solid line.

For the SLR experiment conducted in the laboratory frame of reference no maximum or high temperature flank was accessible because much higher temperatures would have been required for detection. The data was acquired at a resonance frequency of $\omega_0 / 2\pi = 116$ MHz. The method is therefore sensitive to short range ion transport and jump rates in the order of MHz. Having a closer look at the activation energies shows, that the low temperature (LT) flank can be divided into three different areas with varying slopes. This effect is reproducible since both samples follow the same trend.

Since only the LT flank is present, the information is limited and no clear conclusion can be drawn. The differences in slope might come from phase transitions changing the diffusional behaviour of the lithium or, since we are talking about the LT flank, correlation effects like coulombic interactions and/ or structural disorder might lead to the decrease of the activation energies of the respective areas. Another possibility would be non-diffusive background effects [85] which might be the reason for the deviation from the linear behaviour of the LT flank of the $R_{1\rho}$ experiment below RT as well.

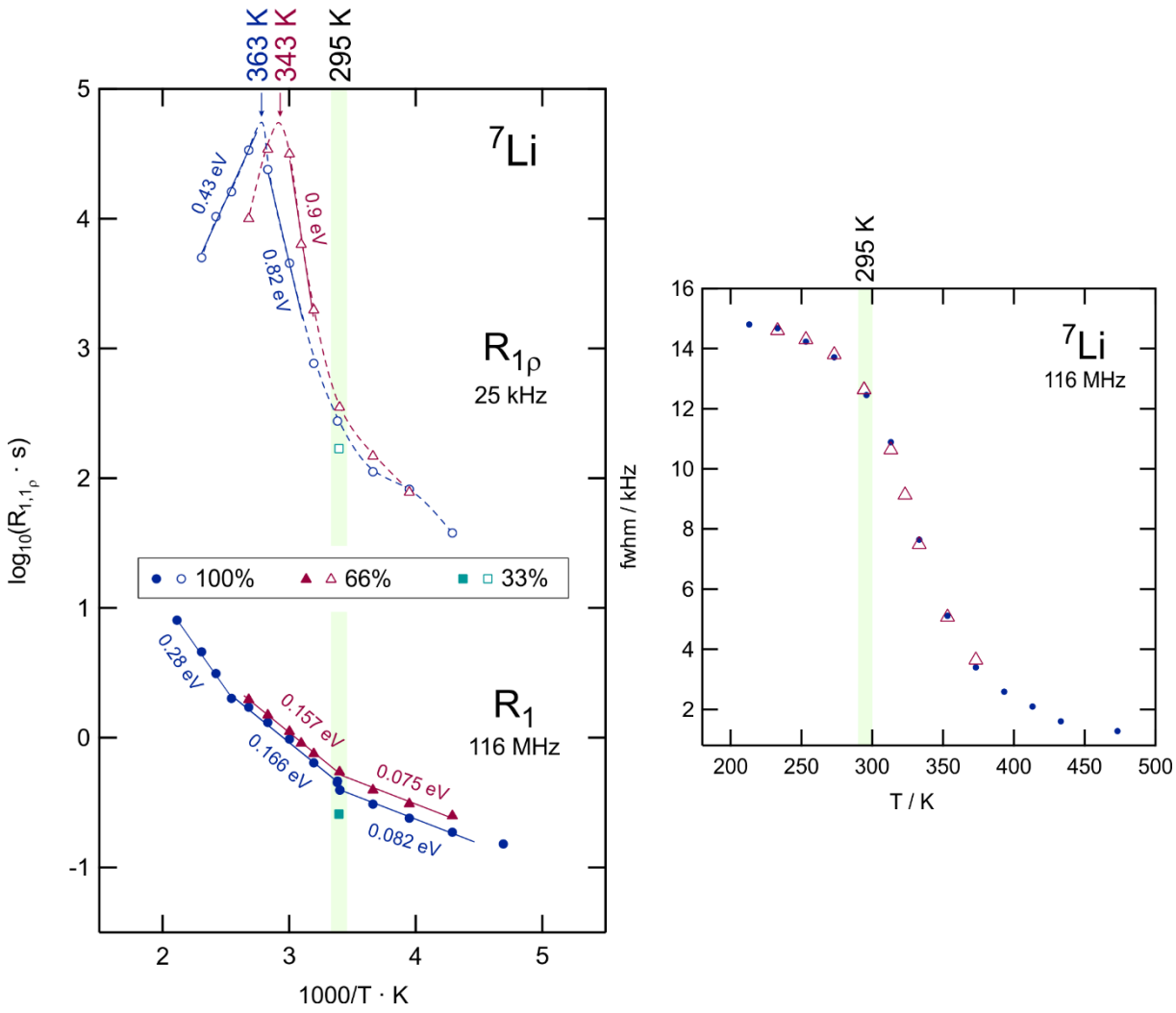

Figure 37. Arrhenius plots of the ^{7}Li NMR spin lattice relaxation rates in the laboratory frame of reference (R_1) at 116 MHz and SLR rates in the rotating frame of reference ($R_{1\rho}$) at 25 kHz. The data was recorded for three samples with different states of lithiation. The dashed lines are a guide to the eye and straight lines according to Arrhenius are adhered to the curve for the calculation of the activation energies. (left) Full width of half maximum of the central ^{7}Li NMR line at 116 MHz at different temperatures. (right)

One motivation of this master thesis was the superior low temperature behaviour of the Cu_2Zn_8 alloy in lithium half cells [1]. Capacities of 200 mAh g^{-1} can be reached at -20 °C and still 140 mAh g^{-1} at -30 °C where commercial graphite electrodes are practically unusable. This phenomenon can be partially described by the NMR experiments. The relaxation times in Table 9 as well as the plots in Figure 37 show that even at low temperatures the lithium is still somehow diffusing although we are already at the limit with -60 °C. This can be seen in the motional narrowing curve, where the rigid-lattice regime appears below this temperature.

In addition, the activation energies of the jumping processes with regard to short range diffusion are relatively small with values < 0.28 eV and get even smaller with decreasing temperature. It might be, that at the lower edge of the measured temperature range, the mobility of the lithium ion is already at its limit (see motional narrowing curve) but the energy barrier which has to be surmounted is low enough that jumping processes can still occur. However, it has to be mentioned that we are only discussing on the basis of the LT flank from R_1 measurements and further experiments are indispensable in order to collect further information on ion dynamics.

Part II – Conductivity of Titania Nanotubes

3.5. Difference Between Annealed and Pristine TiO_2 Nanotubes

Self-assembled titania nanotubes have emerged as a functional material in the past. The highly regular structure is characterized by an easy preparation and the geometry is controllable by the synthesis conditions. Titania nanotubes have also been tested as anode materials [23] in lithium ion batteries due to the higher operation voltage of titania in comparison to graphite electrodes which increases safety on the expense of a lower energy density.

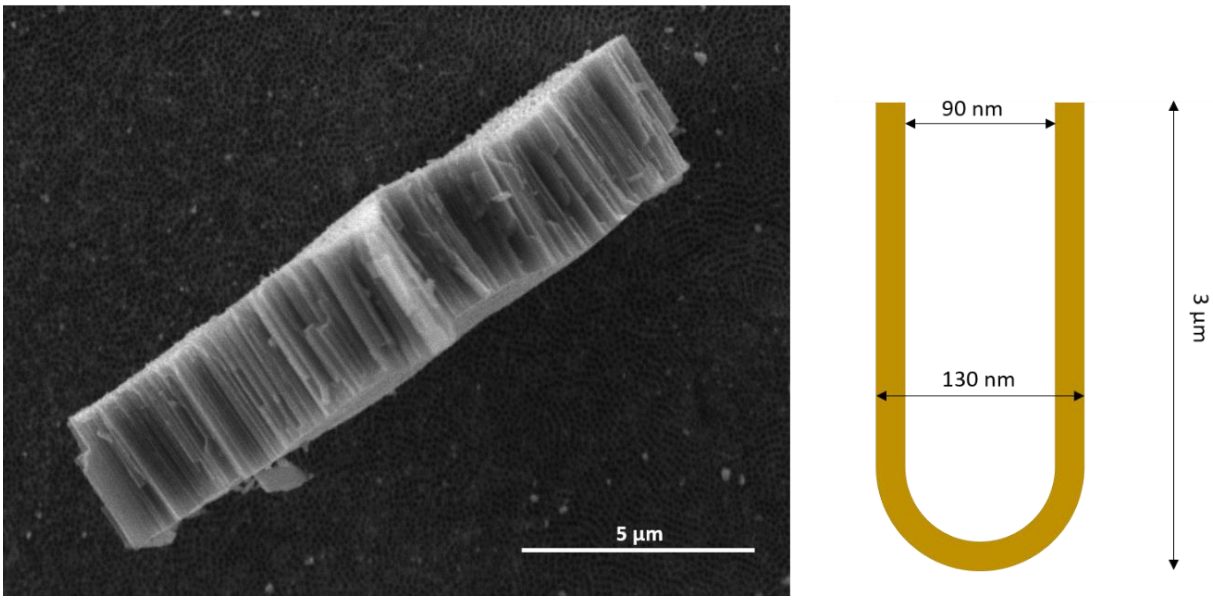

Figure 38. Secondary electron SEM image of a titania nanotube fragment prepared by a two-step anodization in fluoride containing ethylene glycol (anodization voltage: 60 V) as well as the dimensions of the nanotube resulting from the present conditions

Previous experiments have shown that the morphology of titania has an influence on its conductivity whereby the anatase phase is known to show the best electronic conductivity in comparison to the amorphous or rutile phase [86]. The as-anodised nanotubes are amorphous but by certain heat treatments they can be converted to their crystalline homologues [87]. Annealing the amorphous sample at 450 °C for 20h should increase the conductivity (and therefore decrease the resistance) by more than two orders of magnitude [86].

The difference in conductivity between an amorphous/pristine TiO_2 nanotube sample is compared with a sample that was annealed at 400 °C for 20h is shown in the next section (see below). Here we investigated the difference in lithium insertion

between the pristine and annealed samples. Both sample are prepared by anodization in fluoride-containing ethylene glycol using an anodization voltage of 60 V. Titania nanotubes prepared under these conditions have a length of about 3 µm and a wall thickness of approximately 20 nm (see Figure 38).

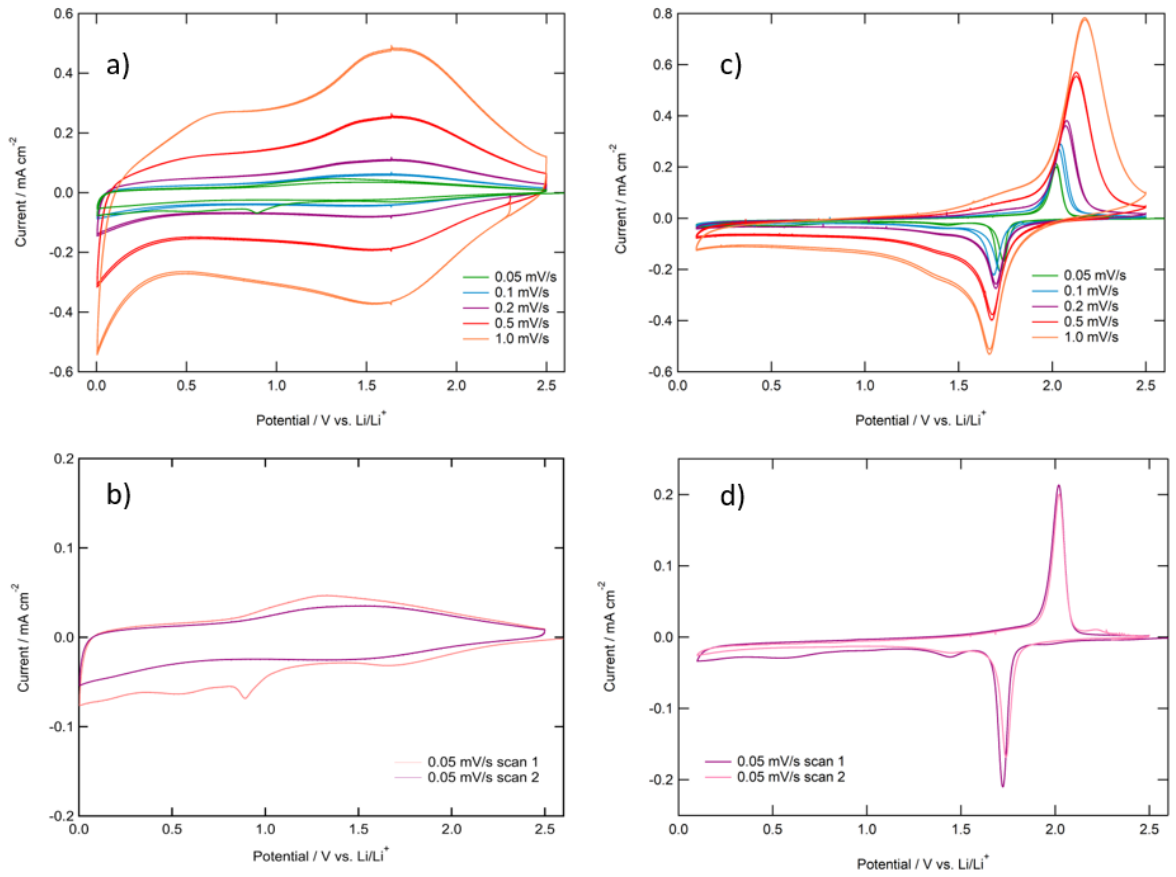

Figure 39. Cyclic voltammograms of pristine (a & b) and annealed (c & d) titania nanotubes in a 3-electrode cell using a LP30 (1M $LiPF_6$ in EC:DMC 1:1) electrolyte and metallic lithium as counter and reference electrode. The CV were recorded at different scan rates. The first two cycles recorded at a scan rate of 0.05 mV s^{-1} are shown separately in b & d. Annealing was done at 400 °C for 20h.

The cyclic voltammograms in Figure 39 clearly show a difference between the two samples. While the pristine one reveals a broad, poorly defined peak distributed over a large voltage range, the annealed sample shows clearly distinct anodic and cathodic peaks which is an indication that the sample has undergone a crystallization reaction during annealing. The cathodic peak corresponding to lithium insertion appears at approximately 1.7 V vs. Li/Li^+ while the anodic peak corresponding to lithium extraction appears at 2.1 V vs. Li/Li^+ when the slowest scan rate is considered. With increasing scan rate a shift to lower or higher potentials is visible.

During lithiation, the tetragonal anatase undergoes a phase transformation to the Li-rich orthorhombic phase [23]. That's why the lithiation/delithiation peaks appear at defined potentials. Amorphous TNT, in contrast, do not undergo any specific phase transition during lithium uptake leading to the broad peak in the CV in Figure 39 a & b.

While lithium accommodation in anatase TNT is limited to the vacant octahedral and tetrahedral holes of the tetragonal structure, in amorphous samples of the many structural and chemical defects provide opportunities for storage of lithium ion and enhanced diffusion inside the material. The effect is also described in theory according to which anatase is only able to take up 0.5 Li per Ti [23] when the available crystallographic sites are considered. This may also be the reason for the enhanced cycling performance of the pristine sample when compared with the annealed one. The rate capability tests in Figure 40 show that much higher charge and discharge capacities can be reached with the amorphous sample. While the annealed one suffers from capacity fading and irregular coulombic efficiencies, the pristine TNT show constant capacities around 200 µAh cm^{-2} at all cycling rates and the coulombic efficiency is rather constant and approaching 100%.

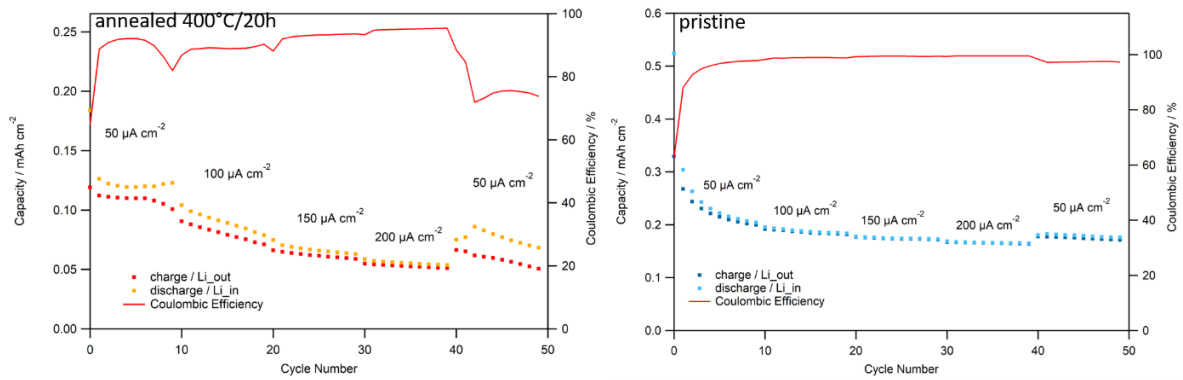

Figure 40. Rate capability test (from 50 µA cm^{-2} to 200 µA cm^{-2}) of nanotubular titania, grown on a titanium substrate. Pristine (right) or annealed at 400 °C for 20h (left). The charge and discharge capacity are depicted as dots and the coulombic efficiency as red line.

To prove which phases are present in the annealed sample an XRD measurement was performed. The received pattern was then compared to prominent titania phases. Since the whole TNT sample including the titanium substrate was investigated, a large titanium metal background signal can be seen in Figure 41. In addition, the reflections of the anatase phase are clearly visible, whereby those of the rutile phase

are not appearing in the pattern. In addition to the information from the cyclic voltammograms this leads to the conclusion, that the amorphous TiO_2 is mostly converted to crystalline anatase.

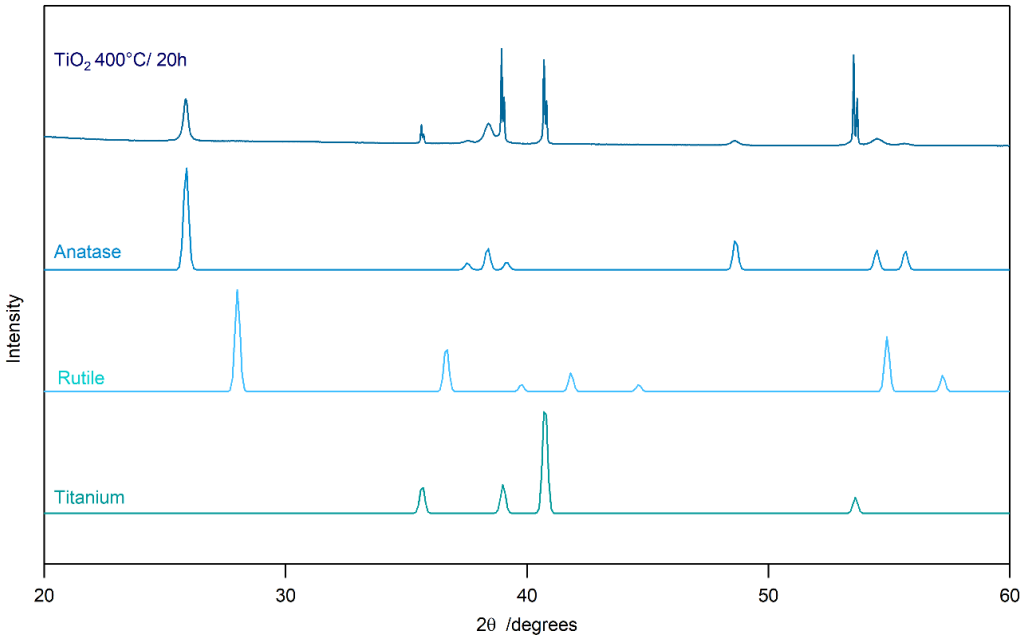

Figure 41. XRD pattern of TiO_2 nanotubes grown on titanium foil. XRD data for comparison is taken out of the Inorganic Crystal Structure Database.

3.6. Preparation of the Contacts

Electrical contacts with a diameter of approximately 0.8 mm were deposited on top of the titania nanotube layers to create a basis for resistivity measurements. Aluminium as well as gold was evaporated through an aluminium mask on top of the tubes with a thickness of ~245 nm and ~100 nm. Nickel contacts, in contrast were defined on the tube surface by sputtering through the mask. For comparison, three pristine as well as three annealed samples were coated with one of the materials each.

SEM images were acquired to get an idea of the surface morphology and coverage of the contacts. As visible in Figure 43 the real diameter of the aluminium contact is about 0.9 mm. Also, the nickel and gold contacts are sized the same. Figure 42 shows SEM images of parts of the different contacts in proximity of a scratch (dark part of the image). All images were acquired with a magnification of 10,000. With the use of SEM the nanotube openings can be clearly seen for the gold and the nickel sample. Thus, the nanotubes are not fully covered by the metals and the coverage is rather limited to the nanotube walls.

With regard to the aluminium sample, areas are visible where the same effect is present, and others can be seen where the nanotubes look covered by the aluminium. This could be an indication, that the aluminium contact works the best for the resistivity measurements, which has been confirmed in practice. Unfortunately, aluminium has the property to form oxide layers and this behaviour is even enhanced under elevated temperature. Due to the fact that oxides are electronic insulators, this effect would render them unusable as contacts for future experiments which include heating.

During scanning electron microscopy, a second phenomenon could be observed regarding aluminium. The squares with different shades visible in the full-size image of the contact and even better on the magnified image (Figure 43) originate from radiation damage caused by the electron beam, although very low acceleration voltages of 5 kV were used for the measurement.

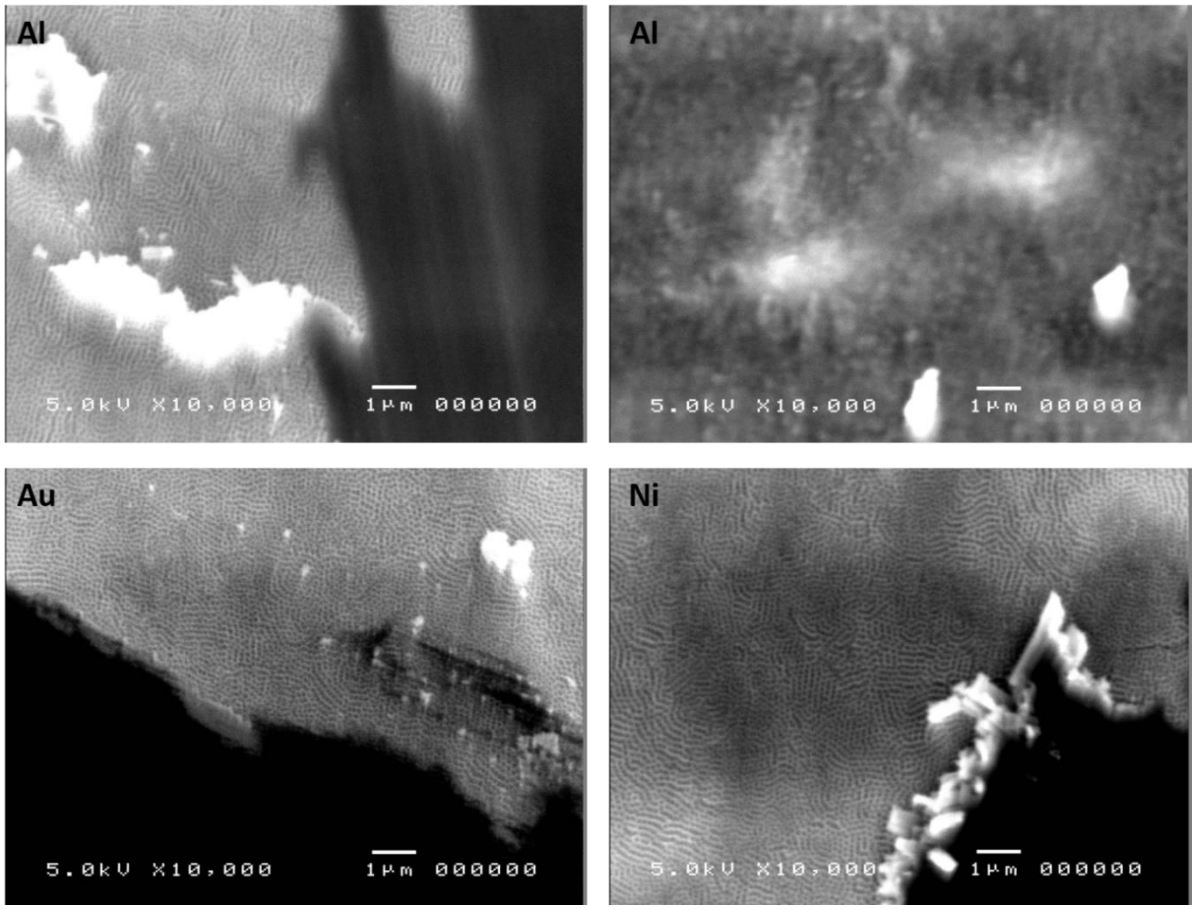

Figure 42. Aluminium (~245 nm) and gold (~100 nm) contacts evaporated through an aluminium mask (Ø 0.8 mm) on pristine titania nanotube samples prepared by anodization on titanium substrates. Nickel contact (300 nm) sputtered through the same mask on titania nanotubes. (SEM images)

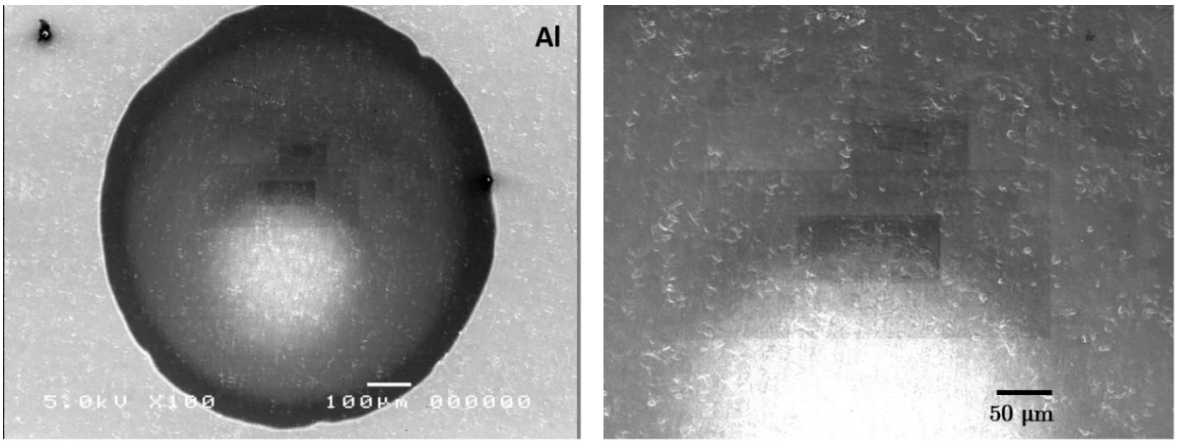

Figure 43. Full-size SEM image of aluminium contact on titania nanotubes (bright background) with damage caused by electron beam (left). Magnification of the beam damage (right)

3.7. Conductivity Measurement

Due to the fact that the previous impedance experiments did not reach the intended goal, new samples were prepared. Aluminium was excluded as contacting material because of the formation of oxides when heated.

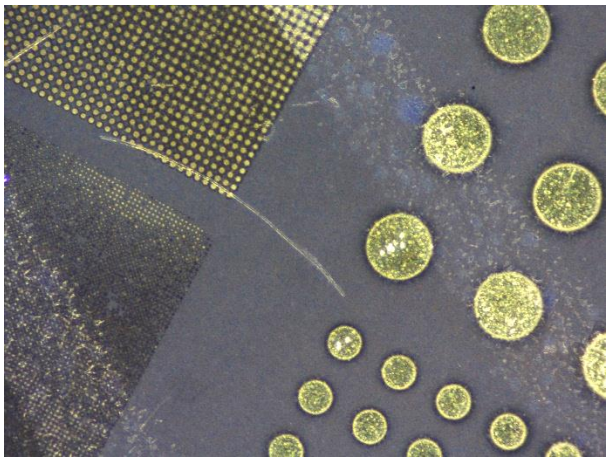

Figure 44. Image of annealed sample including gold sputtered contacts with a thickness of 100 nm and a diameter between 15 and 400 µm

To improve the homogeneity of the contact layer, the titanium substrate was polished prior to the anodization and a thinner (0.1 mm) chromium mask with smaller contact diameters (400, 200, 100, 50, 30 and 15 µm) was used. In consequence to its low contact resistance, gold was the material of choice when it comes to the sputtering of the contacts. The thicknesses were 100 nm for the annealed TNT sample and 400 and 100 nm for the pristine ones. The result is shown in Figure 44.

The measurement was mainly done by a conductivity 2-point set-up whereby the 400 µm or the 200 µm contact (visible in the right half of Figure 44) and the titanium substrate were contacted as shown in Figure 25. Several trials have been made but it was again not possible to record any current signal upon voltage application for the pristine samples. Maybe the overall resistivity is too high to get significant current responses which exceed the noise. However, the IV-curves of the annealed sample have shown a characteristic behaviour.

Since titania dioxide is known to be a semiconductor, contrary to ohmic resistors, the resistance is not constant when applying a cyclic potential sweep and a deviation from linearity can be observed. At very low voltage values, near the origin, very high resistances can be observed which are almost ohmic and tend to decrease when the voltage is elevated (see Figure 47b). According to A. Varpula [88] at low voltages the electrical conductance of a polycrystalline titania is limited by a potential barrier at the grain boundaries. At higher voltages the effective potential barrier decreases and the current increases non-linearly. A second linear region is supposed to appear at very high voltages triggered by the resistance of the bulk regions.

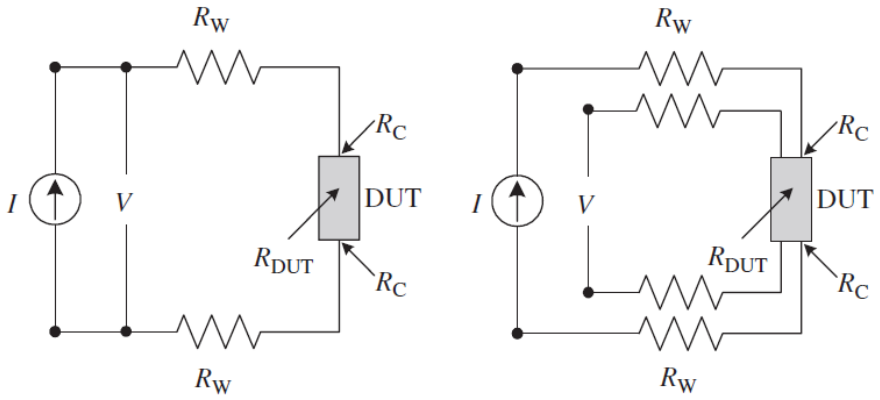

Figure 45. 2-point and 4-point resistivity setup (Source: Semiconductor Material and Device Characterisation [89])

The total resistance which is measured indirectly with the present experiment consists out of the resistance of the contacts R_C (gold and titanium), the resistance of the wires and the tungsten tips R_W and the resistance of the sample R_{TNT}.

$$R_{total} = \frac{U}{I} = R_c + R_w + R_{TNT} \neq constant \tag{37}$$

Usually the contribution of the metallic parts to the total resistance should be negligible in comparison to the semiconductor but nevertheless, the exact ratio is unknown. Using the more complex four-point probe instead of the two-point setup shown in Figure 45 would help to get rid of the voltage drops caused by R_W and R_C [89].

As already mentioned the resistivity of the titania nanotubes is dependent on the applied voltage and cannot be determined directly from the slope of the whole curve. The resistivity at a certain voltage value would correspond to the inverse slope of the tangent of the respective point.

$$dI = \frac{1}{R_{total}}\, dU \tag{38}$$

Since no function of the IV-curve is known and thus no derivation can be formed, the most useful values will be gained by the determination of the slope of the almost ohmic region at very low voltages between -0.2 and 0.2 V. An example is demonstrated in Figure 47. The corresponding values are calculated for different contact arrangements. Since the resistance is also dependent on the geometry the specific resistivity was calculated and a comparison was made.

$$\rho = R \cdot \frac{A}{l}\ [\Omega\, cm] \tag{39}$$

The effective area A as well as the length of the nanotubes l are determined based on the data from Figure 46 assuming a cylinder-shaped body.

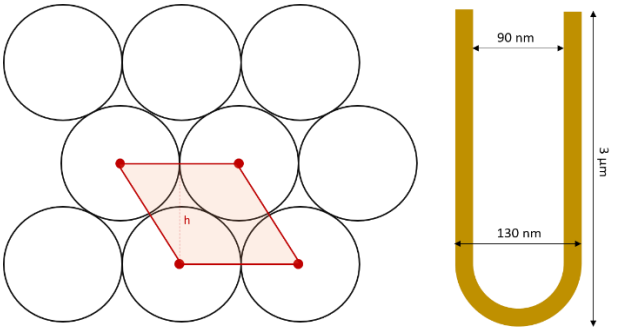

Figure 46. Geometry of the titania nanotubes created by a two-step anodization in fluorine containing ethylene glycol (anodization voltage: 60 V). The area of the rhombus is equivalent to the size of one whole nanotube including the space in between. ($h = \sqrt{3}r^2$)

Table 10. Specific conductivities and resistivities determined from the respective IV-characteristics as well as information on the size of the gold contact and its position. The specific resistivity was calculated based on eqn. 39, an area of 0.472 mm^2 TNT per mm^2 contact and an approximate nanotube length of 3 µm.

contact size	position of contact	conductivity [S cm^{-1}]	specific resistivity [Ω cm]
200 µm	border	$4{,}44\ 10^{-4}$	$2{,}25\ 10^{+3}$
200 µm	border	$1{,}92\ 10^{-5}$	$5{,}21\ 10^{+4}$
200 µm	central	$1{,}38\ 10^{-4}$	$7{,}24\ 10^{+3}$
200 µm	central	$4{,}61\ 10^{-5}$	$2{,}17\ 10^{+4}$
400 µm	central	$6{,}12\ 10^{-5}$	$1{,}63\ 10^{+4}$
400 µm	central	$1{,}28\ 10^{-4}$	$7{,}78\ 10^{+3}$

The specific resistances of the TiO_2 nanotubes from Table 10 are in the order of 10^3-10^4 Ω cm which is slightly lower than the values obtained for annealed samples according to Tighineanu et al. [86] which are in the order of 10^4-10^5 Ω cm. Another interesting fact is, that the recorded IV-curves show a rather symmetric shape and are quite reproducible with regard to the 200 µm contacts (see Figure 47b) whereas this is not the case for the larger contacts (see Figure 48). Four curves consisting out of three cycles were recorded for each contact to check the reproducibility. One example of a 400 µm contact from the middle, with the titanium substrate as counter electrode is shown in Figure 48. Although curves with the typical shape are obtained, the cycles of each measurement do not match and deviations from symmetry are noticeable.

Attempts were also made with contacts smaller than 200 µm, but it has turned out that contacting with the tungsten tips was difficult. In addition, the sputtering of the contacts in the size of 15-50 µm has not lead to the expected results due to undefined outlines and undesired overlapping.

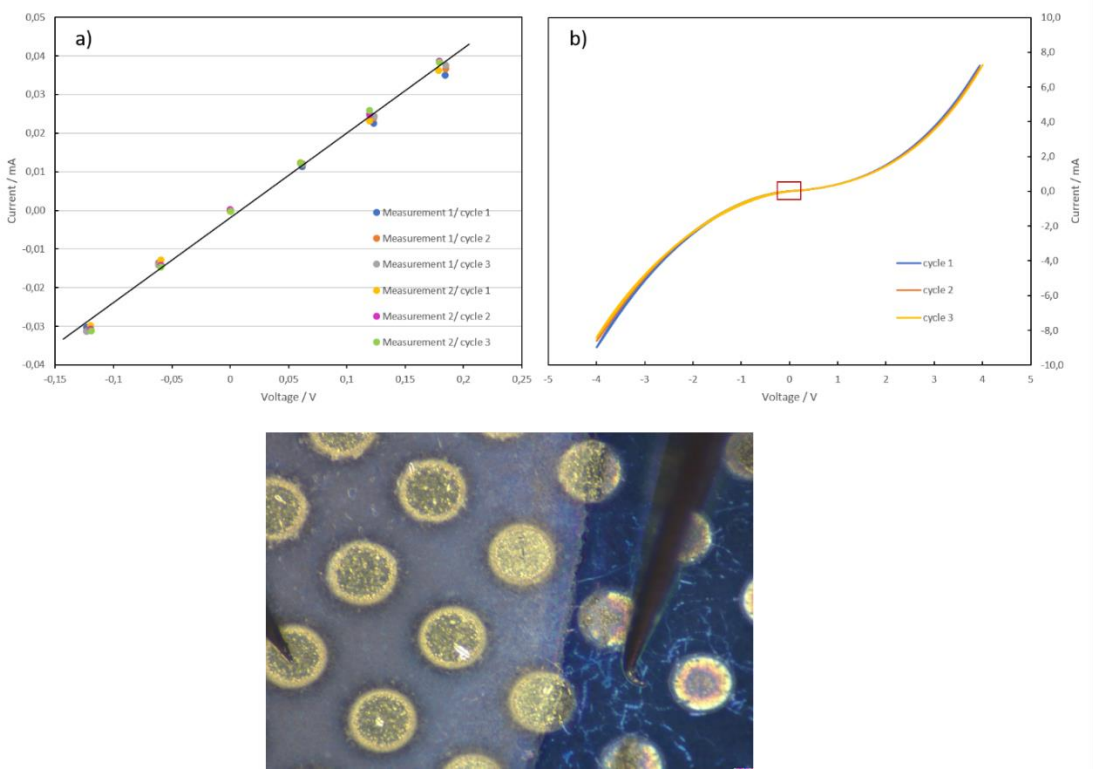

Figure 47. Total IV-characteristics (b) of the TNT sample annealed at 400 °C for 20 h under air. For the conductivity measurements, a 100 nm sputtered gold contact with a diameter of 200 µm was used as one electrode (lo) and the titanium substrate as second electrode (hi). The resistance was determined from the slope of the ohmic region (a) at low voltages indicated with the red square in the IV-curve. The data plotted in (a) was taken from two independent measurements (using the same contact) with three cycles respectively.

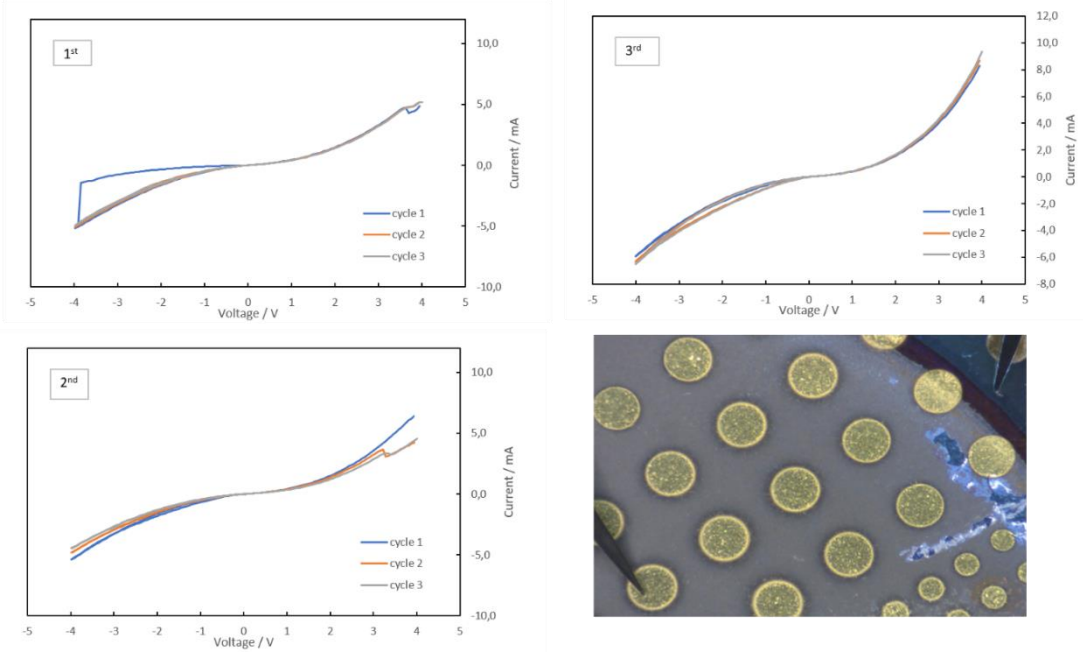

Figure 48. Three individual IV-curves of the annealed (at 400 °C for 20 h under air) TNT sample shown in the image. For each measurement the same gold contact with a diameter of 0.4 mm was used as shown in the image. Different shapes of the curves can be noted although the conditions during acquisition were the same.

Part III – Effect of TiO_2 Nanotubes as Substrate for Cu-Zn Alloys in LIB

3.8. Comparison of Electrochemical Characteristics of Different Electrode Compositions

Since the filling and decoration of titania nanotubes with nanoparticles can change the properties of the tubes [34], it was tried to combine the Cu-Zn alloys with TNT aiming to get an electrode with an enhanced performance. Cu-Zn alloys were deposited on the nanotubes with a so-called pulsed-current approach, described in more detail in chapter 1.4.5.2., whereby 40 short current pulses with a current density of -3 A/cm^2 were applied to the system.

For comparison, GCPL experiments were done for the as-prepared samples ($CuZn/TiO_2/Ti$) as well as for a pure titania nanotube sample and a sample of Cu_2Zn_8 deposited on titanium foil (CuZn/Ti) as used in Part I of the thesis. The experiment was repeated with TNT annealed at 400 °C for 20h to see possible influences of the annealing step. Figure 49 shows the capacities of the three samples with regard to the amorphous titania nanotubes. It is clearly visible that the areal capacity of the titania nanotubes is by far lower than those of the Cu-Zn containing samples. This lower capacity is among other reasons also related to the height of only 3 µm. Longer nanotubes could be prepared by a longer anodization time, but with the length also the resistance increases. TNT preparation is limited to a tube length of approximately 1 mm whereby Cu-Zn alloys can be deposited with much thicker layers. However, one has to mention that the macroscopic pores are getting larger with increasing film thickness and the structure might get instable.

The CuZn/Ti sample shows a high areal capacity during the first cycles. The capacity is then fading until an almost stable value is reached after 30 cycles. The $CuZn/TiO_2/Ti$ sample's capacity in contrast increases slightly during cycling. During the last cycles of the experiment the capacities of both samples look like having stabilized at the same value. No significant increase of the cycling performance when combining the Cu-Zn alloy with TNT could be seen in Figure 49.

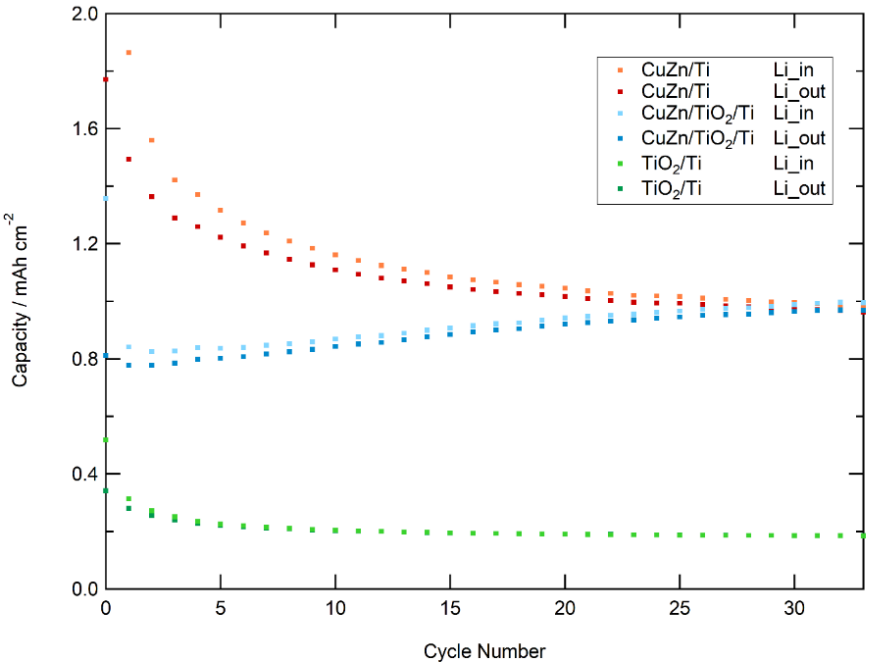

Figure 49. Comparison of the electrochemical performance of amorphous titania nanotubes (TiO_2/Ti) with Cu_2Zn_8 (CuZn/Ti) and CuZn electrodeposited onto the amorphous titania nanotubes using a pulsed current approach (CuZn/TiO_2/Ti). Galvanostatic cycling was performed with C-rates between C/1 – C/2.

When looking at Figure 50 the situation is different. The annealed titania sample has again much lower areal capacities. After some cycles needed to stabilize the capacity, it is visible that the CuZn/$TiO_2$400 °C/Ti sample shows an improvement in capacity over 0.4 mAh cm^{-2} after 30 cycles in comparison to the Cu-Zn sample without any TNT. Overall, the sample shows stable capacity values already after five cycles while the CuZn/Ti sample suffers from continuous capacity fading. The coulombic efficiency is slightly below 100%.

One reason for the capacity improvement might be the fact, that the deposited Cu-Zn alloy sticks better on the rough nanotube surface than on the smoother titanium foil. During cycling of the CuZn/Ti sample, particles might detach from the substrate and do not contribute to the overall capacity in the next cycle which might be an explanation for the capacity fading seen in Figure 49 & Figure 50. The fact that the Cu-Zn alloy is attached very loose to the titanium substrate was also visible during drying with compressed air after deposition.

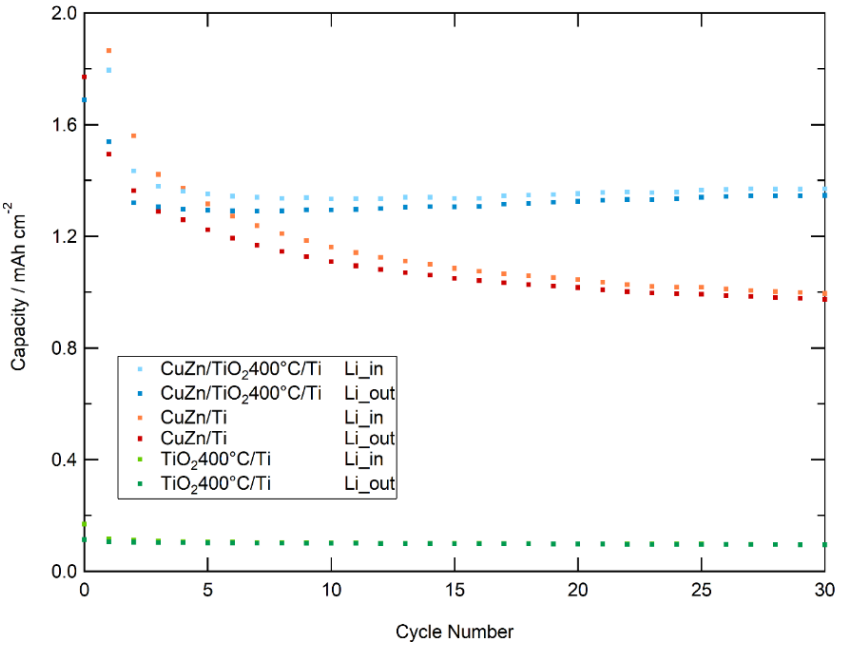

Figure 50. Comparison of the electrochemical performance of annealed titania nanotubes (TiO_2/Ti) with Cu_2Zn_8 (CuZn/Ti) and CuZn electrodeposited onto annealed titania nanotubes using a pulsed current approach (CuZn/TiO_2/Ti). Galvanostatic cycling was performed with C-rates between C/1 – C/2.

3.9. Influence of the Annealing Step

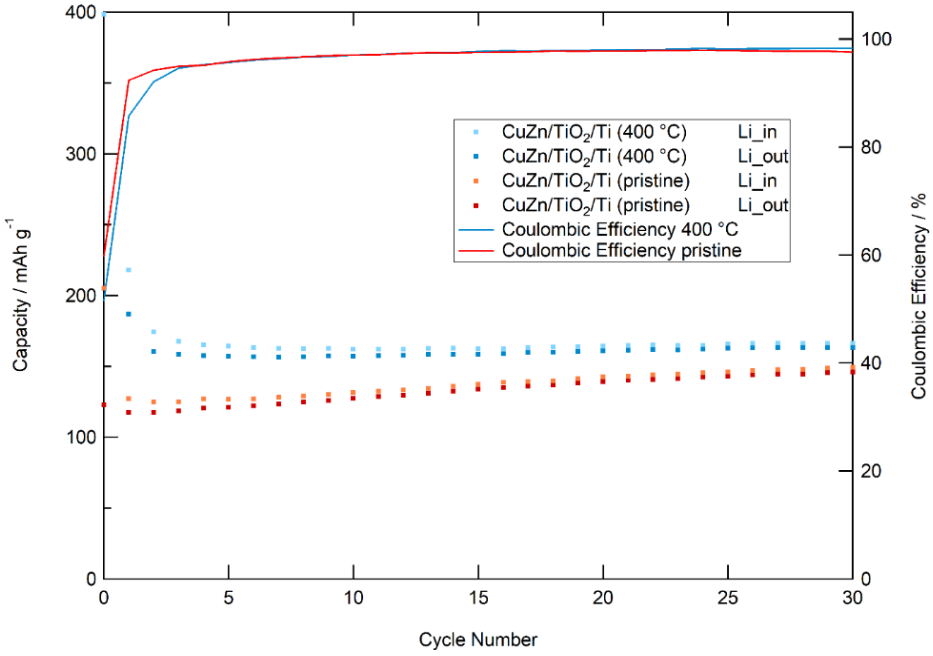

Figure 51. Comparison of the electrochemical performance of a Cu-Zn titania nanotube composite with pristine, amorphous titania nanotubes in one case and with nanotubes annealed at 400 °C for 20 h in the other. (C-rates: C/1.5 for annealed sample and C/2.25 for the pristine sample)

As could be seen in the previous chapter, the composite material containing the annealed TNT has shown some improvement in capacity and cycling stability whereas the composite sample with the pristine TNT did not. Therefore, the GCPL data of the two composites was compared directly in Figure 51. It is obvious, that the coulombic efficiency is constant and rather high, independent on the type of TNT used, with an exception of the first cycles. Here, the deviation is caused by the formation of the solid electrolyte interface, where more charge is consumed than is necessary for storing lithium.

Both composite materials do not suffer from capacity fading over the 30 cycles. At this stage it is difficult to evaluate the long-term stability upon cycling. The composite material containing the annealed TNT exceeds the other sample by a specific capacity of 25 mAh g^{-1}. This difference might very likely be related to the enhanced electronic conductivity of anatase TiO_2.

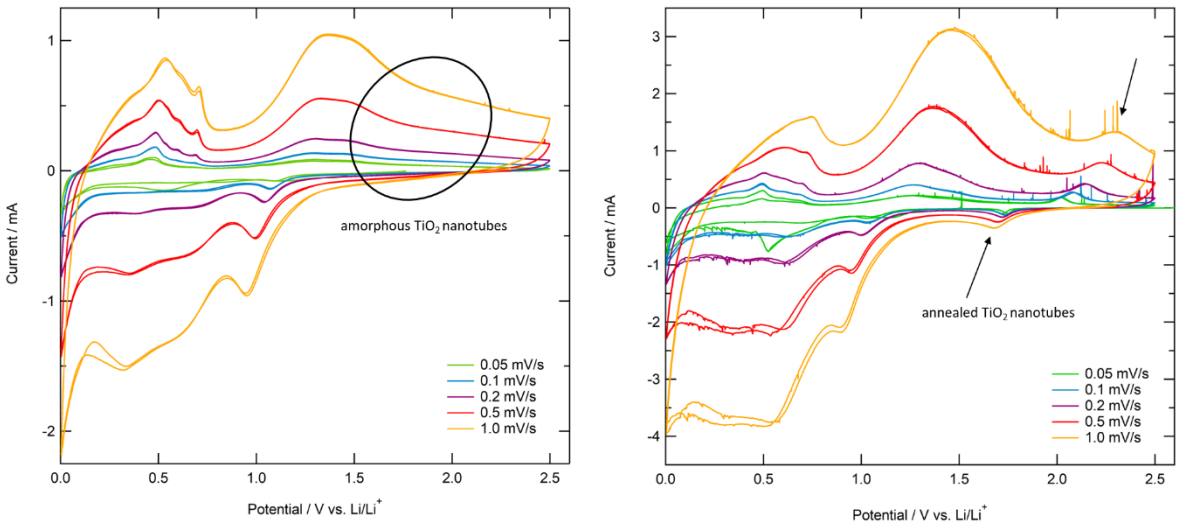

Figure 52. Cyclic voltammogram of a Cu-Zn alloy titania nanotube composite with amorphous TNT (left) and annealed TNT (right). The current responses coming from the reaction of lithium with titania $TiO_2 + x\ Li^+ + x\ e^- \rightleftarrows Li_xTiO_2$ are marked in black.

When looking at Figure 52 it is clearly visible that there is a contribution of both, the nanotubes as well as the Cu-Zn alloy, to the overall capacity with regard to the annealed titania nanotubes. For the pristine TNT a contribution is expected as well, though a clear statement is difficult to be made. Due to the absence of distinct peaks, distinguishing between capacitive current and the small current coming from the amorphous nanotubes is subjected to high errors and unfeasible from the recorded data.

4. Conclusion and Outlook

Nanocrystalline, zinc-rich Cu-Zn alloys were successfully prepared by electrodeposition in an aqueous environment using high cathodic current densities exceeding the diffusion-limited values by far. This leads to highly branched, dendritic deposits with a relatively high specific surface area (approx. 240 m^2/g, BET). With respect to the substrates, the rough Cu-foil has proven to be the best variant. Based on the XRD-measurements, the Cu-Zn alloys with an approximate composition of 20% copper and 80% zinc possess a hexagonal closed packed structure of the Hume-Rothery type. The major part of the alloy consists of the Hume-Rothery ε-phase whereby also small domains of the γ-phase, which is richer in copper, have to be present according to the XRD-data.

The microporous and nanostructured Cu-Zn alloys are known for their outstanding low-temperature behaviour when used as anode material in lithium half cells which is described in more detail by Varzi et al. [1]. The reason for these remarkable results can be understood with the help of solid-state NMR-experiments used for the investigation of the lithium ion dynamics. Recorded motional narrowing curves have shown that the mobility of the lithium ions increases significantly between 250 and 400 K. Although the diffusion maximum is far away from room temperature, the diffusivity already starts to increase at sub-zero temperatures (-20 °C). Below 250 K, no diffusion-induced lithium motion in the kHz range is measurable. This area is known as the rigid lattice regime and is characterized by an almost constant line width. Above 450 K we are in the limit of extreme narrowing.

From the maximum of the $R_{1\rho}$ Arrhenius-plot the maximum possible, microscopic jump rate regarding long-range ion transport was determined. The value of $3.14 \cdot 10^5$ jumps/s is in the range of the well-studied lithium titanium oxide (LTO) anode. Since the microscopic jump-rate and the lithium self-diffusion coefficient are related through the Einstein-Smoluchowski equation, also the diffusion coefficient should be predictable. Unfortunately, up to now no information on the exact crystal structure of the lithiated Cu-Zn alloy is known and consequently also the type of lattice sites occupied by the inserted lithium is unknown. Apart from that, the dimensionality of the lithium dynamics cannot be accurately established from the available data. However, based on the shape of the $R_{1\rho}$ Arrhenius-plot it seems the motion is rather related to diffusion in confined dimensions instead of 3D diffusion which is known to have a characteristic symmetric peak. Anyway, in order to prove whether 1D or 2D diffusion is occurring in the system, frequency dependent NMR experiments have to be made.

Although no maximum could be extracted from the R_1 experiments, it is obvious that the low activation energies of 0.075-0.28 eV are responsible for the relatively fast lithium diffusion and the resulting enhanced rate capability of the Cu-Zn electrodes at low temperatures. Even though the thermal energy of the jumping ion is rather low at low temperatures, the energy barrier to be overwound is also low which increases the probability of successful jumps.

Another feature requiring further investigation is the low temperature flank of the R_1 experiment which consists of three regimes with different slopes resulting in an unusual temperature dependence of the activation energy. This behaviour might come from thermal induced phase transformations or correlation effects influencing the shape of the LT flank. Since only the LT flank is available for analysis, the informative value is limited. Further information could be gained by increasing the high temperature limit to temperatures higher than 200 °C in order to hopefully obtain a HT flank where motion of ions might be independent of correlation effects.

Comparing the three electrochemically lithiated samples with differing lithium content one can say that the relaxation is fastest for the 66% lithiated sample, which might be the result of more free lattice sites in comparison to the fully lithiated sample. The 66% sample also reaches the frequency-dependent, maximum jump rate regarding long-range ion transport, but already at a lower temperature than the fully lithiated sample. The sample with the lowest proportion of lithium (33%) was curiously found to have the slowest relaxation times. This could be due to a different Li-Cu-Zn phase occurring at this low lithium content. However, it is difficult to acquire a complete picture at this stage, this aspect would also require further investigations.

The cycling performance of the Cu-Zn alloy in a lithium half-cell is good with respect to rate capability and cycling stability. Specific capacities of 200 mAh g^{-1} can be reached with a current load of 0.5 A g^{-1} and even 50 mAh g^{-1} when using a current load of 10 A g^{-1}. Distinguishing between capacitive and diffusion induced current from cyclic voltammetry data has shown that the contribution of capacitive current is large, higher than 50% in all cases. The high BET surface area of 240 m^2 g^{-1} of the nanostructured sample might not only be the reason for the enhanced rate capability but also for the large contribution of capacitive current coming from the electric double layer. From the diffusion induced part of the current at the peak potentials the macroscopic, chemical diffusion coefficient can then be calculated leading to values in the order of 10^{-18} cm^2 s^{-1}. To see whether the value is reliable, the chemical diffusion coefficient could be determined additionally using a Galvanostatic Intermittent Titration Technique (GITT) experiment.

Using TNT as substrate for the Cu-Zn alloy does not reach to an improvement in capacity for the pristine, amorphous titania nanotubes whereas an improvement of approximately 0.4 mAh cm^{-2} after 30 cycles could be obtained regarding the annealed TNT. When directly comparing the composite electrode of pristine TNT and Cu-Zn alloy with the electrode consisting of the annealed TNT and Cu-Zn, an improvement regarding the latter one by 20 mAh g^{-1} can be seen. This effect might be related to the titania surface roughened by the nanotubes and due to the higher conductivity improvement of the anatase-rich, annealed TNT. For future research, it would be interesting to take a cross-section SEM image of the composite electrode to see whether the Cu-Zn alloy was partially deposited into the nanotubes by the pulsed current procedure and if the nanotubular structure is intact.

The resistivity of the annealed TNT sample was also measured by a simple DC approach. After electrochemical characterization and XRD measurements it was clearly visible that some structural change towards the crystallization to anatase took place during annealing. It was not possible to record IV-curves for the pristine sample, but data could be acquired for the annealed one. The IV-characteristics between +4 and -4 V differ from the linear behaviour according to Ohm's law. The resistivity was calculated from the approximately Ohm-like curve at low voltage between 0.2 and -0.2 V leading to values between 10^3 and 10^4 Ω cm.

Figures

Tables

Bibliography

[1] A. Varzi, L. Mattarozzi, S. Cattarin, P. Guerriero, S. Passerini, Adv. Energy Mater. 8 (2018) 1–11.

[2] O. Schmidt, A. Hawkes, A. Gambhir, I. Staffell, Nat. Energy 6 (2017) 17110.

[3] H.C. Hesse, M. Schimpe, D. Kucevic, A. Jossen, Lithium-Ion Battery Storage for the Grid - A Review of Stationary Battery Storage System Design Tailored for Applications in Modern Power Grids, 2017.

[4] N. Nitta, F. Wu, J.T. Lee, G. Yushin, Mater. Today 18 (2015) 252–264.

[5] A. Manthiram, ACS Cent. Sci. 3 (2017) 1063–1069.

[6] N. Omar, M. Daowd, P. van den Bossche, O. Hegazy, J. Smekens, T. Coosemans, J. van Mierlo, Energies 5 (2012) 2952–2988.

[7] A. Yoshino, Development of the Lithium-Ion Battery and Recent Technological Trends, Elsevier, 2014.

[8] K. Zaghib, J. Dubé, A. Dallaire, K. Galoustov, A. Guerfi, M. Ramanathan, A. Benmayza, J. Prakash, A. Mauger, C.M. Julien, Lithium-Ion Batter. Adv. Appl. (2014) 437–460.

[9] F. Mizuno, C. Yada, H. Iba, Solid-State Lithium-Ion Batteries for Electric Vehicles, Elsevier, 2014.

[10] Y. Makimura, T. Ohzuku, J. Power Sources 119–121 (2003) 156–160.

[11] M. Thackeray, C.T. Division, E.T. Program, 25 (1997) 3–4.

[12] Robert Bean, Linkedin (2016).

[13] Y. Nishi, Past, Present and Future of Lithium-Ion Batteries. Can New Technologies Open up New Horizons?, Elsevier, 2014.

[14] W. Xu, J. Wang, F. Ding, X. Chen, E. Nasybulin, Y. Zhang, J.G. Zhang, Energy Environ. Sci. 7 (2014) 513–537.

[15] W.J. Zhang, J. Power Sources 196 (2011) 13–24.

[16] D. Deng, Energy Sci. Eng. 3 (2015) 385–418.

[17] Y. Hwa, J.H. Sung, B. Wang, C.-M. Park, H.-J. Sohn, J. Mater. Chem. 22 (2012) 12767.

[18] S. Iwamura, H. Nishihara, Y. Ono, H. Morito, H. Yamane, H. Nara, T. Osaka, T. Kyotani, Sci. Rep. 5 (2015) 25–27.

[19] D.B. Polat, J. Lu, A. Abouimrane, O. Keles, K. Amine, ACS Appl. Mater. Interfaces 6 (2014) 10877–10885.

[20] N.S. Hudak, 4 – Nanostructured Electrode Materials for Lithium-Ion Batteries, Elsevier, 2014.

[21] T. Djenizian, I. Hanzu, P. Knauth, J. Mater. Chem. 21 (2011) 9925–9937.

[22] S. Goriparti, E. Miele, F. De Angelis, E. Di Fabrizio, R. Proietti Zaccaria, C. Capiglia, J. Power Sources 257 (2014) 421–443.

[23] G.F. Ortiz, I. Hanzu, T. Djenizian, P. Lavela, J.L. Tirado, P. Knauth, Chem. Mater. 21 (2009) 63–67.

[24] L. Kavan, M. Graetzel, J. Rathousky, A. Zukal, J. Electrochem. Soc. 143 (1996) 394–400.

[25] M. Pfanzelt, P. Kubiak, M. Fleischhammer, M. Wohlfahrt-Mehrens, J. Power Sources 196 (2011) 6815–6821.

[26] C. Julien, A. Mauger, A. Vijh, K. Zaghib, Lithium Batteries, 2016.

[27] A.R. Armstrong, G. Armstrong, J. Canales, P.G. Bruce, Angew. Chemie - Int. Ed. 43 (2004) 2286–2288.

[28] G. Armstrong, A.R. Armstrong, J. Canales, P.G. Bruce, Chem. Commun. (2005) 2454–2456.

[29] A.R. Armstrong, G. Armstrong, J. Canales, R. García, P.G. Bruce, Adv. Mater. 17 (2005) 862–865.

[30] W. Xu, Z. Wang, Z. Guo, Y. Liu, N. Zhou, B. Niu, Z. Shi, H. Zhang, J. Power Sources 232 (2013) 193–198.

[31] S.-J. Park, Y.-J. Kim, H. Lee, J. Power Sources 196 (2011) 5133–5137.

[32] J. Wang, Y. Zhou, B. Xiong, Y. Zhao, X. Huang, Z. Shao, Electrochim. Acta 88 (2013) 847–857.

[33] I. Hanzu, T. Djenizian, P. Knauth, J. Phys. Chem. C 115 (2011) 5989–5996.

[34] P. Roy, S. Berger, P. Schmuki, Angew. Chemie - Int. Ed. 50 (2011) 2904–2939.

[35] M. Anpo, Pure Appl. Chem. 72 (2000).

[36] D. Prutsch, M. Wilkening, I. Hanzu, RSC Adv. 6 (2016) 98243–98247.

[37] D. Kim, A. Ghicov, S.P. Albu, P. Schmuki, J. Am. Chem. Soc. 130 (2008) 16454–16455.

[38] D. Yan, C. Yu, Y. Bai, W. Zhang, T. Chen, B. Hu, Z. Sun, L. Pan, Chem. Commun. 51 (2015) 8261–8264.

[39] B. Tian, C. Li, J. Zhang, Chem. Eng. J. 191 (2012) 402–409.

[40] J. Xu, C. Jia, B. Cao, W.F. Zhang, Electrochim. Acta 52 (2007) 8044–8047.

[41] M. Paulose, H.E. Prakasam, O.K. Varghese, L. Peng, K.C. Popat, G.K. Mor, T.A. Desai, C.A. Grimes, J. Phys. Chem. C 111 (2007) 14992–14997.

[42] H.E. Prakasam, K. Shankar, M. Paulose, O.K. Varghese, C.A. Grimes, J. Phys. Chem. C 111 (2007) 7235–7241.

[43] E.D.-C. V. Zwilling A. Boutry-Forveille, D. David, M. Y. Perrin, M. Aucouturier, Surf. Interface Anal 27 (1999) 629–637.

[44] V. Zwilling, M. Aucouturier, E. Darque-Ceretti, Electrochim. Acta 45 (1999) 921–929.

[45] R. Beranek, H. Hildebrand, P. Schmuki, Electrochem. Solid-State Lett. 6 (2003) B12.

[46] S.P. Albu, A. Ghicov, J.M. Macak, P. Schmuki, Phys. Status Solidi - Rapid Res. Lett. 1 (2007).

[47] M. Qorbani, N. Naseri, O. Moradlou, R. Azimirad, A.Z. Moshfegh, Appl. Catal. B Environ. 162 (2015) 210–216.

[48] X. Huang, Z. Liu, J. Nanomater. 2013 (2013).

[49] Y. Hou, X.Y. Li, Q.D. Zhao, X. Quan, G.H. Chen, Adv. Funct. Mater. 20 (2010) 2165–2174.

[50] Y.C. Lim, A.S. Siti, P. Nur Amiera, K. Devagi, Y.P. Lim, in: AIP Conf. Proc., 2017.

[51] Y. Zhang, Y. Yang, P. Xiao, X. Zhang, L. Lu, L. Li, Mater. Lett. 63 (2009) 2429–2431.

[52] Y. Lai, H. Zhuang, K. Xie, D. Gong, Y. Tang, L. Sun, C. Lin, Z. Chen, New J. Chem. 34 (2010) 1335–1340.

[53] Y.Y. Song, Z. Da Gao, P. Schmuki, Electrochem. Commun. 13 (2011) 290–293.

[54] N.K. Shrestha, J.M. Macak, F. Schmidt-Stein, R. Hahn, C.T. Mierke, B. Fabry, P. Schmuki, Angew. Chemie - Int. Ed. 48 (2009) 969–972.

[55] N. Liu, K. Lee, P. Schmuki, Angew. Chemie - Int. Ed. 52 (2013) 12381–12384.

[56] A.R. West, Solid State Chemistry and Its Applications, Second Edition, Second, Wiley-Blackwell, Sheffield, 2014.

[57] P. Atkins, J. De Paula, Atkins Physical Chemistry 8th Edition, 2006.

[58] A. Bard, L. Faulkner, Russ. J. Electrochem. 38 (2002) 1505–1506.

[59] M. Brinek, Sodium Insertion into Spinel-Type Lithium Titanium Oxide : Correlation between Crystallinity and Electrochemical Properties, Graz University of Technology, 2017.

[60] Denis Andrienko, Cyclic Voltammetry, Mainz, 2008.

[61] X. Xia, D. Chao, Y. Zhang, J. Zhan, Y. Zhong, X. Wang, Y. Wang, Z.X. Shen, T. Jiangping, H.J. Fan, Small 12 (2016) 3048–3058.

[62] J.K. Park, Principles and Applications of Lithium Secondary Batteries, 2012.

[63] S. Lunghammer, Hochauflösende NMR-Messungen an Kanalstrukturiertem Li2Ti3O7 Und Dem Orthosilikat Li4SiO4, Graz University of Technology, 2016.

[64] T.D.W. Claridge, Tetrahedron Org. Chem. Ser. 27 (2009) 11–34.

[65] C. Vinod Chandran, P. Heitjans, in: G.A.B.T.-A.R. on N.M.R.S. Webb (Ed.), Academic Press, 2016, pp. 1–102.

[66] N.M. Trease, T.K.-J. Ko ster, C.P. Grey, Interface Mag. 20 (2011) 69–73.

[67] M. Feuerstein, R.F. Lobo, Chem. Mater. 10 (1998) 2197–2204.

[68] A. Kuhn, M. Kunze, P. Sreeraj, H.D. Wiemhöfer, V. Thangadurai, M. Wilkening, P. Heitjans, Solid State Nucl. Magn. Reson. 42 (2012) 2–8.

[69] A. Dunst, V. Epp, I. Hanzu, S.A. Freunberger, M. Wilkening, Energy Environ. Sci. 7 (2014) 2739–2752.

[70] V. Epp, Lithium Diffusivity in Fast Solid-State Ionic Conductors: NMR and Impedance Spectroscopic Studies, Graz University of Technology, 2014.

[71] P. Heitjans, S. Indris, M. Wilkening, Diffus. Fundam. 2 (2005) 45.1-45.20.

[72] H. Mehrer, Diffusion in Solids - Fundamentals, Methods, Materials, Diffusion-Controlled Processes, 2007.

[73] P. Heitjans, J. Kärger, Diffusion in Condensed Matter: Methods, Materials, Models, 2005.

[74] A. Kuhn, P. Sreeraj, R. Pöttgen, H.D. Wiemhöfer, M. Wilkening, P. Heitjans, J. Am. Chem. Soc. 133 (2011) 11018–11021.

[75] M. Wilkening, J. Heine, C. Lyness, A.R. Armstrong, P.G. Bruce, Phys. Rev. B 80 (2009) 64302.

[76] B.J. Plowman, L.A. Jones, S.K. Bhargava, Chem. Commun. 51 (2015) 4331–4346.

[77] V.F. Degtyareva, N.S. Afonikova, Solid State Sci. 37 (2014) 47–54.

[78] O. Gourdon, D. Gout, D.J. Williams, T. Proffen, S. Hobbs, G.J. Miller, Inorg. Chem. 46 (2007) 251–260.

[79] F. Mueller, D. Geiger, U. Kaiser, S. Passerini, D. Bresser, ChemElectroChem 3 (2016) 1311–1319.

[80] V. Augustyn, P. Simon, B. Dunn, Energy Environ. Sci. 7 (2014) 1597–1614.

[81] J.S.M. Lee, M.E. Briggs, C.C. Hu, A.I. Cooper, Nano Energy 46 (2018) 277–289.

[82] M. Wilkening, W. Iwaniak, J. Heine, V. Epp, A. Kleinert, M. Behrens, G. Nuspl, W. Bensch, P. Heitjans, Phys. Chem. Chem. Phys. 9 (2007) 6199–6202.

[83] M. Wilkening, W. Küchler, P. Heitjans, Phys. Rev. Lett. 97 (2006).

[84] C.A. Sholl, J. Phys. C Solid State Phys. 14 (1981) 1479–1490.

[85] J. Langer, V. Epp, P. Heitjans, F.A. Mautner, M. Wilkening, Phys. Rev. B - Condens. Matter Mater. Phys. 88 (2013).

[86] A. Tighineanu, T. Ruff, S. Albu, R. Hahn, P. Schmuki, Chem. Phys. Lett. 494 (2010) 260–263.

[87] R. Beranek, H. Tsuchiya, T. Sugishima, J.M. Macak, L. Taveira, S. Fujimoto, H. Kisch, P. Schmuki, Appl. Phys. Lett. 87 (2005) 243114.

[88] A. Varpula, J. Sinkkonen, S. Novikov, in: Phys. Scr. T, 2010.

[89] D.K. Schroder, in: Semicond. Mater. Device Charact., 2006, p. 15.

[90] Purdue University, *Scanning Electron Microscope,* https://www.purdue.edu/ehps/rem/laboratory/equipment%20safety/Research%20Equipment/sem.html (date of access 09.12.2018)

[91] Hoffmann, D. *Theoretische Grundlagen der Festkörper-NMR-Spektroskopie,* https://duepublico.uni-duisburg-essen.de/servlets/DerivateServlet/Derivate-5053/3.pdf, (date of access 27.11.2018)

[92] University College London, *Solid-state NMR, http:/www.ucl.ac.uk/nmr/NMR˙lecture˙notes/L10˙3˙web.pdf* (date of access: 27.11.2018)